Dynamics of Saltwater Intrusion Processes in Saturated Porous Media Systems

by

Sun Woo Chang

A dissertation submitted to the Graduate Faculty of
Auburn University
in partial fulfillment of the
requirements for the Degree of
Doctor of Philosophy

Auburn, Alabama
December 8, 2012

Keywords: saltwater intrusion, density-dependent flow, climate change

Approved by

T. Prabhakar Clement, Committee Chair, Arthur H. Feagin Professor of Civil Engineering
Ming-Kuo Lee, Committee member, Professor of Geology
Xing Fang, Committee member, Associate Professor of Civil Engineering
Jose G. Vasconcelos, Committee member, Assistant Professor of Civil Engineering

Abstract

The overarching goal of this dissertation is to contribute towards a better understanding of the dynamics of saltwater intrusion and the associated transport processes in coastal groundwater systems. As a part of this effort, we have also investigated the impacts of various climate-change impacted variables such as average sea level and regional recharge fluxes on saltwater intrusion processes. Climate change effects are expected to substantially raise the average sea level. It is widely assumed that sea-level rise would severely impact saltwater intrusion processes in coastal aquifers. In the first phase of this study we hypothesize that a natural mechanism, identified here as the ''lifting process,'' has the potential to mitigate, or in some cases completely reverse, the adverse intrusion effects induced by sea-level rise. A detailed numerical study using the MODFLOW-family computer code SEAWAT was completed to test the validity of this hypothesis in both confined and unconfined systems. Our conceptual simulation results show that if the ambient recharge remains constant, the sea-level rise will have no long-term impact (i.e., it will not affect the steady-state salt wedge) on confined aquifers. Our transient confined-flow simulations show that a self-reversal mechanism, which is driven by the lifting of the regional water table, would naturally drive the intruded saltwater wedge back to the original position. In unconfined systems, the lifting process would have a lesser influence due to changes in the value of effective transmissivity. A detailed sensitivity analysis was also completed to understand the sensitivity of this self-reversal effect to various aquifer parameters.

The outcomes of the first phase of this research indicated that the changes in groundwater fluxes due variations in rainfall patterns is one of the major climate-change-induced hydrological variable that can impact saltwater intrusion in coastal aquifers. In the second phase of this study, we use a combination of laboratory experiments and numerical simulations to study the impacts of changes in various types of groundwater fluxes on saltwater intrusion dynamics. We have completed experiments in a laboratory-scale sand tank model to study the changes in two types of groundwater fluxes— areal-recharge flux and regional flux. The experimental results were modeled using the numerical code SEAWAT. The transient datasets collected in this experimental study are found to be useful benchmark data for testing numerical models that employ flux-type boundary conditions. Also, based on the experimental observations we hypothesized that when the fluxes are perturbed it would require relatively less time for a salt wedge to recede from an aquifer when compared to the time required for the wedge to advance into the aquifer. This rather counter-intuitive hypothesis implies that saltwater intrusion and receding processes are asymmetric and the time scales associated with these processes will be different. We use a combination of laboratory and numerical experiments to test this hypothesis and use the resulting dataset to explain the reason for the difference in salt wedge intrusion and recession time scales.

In coastal aquifers, presence of a salt wedge divides the groundwater flow system into two distinct regions which includes a freshwater region above the wedge and saltwater region below the wedge. Typically, the freshwater transport processes occurring above a wedge are much faster than the saltwater transport processes occurring beneath the wedge. Recently, many modeling and laboratory studies have investigated the movement of salt wedges and the associated transport processes. Most of these transport studies, however, have focused on

understanding the groundwater plume transport above a wedge. As per our knowledge, so far no one has completed controlled laboratory experiments to study the transport processes occurring beneath a saltwater wedge. In this study, we have completed contaminant transport experiments to map the dynamics of saltwater flow patterns beneath a wedge and relate it to the freshwater flow patterns present above the wedge. We used a novel experimental approach that employed variety dyed neutral density tracers to map the mixing and transport processes occurring above and below a salt wedge. The experimental datasets were simulated using the SEAWAT code. The model was then used to investigate contaminant transport scenarios occurring beneath a saltwater wedge in larger field-scale problems.

Acknowledgments

Table of Contents

List of Tables

List of Illustrations

x

Chapter 1

INTRODUCTION

1.1 Fundamentals of Saltwater Intrusion

Groundwater is an important freshwater resource used extensively for water supply. Groundwater also supports industrial activities in many areas that have limited number of surface water resources. Unlike a surface water reservoir, which is a concentrated source that can serve only a narrow region, groundwater is a distributed source which can serve populations distributed over a larger region. If the areas where groundwater is present coincided with areas of demand, groundwater can be made available to the local public without any major investment in water transmission infrastructure. Groundwater is also a relatively stable source since climate fluctuations induce relatively small variations in groundwater levels in most cases; large volumes of water stored in groundwater aquifers may serve as a buffer to supply water during lengthy drought periods [*Bear and Cheng*, 2010] .

Currently, within the US, it has been estimated that groundwater aquifers located along the Atlantic Coast supply drinking water to over 30 million residents living in coastal towns from Maine to Florida [USGS, 2000]. These precious coastal aquifers are constantly being contaminated by saline water through a natural process known as saltwater intrusion. Figure 1.1 illustrates the dynamics of groundwater flow and mixing of freshwater and saltwater in a coastal aquifer. As shown in the figure, the fresh groundwater region is in direct contact with the saline seawater region in coastal aquifers. Under natural conditions, a dynamic equilibrium exists between these two regions. There are numerous human and environmental factors that can adversely impact this equilibrium and that lead to severe saltwater contamination of the

1

freshwater region. Once contaminated, it is difficult and expensive to clean up saltwater contaminated aquifers. In some cases the contamination could even be irreversible [Bear and Cheng, 2006].

Saltwater intrusion into freshwater aquifers primarily occurs due to the difference in the density of seawater (which has a density value of 1.025 g/cm^3) and fresh groundwater (which has a density value of 1.000 g/cm^3). This small density difference can play a significant role in controlling two types of saltwater intrusion processes: lateral intrusion of seawater beneath the regional aquifer and up-coning of seawater near pumping wells. The up-coning of seawater normally occurs near a pumping well when a large amount of groundwater is withdrawn from the aquifer. Anthropogenic pumping activities induce a cone of depression around the well, which can lead to upward migration of seawater directly into pumping wells. Lateral intrusion of seawater, on the other hand, would occur naturally when denser saltwater seeps inland at the bottom of the freshwater aquifer (see Figure 1.1). Lateral intrusion of seawater would result in a distinct curved interface that separate the freshwater and saltwater regions; this interface is known as the regional "saltwater wedge." The shape and extent of the interface is determined by various factors such as the geology of the aquifer, climate patterns, variations in natural groundwater flow and the sea level, etc.
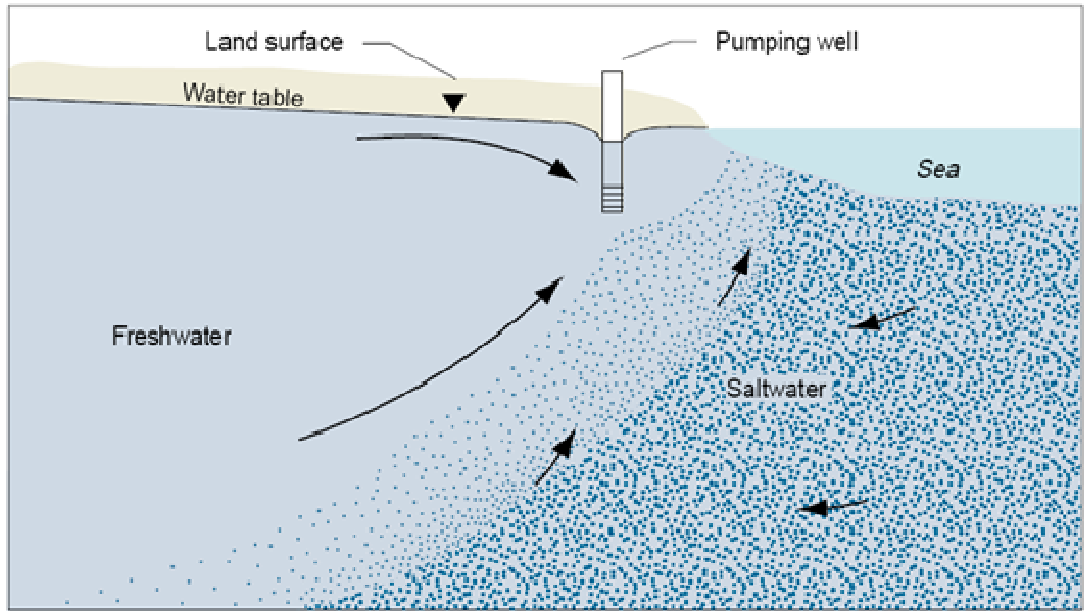
Figure 1.1. Groundwater flow patterns near a pumping well in a coastal aquifer (USGS, 2000)

1.2. Impacts of Climate Change on Saltwater Intrusion Processes

In recent years, population growth and land use changes in coastal areas have increased the demand for freshwater; in addition, it is believed that climate change effects have further reduced the water availability in coastal areas [*Ranjan et al.*, 2006]. Climate change could lead to rise in sea levels, and climate change could also alter groundwater recharge fluxes due to changes in rainfall patterns. Droughts induced by climate change would result in reduction of regional freshwater recharge and this would enhance saltwater intrusion. In the published literature, climate change models have forecasted significant sea-level rise ranging from 0.18 to 0.51 m by the end of this century [*IPCC*, 2007]. According to Titus et al. (2009), during the twentieth century the majority of Atlantic Coast and Gulf of Mexico Coast regions experienced rates of sea-level rise ranging from 2 to 10 mm/year. These estimates are considerably higher than the current global average of 1.7 mm/year, and have led to the concern that rising oceans levels would impact the quality of both surface and ground water supplies and reduce the world's existing fresh water reserves. Impact of climate change on saltwater intrusion in coastal groundwater systems is a serious environmental concern since eighty percent of the world population resides along the coastal regions and depends on coastal aquifers for their water supply. Most of these regions have water-scarce coastal towns that have limited freshwater supply, and are also undergoing rapid population growth. Saltwater intrusion is an important concern for these towns.

Researchers have used modeling studies to understand the coupling of climate change effects with groundwater problems. Dausman and Langevin (2005) evaluated the relative importance of drought, well-field pumping, sea-level rise, and canal management on saltwater intrusion for the Biscayne aquifer in Southern Florida. The simulation results for a coastal

aquifer in Broward County, Florida, demonstrated that if the sea-level rise becomes greater than 48 cm over the next 100 years local well fields would be vulnerable to chloride contamination. Aquifers in small barrier islands are particularly more vulnerable to climate change effects than other aquifers because extreme events such as hurricanes can deposit abnormal amount of salt by directly inundating these islands. Gillett et al. [2000] reported that the occasional hurricanes that strike the Gulf Coast can cause tidal surges up to 5 to 25 feet above the normal level. These storm surges could dump large amount of saltwater over sandy soil and contaminate the shallow groundwater. In addition to storm surges, catastrophic events such as tsunamis can also dump large volume of saltwater above freshwater coastal aquifers. Ilangasekare et al. (2006) discuss a detailed field survey completed in Sri Lanka that documented saltwater intrusion caused by the tsunami wave generated by the 2004 Indian Ocean earthquake on Sunday, 26 December 2004, with an epicenter off the west coast of Sumatra, Indonesia. The tsunami surge not only caused the salt wedge to temporarily move inward, but it also dumped a dense seawater directly over sandy unconfined aquifer along the entire Sri Lankan coast. Ilangasekare et al. (2006) used a combination laboratory analysis together with simple analytical calculations to estimate the time taken to naturally restore these aquifers. These field studies have demonstrated the importance of understanding impacts of climate change and other extreme hydrological events on saltwater intrusion processes.

1.3 Objectives

The overall goal of this research is to develop a better understanding of the dynamics of saltwater intrusion processes in coastal groundwater aquifers. This study has four research objectives, and this dissertation has four distinct chapters that document the results of

investigations related to each of these objectives. Each of the four chapters is organized in a journal format and has an introduction section and also reviews all relevant literature.

The first objective of this study is to investigate the transient impacts of the sea-level rise on saltwater intrusion processes in confined and unconfined coastal aquifers that are driven by natural recharge fluxes. The results of this numerical study are used to develop an intuitive understanding for saltwater intrusion dynamics, which can help better manage the potential long term impacts of sea-level rise on coastal aquifers.

The result of the first phase of this study demonstrated the importance of flux-type boundary conditions. Our review indicated that past experimental efforts related to saltwater intrusion processes have primarily focused on conducting experiments involving constant head boundary conditions. **Therefore, the second objective of this work is to conduct experimental studies to investigate the dynamics of saltwater intrusion processes in an unconfined aquifer using different types of flux boundary conditions**. We investigated the influence of variations in recharge patterns (resulting from changes in rainfall conditions) on a transient movement salt wedge using a laboratory-scale aquifer model and modeled the data using a numerical code. Both the laboratory data and the numerical simulations were used to develop a better understanding of the dynamics of salt wedges under transient flow conditions.

Many of the shallow unconfined aquifers in coastal areas are contaminated by various type of contaminants released from a variety of anthropogenic sources [*Westbrook et al.*, 2005]. Furthermore, regional groundwater flow can also transport large amount of nutrients, which then could be exchanged across the salt wedge. **Therefore, the third objective of this work is to conduct laboratory experimental studies to investigate the contaminant transport processes near a salt wedge**. We completed laboratory experiments to study tracer transport in both

freshwater and salt water flow zones in the vicinity of the salt wedge. The results were used to analyze contaminant transport scenarios above and below a saltwater wedge.

This dissertation has five chapters. The first chapter (the current chapter) provides a basic introduction to this research, lists the objectives, and provides a brief summary of each chapter. The second chapter focuses on the first objective, with the outcome of this effort already published in *Advances in Water Resources* [Chang et al., 2011]. The third chapter focuses on the second objective and the outcome of this effort has been accepted in *Water Resources Research* [*Chang and Clement*, 2012b]. The fourth chapter focuses on the third objective and the outcome of this effort has been communicated to *Journal of Contaminant Hydrology* [*Chang and Clement*, 2012a] The fifth chapter provides a brief summary of the key outcomes of this research and offers recommendations for future work.

Chapter 2

INVESTIGATION OF THE IMPACT OF SEA-LEVEL RISE ON SALTWATER INTRUSION
PROCESSES - A CONCEPTUAL MODELING STUDY

2.1 Introduction

Saltwater intrusion is a serious environmental issue since eighty percent of the world's population live along the coast and utilizes local aquifers for their water supply. In the US alone, it is estimated that freshwater aquifers along the Atlantic coast supply drinking water to 30 million residents living in coastal towns located from Maine to Florida [*USGS*, 2000]. Under natural conditions, these coastal aquifers are recharged by rainfall events, and the recharged water flowing towards the ocean would prevent saltwater from encroaching into the freshwater region. However, over exploitation of coastal aquifers has resulted in reducing groundwater levels (hence reduced natural flow) and this has led to severe saltwater intrusion. Cases of saltwater intrusion, with varying degrees of severity and complexity, have been documented throughout the Atlantic coastal zone. For example, in May County, New Jersey, more than 120 water supply wells have been abandoned because of saltwater contamination [*Lacombe and Carleton*, 1992]. A recent USGS [2000] study provides a summary of saltwater intrusion problems and various mitigation techniques. International organizations have identified saltwater intrusion as one of the major environmental issues faced by several coastal cities in India, China, and Mexico [*WWD*, 1998]. Researchers have also reported that variations in the sea level and the associated wedge movement can influence the near-shore and/or large-scale submarine discharge patterns and impact nutrient loading levels across the aquifer-ocean

interface [*Li and Jiao*, 2003b; *Li et al.*, 2008; *Li et al.*, 1999; *Michael et al.*, 2005; *Robinson et al.*, 2007]. Therefore, understanding the dynamics of saltwater intrusion in coastal aquifers and its interconnection to anthropogenic activities is an important environmental challenge.

While anthropogenic activities such as over pumping and excess paving in urbanized areas are the major causes of saltwater intrusion, it is anticipated that increases in sea level due to climate change would aggravate the problem. Nevertheless, only a few studies have focused on understanding the combined effects of climate change and anthropogenic impacts [*Li and Jiao*, 2003a; b]. Feseker [2007] completed a numerical modeling study to assess the impacts of climate change and changes in land use patterns on the salt distribution in a coastal aquifer. The model used parameters to reflect the conditions similar to those observed at the CAT-field site located in the northern coast of Germany. The study concluded that rising sea level could induce rapid progression of saltwater intrusion. Furthermore, the time scale of changes resulting from the altered boundary conditions could take decades or even centuries to impact groundwater flows and hence the present day salt distribution might not reflect the long term equilibrium conditions. Leatherman [1984] investigated the effects of rising sea-level on salinization in an aquifer in Texas. Meisler et al.[1985] used a finite-difference computer model to analyze the effect of sea-level changes on the development of the transition zone between fresh groundwater and saltwater in the northern Atlantic Coastal Plain (from New Jersey to North Carolina). Navoy [1991] studied aquifer-estuary interactions to assess the vulnerability of groundwater supplies to sea level rise-driven saltwater intrusion in a coastal aquifer in New Jersey. Oude Essink [2001] used a three-dimensional transient density-driven groundwater flow model to simulate saltwater intrusion in a coastal aquifer in the Netherlands for three types of sea-level rise scenarios: no rise, a sea-level rise of 0.5 m per century, and a sea-level fall of 0.5 m per century. They

9

concluded that sea-level rise of 0.5 m per century would increase the salinity in all low-lying regions closer to the sea. Dausman and Langevin [2005] completed SEAWAT simulations for a coastal aquifer in Broward County, Florida, and demonstrated that if the sea-level rise becomes greater than 48 cm over the next 100 years then several local well fields would be vulnerable to chloride contamination. Melloul and Collin [2006] evaluated the potential of sea-level rise to cause permanent freshwater reserve losses in a coastal aquifer in Israel. They quantified the saltwater intrusion effect due the lateral movement of seawater and due changes in the groundwater head. For the assumed sea-level rise of 0.5 m, about 77% of the loss was due to the lateral movement and about 23% was due to the head change. Ranjan et al. [2006] used the sharp interface assumption to analyze the effects of climate change and land use on coastal groundwater resources in Sri Lanka. Giambastiani et al. [2007] conducted a numerical study to investigate saltwater intrusion in an unconfined coastal aquifer of Ravenna, Italy. Their result showed that the mixing zone between fresh and saline groundwater will be shifted by about 800 m farther inland for a 0.475 m per century of sea-level rise. Loaiciga et al. [2011] employed hydrogeological data and the finite-element numerical model FEFLOW to assess the likely impacts of sea-level rise and groundwater extraction on seawater intrusion in the Seaside Area aquifer of Monterrey County, California, USA. Sea-level rise scenarios were consistent with current estimates made for the California coast, and varied between 0.5 and 1.0 m over the 21st century. These authors concluded that sea-level rise would have a minor contribution to seawater intrusion in the study area compared to the contribution expected from groundwater extraction.

The primary focus of most of the field-scale modeling studies discussed above was to understand saltwater intrusion problems related to a specific field site. More recently, Werner and Simmons [2009] completed a conceptual modeling study using a steady-state, sharp-

interface analytical model focused on developing a general understanding of the impacts of sea-level rise on groundwater aquifers that might have different types of boundary conditions. They used a relatively simple analytical model to provide a first-order assessment of the impacts of sea level changes on saltwater intrusion on aquifer systems with two types of boundary conditions. Their results showed that the level of intrusion would depend on the type of inland boundary condition assumed in the model. The steady-state, sharp-interface, analytical expression used in the study did not consider saltwater mixing effects and transient effects. The transient effects in unconfined aquifers were later investigated by Webb and Howard [2010], using a numerical model that employed constant head boundary conditions to study the changes in the rates of intrusion for a range of hydro-geological parameters.

The objective of this study is to complete a comprehensive investigation of the transient impacts of sea-level rise on saltwater intrusion processes in both confined and unconfined coastal aquifer systems that are driven by natural recharge fluxes. The results are then used to develop an intuitive understanding of saltwater intrusion dynamics, which can help better assesses and manage the potential long term impacts of sea-level rise on coastal aquifers.

2.2 Problem Formulation and Conceptual Modeling

Under natural flow conditions, dense sea water would have the tendency to intrude beneath fresh groundwater. The spatial extent of the intruded saltwater wedge (designated as the "toe position XT") would depend on several aquifer parameters including recharge rate, regional aquifer discharge rate, hydraulic properties, and sea level. Recent climate change studies have shown that the global sea-level, on average, is expected to rise between 18 and 59 cm this century [IPCC, 2007]. Worst-case projections show it could be as high as 180 cm [Vermeer and

11

Rahmstorf, 2009]. Therefore, environmental planners worldwide are concerned about the impacts of sea-level rise on saltwater intrusion processes, especially in over-utilized, urbanized coastal aquifers that already have low groundwater levels. Currently, it is expected that the rising sea level will enhance saltwater intrusion and potentially contaminate many freshwater reserves. Figure 2.1a depicts a commonly assumed conceptual model [Cheng et al., 2000; Custodio and Bruggeman, 1987; Fetter, 2001; Mantoglou, 2003; Strack, 1976; Werner and Simmons, 2009] that illustrates how the rising sea level would impact the groundwater quality by forcing the wedge to migrate inland. This conceptual model, however, ignores the fact that when the seawater rises at the sea-side boundary the system would pressurize and the water-table level might be "lifted" throughout the aquifer. Figure 2.1b illustrates a revised conceptual model. This revised model accounts for the lift in the groundwater level over the entire system due to the changes in the sea-side boundary condition. It is expected that after a long period (i.e., at or near steady state) this lifting effect would approximately raise the entire fresh water body (measured from the bottom of the aquifer) by an extent similar to the sea-level rise (i.e., a similar order of magnitude). One could intuitively expect this lifting mechanism to counteract and reduce the impacts due to the sea-level rise. However, it is unclear to what extent this lifting process could reduce the overall impacts due to sea-level rise. In this study, we employ this revised conceptual model to hypothesize that changes in the sea-level might have little or no impact on saltwater intrusion when the net flux through the system is unchanged. The overall goal of this conceptual study is to test the validity of this hypothesis, and understand its ramifications under transient conditions in idealistic confined and unconfined systems.
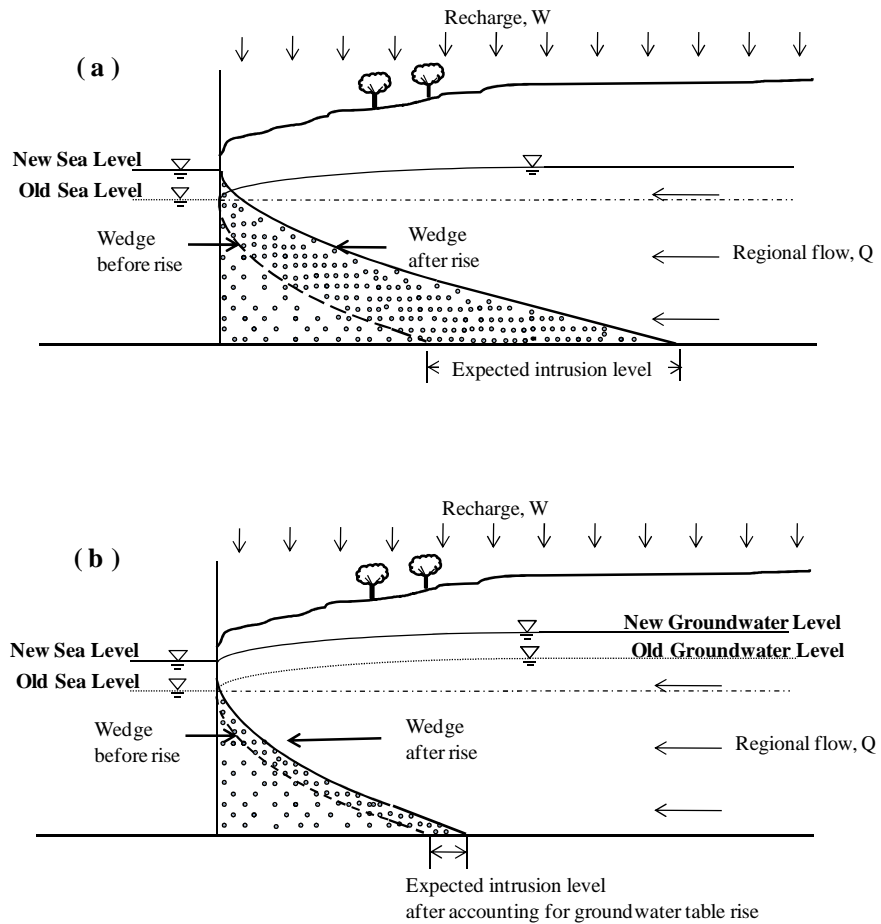
Figure 2.1. Comparison of conceptual models used for visualizing the impacts of sea-level rise on a saltwater wedge: (a) salt wedge profile after sea-level rise based on a traditional conceptual model that ignores the lifting effect, and (b) a new conceptual model that includes the lifting effect.

2.3 Details of Numerical Experiment

The base-case problem considered in this study was adapted from Werner and Simmons' conceptual model [*Werner and Simmons*, 2009] of a seawater intrusion field study completed in Pioneer Valley, Australia. The original problem only considered unconfined flow conditions; in this work, the problem was modified to investigate both confined and unconfined conditions. Our numerical study considered a two-dimensional aquifer system which is 1000 m long and 30 m thick. A rectangular numerical grid, with $\Delta x = 4$ m, $\Delta y = 1$ m and $\Delta z = 0.4$ m, was used. The initial sea level (prior to the rise) was assumed to be at 30 m and the sea level was then allowed to rise instantaneously to 34 m. The net sea-level rise assumed was 4 m, a theoretical worst-case scenario which is approximately double the extreme value predicted by Vermeer and Rahmstorf [2009]. The assumed sea-level rise was chosen to approximately mimic the last interglacial period's rapid sea-level rise that reached up to 4 to 6 m due to rapid loss of ice-sheet [*Blanchon et al.*, 2009]. It is important to note that this is not a "true" scenario simulation exercise; our objective is not to forecast the future location of saltwater wedge for a specific system, rather it is to develop a generic conceptual understanding to assess the potential impacts of sea-level rise on saltwater intrusion processes. Therefore, some extreme sea-level rise scenarios were initially simulated (as the base-case) to better illustrate certain subtle transport mechanisms. Later, as a part of the sensitivity analysis, we explore some realistic sea-level rise scenarios that range from 0.2 m (minimum rise predicted by IPCC) to 4 m (double the maximum rise predicted by Vermeer and Rahmstorf [2009]). Also, in all base-case simulations we assumed instantaneous rise (a worst-case scenario) and later in the sensitivity section we have presented the results for other finite rates of sea-level rise.

The seawater density was assumed to be 1,025 kg/m^3 with salt concentration of 35 kg/m^3. The regional groundwater flux supplied through the inland boundary using a set of artificial injection well nodes. The flux (q, flow per unit depth) supplied from the right boundary was 0.005 m^2/day (or a total flow rate (Q) of 0.15 m^3/day over the 30 m thick aquifer). Recharge (W) flow was delivered from the top boundary at the rate of 5×10^{-5} m/day. These regional and recharge flows were simply selected to locate the initial location of the saltwater toe in between 300 to 500 m. The hydraulic conductivity was set to 10 m/day, specific storage was set to 0.008 m^{-1} in each confined layer, and porosity to 0.35. Longitudinal and transversal dispersivity values were assigned to be 1 m and 0.1 m, respectively. The initial sea level was set at 30 m to simulate a base-case steady-state wedge. This steady-state wedge was later used as the initial condition in all subsequent sea-level rise simulations. Impacts of density-weighting schemes (upstream and central) and various advection schemes (TVD and upstream finite-difference) were investigated in using tests simulations (results summarized in Appendix 2 and 3). In the final simulations we used upstream density weighting and the finite difference scheme advection package. Other model parameters used are summarized in Table 2.1.

The MODFLOW-family variable density flow code SEAWAT [*Langevin C et al.*, 2003] was used in this study with the central difference weighting option. The modeling approach was validated by solving Henry's steady-state solution [*Henry*, 1964; *Simpson and Clement*, 2004] and also laboratory data provided by Goswami and Clement [2007], and Abarca and Clement [*Abarca and Clement*, 2009]. Several sets of numerical experiments were completed to explore various types of flow conditions and parameter values. The first set of experiments only considered confined-flow conditions and the results were used to explore certain novel salt-

wedge reversal mechanisms that have not been reported in the published literature. Later simulations consider both confined and unconfined flow conditions.

Table 2.1. Aquifer properties and hydrological properties used for the base-case problem.

Property	Symbol	Value
Horizontal aquifer length	L	1000 m
Vertical aquifer thickness	B	30 m
Inland groundwater flow rate	Q	0.15 m^3/day
Uniform recharge rate from top	W	5×10^{-5} m/day
Hydraulic conductivity	K	10 m/day
Specific storage,	Ss	0.008 m^{-1}
Longitudinal dispersivity	α_L	1 m
Transverse dispersivity	α_T	0.1 m
Saltwater concentration	Cs	35 kg/m^3
Saltwater density	ρ_s	1,025 kg/m^3
Freshwater density	ρ_f	1,000 kg/m^3
Porosity	n	0.35

2.4 Results

2.4.1. Impacts of Sea-level Rise on Confined Flow Conditions

The goal of the first steady-state simulation is to estimate the initial saltwater wedge profile that would exist in the system prior to sea-level rise. Figure 2.2 (continuous line) shows the 50% isochlor of the initial steady-state concentration profile for the base-case, confined-flow system. This 50% concentration profile is defined as the base saltwater wedge. The figure shows that under the assumed groundwater flow conditions, the toe of the salt wedge advanced to 382 m into the aquifer before sea-level rise. This steady-state condition was used as the initial condition in all subsequent simulations.

The second steady-state simulation aimed to predict the long-term salt-wedge profile after the sea-level rise. The water level at the seaside boundary was abruptly increased from 30 to 34 m to simulate an instantaneous sea-level rise. The system was allowed to evolve for 80,000 days to reach steady-state conditions. The new steady-state solution for the salt wedge simulated by the model after raising the sea level is also shown in Figure 2.2 (using circle data points). Interestingly, and rather surprisingly, the model-predicted saltwater profiles for both conditions (pre and post sea-level rise) were identical, indicating that the sea-level rise will have no impact on the location of the steady-state wedge when the freshwater flux transmitted through the system remained constant (i.e., if the rainfall/recharge pattern was not changed). This non-intuitive result has several important practical implications. The result indicates that the lifting effect postulated in the conceptual model described in Figure 1c will fully offset the negative impacts of sea-level rise in constant flux confined flow systems.

To further explore this result, we present the transient evolution of the location of the saltwater wedge in Figure 2.3. These profiles show that when the sea-level was instantaneously raised, the wedge initially started to move inward; however, after about 8,000 days, the direction of wedge movement reversed and the wedge started to move backward until it reached the initial steady-state profile. As far as we are aware, no one has predicted or postulated this self-reversal mechanism. Understanding this self-reversal process has an enormous implication on how water resources managers would perceive and manage the impacts of sea-level rise on saltwater intrusion. 10% isochlor and 90% isochlor shows the same transient movement (See appendix 1)

Figure 2.4 shows the transient variations in the toe position of the saltwater wedge (X_T). The data shows that, under assumed flow conditions, the salt wedge first advanced into the aquifer for about 8,000 days and reached a maximum distance of 432 m (from the sea boundary) and then started to recede. The figure also shows the simulated transient freshwater head levels at the right side boundary. This freshwater head data is an excellent surrogate for quantifying the progression of the aquifer "lifting" process, postulated in Figure 2.1b. This dataset shows that the initial head at the right boundary, as predicted by the model prior to the sea-level rise, was 31 m. When the sea-level was raised instantaneously from 30 to 34 m, it took about 2,000 days for the right boundary to fully respond to this change. After about 2,000 days, the fresh-water level in the right boundary reached a constant value of about 35 m. The net change in the freshwater level was about 4 m, almost identical to the sea-level rise forced at the left boundary. This implies that the raising seaward-boundary head lifted the entire fresh groundwater system by a similar order of magnitude. This lifting process was able to fully reverse the salt wedge location. The rate of the reversal process would depend on the rate at which the groundwater system was lifted (or how quickly the groundwater heads would respond), which would in turn depend on the

18

storage properties of the aquifer and the rate of sea-level rise. In the following section, we provide a detailed analysis that quantifies the sensitivity of the self-reversal process to the value of storage coefficient, the rate of sea-level rise and the magnitude of rise. All these simulations used the base-case steady-state solution as the initial condition.
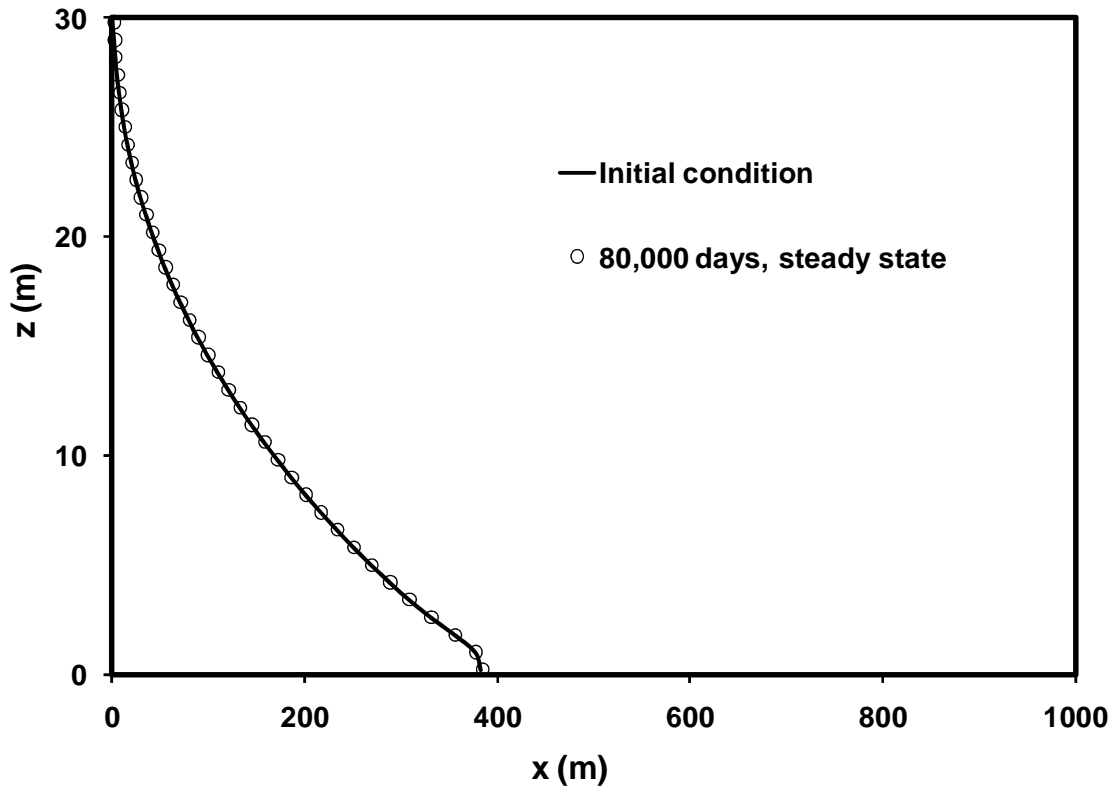
Figure 2.2. Comparison of steady-state salt wedges predicted before and after the sea-level rise in the confined system.
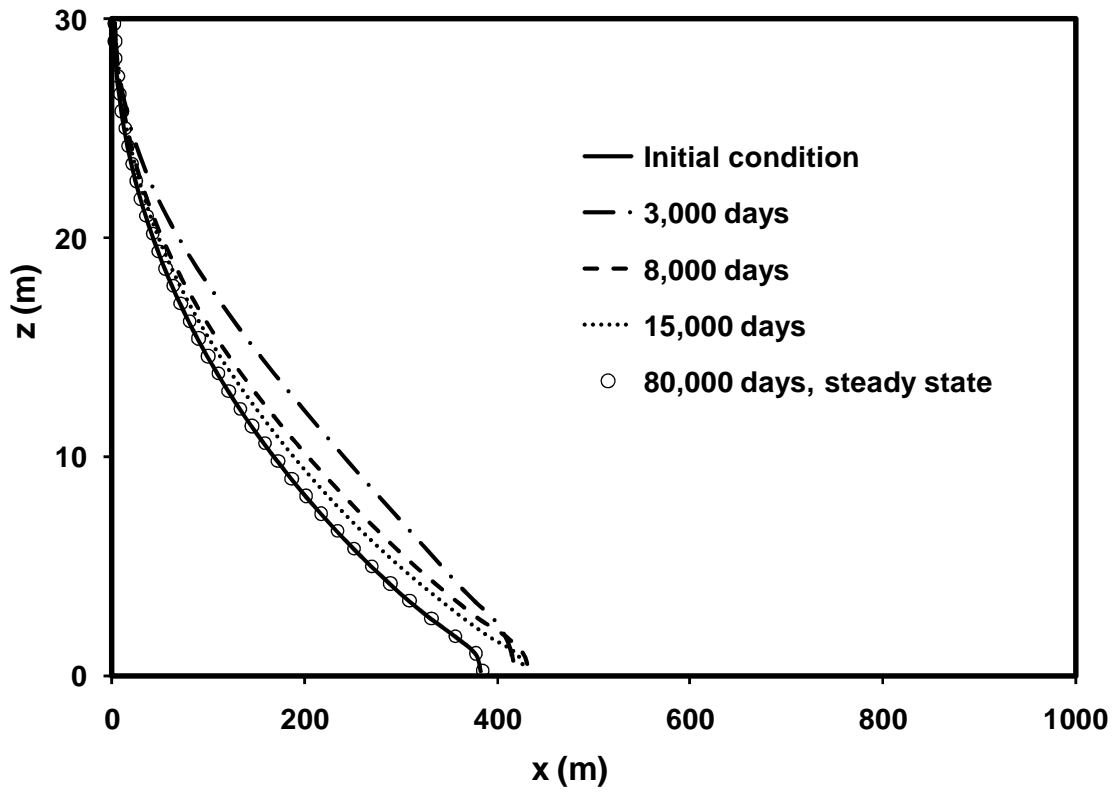
Figure 2.3. Transient salt wedge profiles for the confined system.
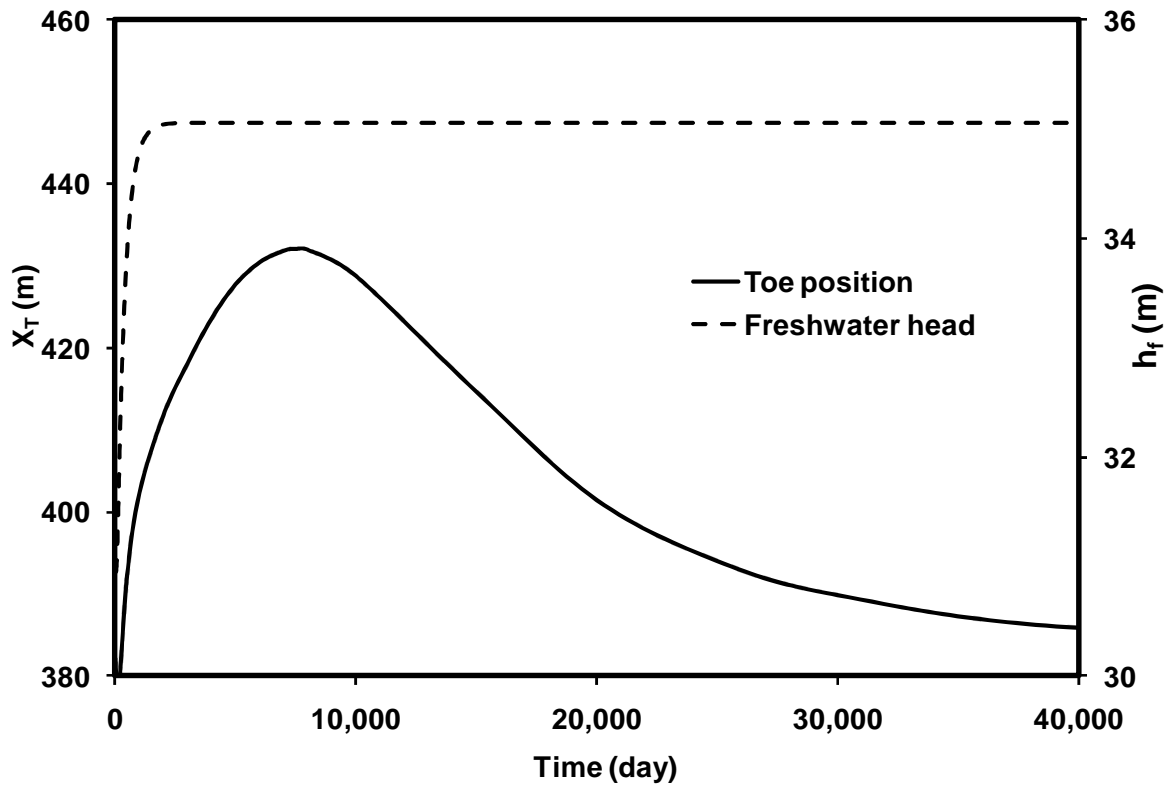
Figure 2.4 Transient variations in the toe position (X_T) and freshwater head (h_f) at the inland boundary.

2.4.2. Sensitivity Analysis of the Self-reversal Process in Confined Systems

2. 4.2.1. Sensitivity to Specific Storage

We first explored the sensitivity of the intrusion mechanism to various values of specific storage (S_s). In this analysis, the value of S_s was varied by an order of magnitude with the range 0.0008 to 0.008 m^{-1}. In all sensitivity simulations, the other parameters were fixed at base-case levels shown in Table 2.1. Figure 2.5a shows the temporal variations in the toe position (X_T) for different values of S_s. The data shows that when S_s was small the system responded rapidly and the intrusion effect was reversed quickly. Also, the maximum intrusion length was small for smaller values of S_s. The maximum values of the predicted saltwater toe position (X_T) were 432, 412, 394, and 386 m for the S_s values 0.008, 0.005, 0.002 and 0.0008 m^{-1}, respectively. The figure shows that when S_s is small (at 0.0008 m^{-1}) the change in the salt wedge location was relatively small even for an extreme sea-level rise of 4 m. The total time required to reach the maximum intrusion level (defined as the duration of intrusion) was 6,000 to 8,000 days. These values appear to be relatively insensitive to S_s. Overall, the extent of saltwater intrusion as indicated by the maximum value of X_T was more sensitive to S_s than the duration of intrusion.

2.4.2.2. Sensitivity to the Magnitude of Sea-level Rise

The sensitivity of the intrusion length to the magnitude of the sea-level rise was explored by varying the sea-level rise within the range of 0.2 to 4 m. Figure 2.5b shows the transient variations in X_T values for various values of sea-level rise. The maximum values of X_T were approximately proportional to the magnitude of sea-level rise. Also, similar to the previous

sensitivity experiment, the time taken to reach the maximum values was about 6,000 to 8,000 days, and this time was relatively insensitive to the magnitude of the sea-level rise.

2.4.2.3. Sensitivity to the Rate of Sea-level Rise

Simulations were completed to test the sensitivity of the intrusion process to changes in the rate of sea-level rise. Literature data indicated that the current rate of sea-level rise observed worldwide has ranged from 2 to 4 mm/year [*McCarthy*, 2009]. Climate change model projections, however, show that the global rate could at least double by the end of this century [*Anderson et al.*, 2010]. A total rise of 4 m was simulated using six different rate scenarios: instantaneous, 1 mm/day for 4,000 days, 0.1 mm/day for 40,000 days, 0.05 mm/day for 80,000 days, and infinite rise at a rate of 0.04 mm/day with $S_s = 0.008$ and $S_s = 0.0008$. Figure 2.5c shows the temporal variations in the simulated toe position (X_T) for all five scenarios. The data demonstrates that the rate of the self-reversal process would depend on the sea-level rise rate. When the rate of rise was low the reversal cycle had a longer duration. The maximum value of the intrusion length, X_T, decreased with decrease in the rate of sea-level intrusion. The time taken to reach the maximum level of intrusion was 7,500, 10,000, 40,000 and 80,000 days for instantaneous, 1 mm/day, 0.1 mm/day, 0.05 mm/day sea-level rise rates, respectively. When sea-level was allowed to rise infinitely at a fixed rate, the results reached an irreversible, quasi steady-state level. It is important to note this irreversible intrusion level was primarily an artifact due the relatively large storage value (of 0.008 m^{-1}) assumed as the base-case parameter. When we reduced the specific storage value by an order of magnitude (to 0.0008 m^{-1}, a more typical value for confined flow) the head information propagated quickly and the lifting effect became continuously active. Therefore, the system with a higher S_s value experienced immediate

reversal and experienced very little intrusion under the continuous-rise scenario. Overall, changes in the rate of sea-level rise influenced the maximum level of intrusion as well as the time required to reach the maximum level. The time required to reach the maximum would, to a large extent, depended on how long the sea rise occurred.

2.4.2.4. Sensitivity to Dispersivity Values

We explored the sensitivity of the intrusion mechanism to dispersivity coefficients by varying the value within the range of 0.5 m to 2 m for longitudinal dispersivity, α_L, and 0.05 m to 0.2 m for transverse dispersivity, α_T. As Abarca et al [2007b] pointed out, changing the values of dispersivity would impact the value of X_T (initial X_T decreased when the dispersivity coefficients were increased). Therefore, we defined a parameter "net change in salt wedge location," which was computed as: maximum value of X_T - initial position of X_T, to quantify the changes. Figure 2.5d shows the temporal variations in the toe position (X_T) for different values of dispersivity. The net change in the salt wedge location was in between 44 and 53 m. The time taken to reach the maximum intrusion level and the peak of X_T values were relatively insensitive to changes in the value of dispersivity coefficient.
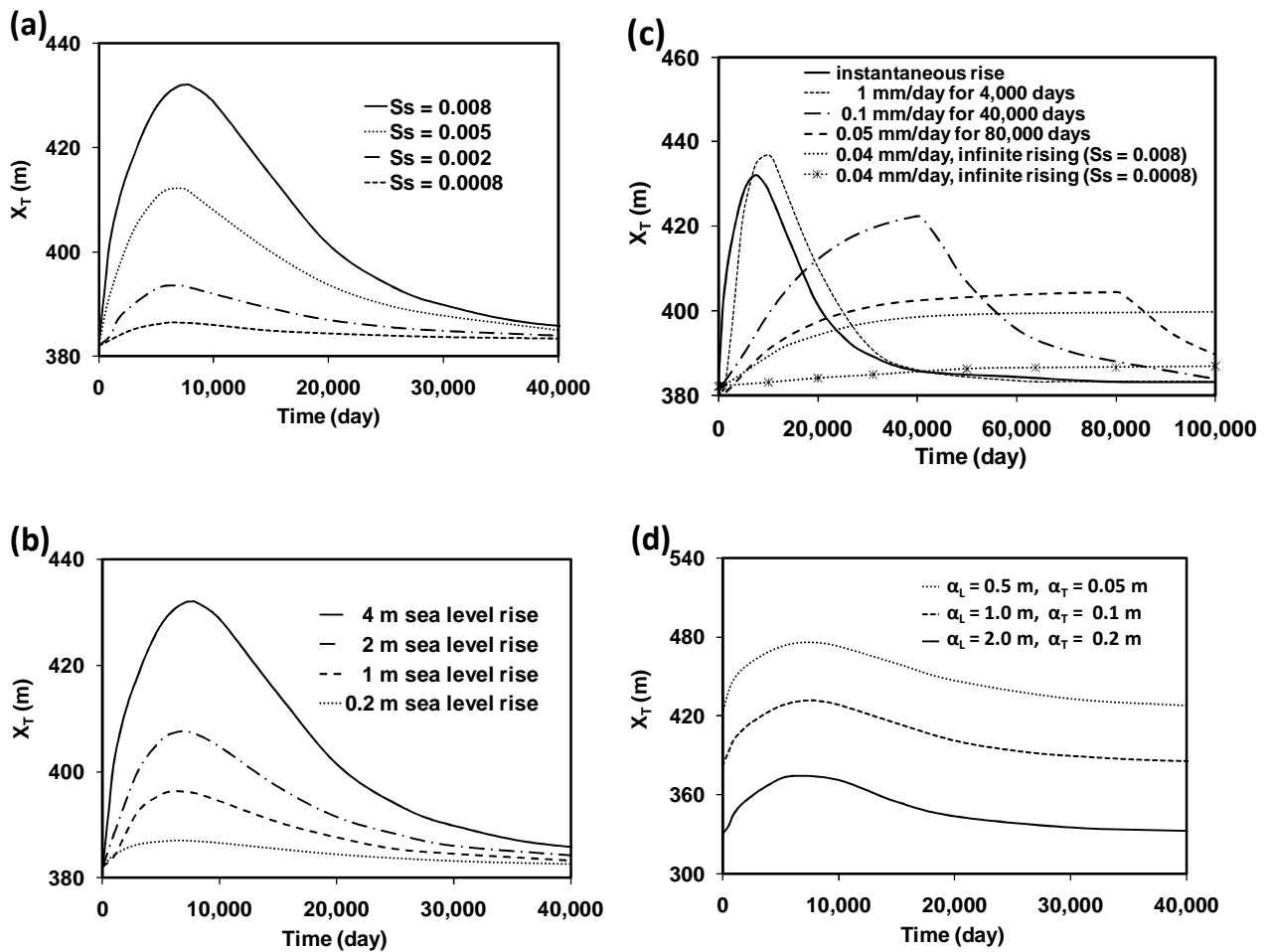
Figure 2.5. Sensitivity of the toe position (X_T) to (a) specific storage, (b) the magnitude of sea-level rise, (c) the rate of sea-level rise velocity and (d) the dispersivity coefficients.

2.4.2.5. Sensitivity to Other Hydrological Parameters

It is important to note that the transient reversal patterns would depend on the values of hydraulic conductivity, recharge rate and ambient groundwater flow. Sensitivity to variations in all these model parameters was also explored in this study. Simpler analytical solutions can be used to intuitively infer the sensitivity to individual variations in K, W and Q values under steady conditions. Werner and Simmons [*Werner and Simmons*, 2009] followed this approach and completed a detailed sensitivity assessment for a steady-state unconfined problem. In this study, we present the results of a selected number of sensitivity tests completed for a transient confined aquifer system using SEAWAT. Figure 2.6a shows the transient variations in X_T values for different hydraulic conductivity values; K values used are: 5 m/day, 10 m/day and 15 m/day. It should be noted that the simulated profiles have different initial X_T since individually changing any one of these parameters (K, W or Q) would alter the steady-state solution of the base problem. The results show that the peak value of X_T (relative to the initial X_T value) would increase, and the responding time would decrease (as expected) when the K value was decreased. Figure 3.6b shows the transient variations in X_T values for various values of Q and W (0.67×base values: $Q = 0.1$ m^3/day and $W = 3.3 \times 10^{-5}$ m/day; base values: $Q = 0.15$ m^3/day and $W = 5 \times 10^{-5}$ m/day; doubled the base values: $Q = 0.3$ m^3/day and $W = 1 \times 10^{-4}$ m/day). The data show that when the amount of freshwater flow was increased the peak value of X_T increased and system also had a shorter responding time. It should be noted that if the transport parameters were scaled consistently (for example, increase K and reduce the Q by a similar factor) then there will be very little variation in the peak value of X_T.
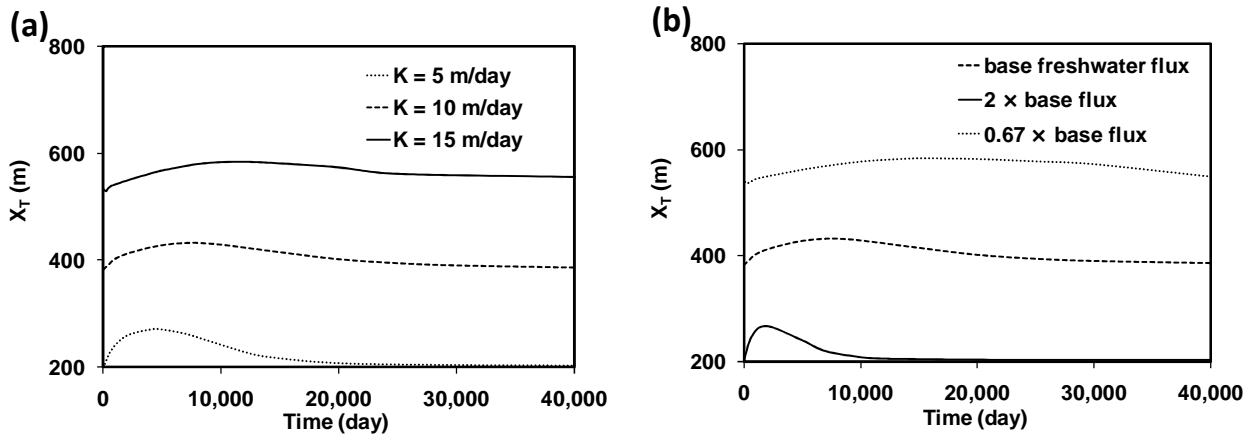
Figure 2.6. Sensitivity of the toe position (X_T) to: (a) hydraulic conductivity and (b) freshwater flux.

2.4.3. Impacts of Sea-level Rise on Unconfined Aquifers

To examine the impacts of sea-level rise on unconfined flow conditions, we completed numerical simulations of an unconfined aquifer with dimensions identical to those used in the confined simulation, except the top layer was modified to simulate unconfined flow. The length of the unconfined aquifer was 1,000 m and the total thickness was 35 m. A numerical grid with $\Delta x = 4$ m, $\Delta y = 1$ m and $\Delta z = 0.4$ m (75 confined layers), and a top unconfined layer of $\Delta z = 5$ m was used. In all unconfined flow simulations, the value of average hydraulic conductivity was set to 10 m/day, total regional freshwater flow (Q) from the right boundary was set to 0.15 m^3/day, and the areal recharge flux (W) was set to 5×10^{-5} m/day. Initially, the regional flow rate was assigned to 0.0019 m^3/day for all confined layers with 0.0048 m^3/day for top unconfined layer (note the top unconfined layer was 1 m as opposed confined nodes which are 0.4 m). After the sea-level rise, the flow rate was again redistributed over the unconfined zone of 4 m. In order to redistribute the same flow of 0.15 m^3/day over an increased saturated aquifer depth, all the confined nodes were assigned a flow of 0.0017 m^3/day and the top 4-m unconfined layer was assigned 0.021 m^3/day. In order to compare unconfined flow simulation results against confined flow results, an identical instantaneous sea-level rise (rise from 30 to 34 m) scenario was assumed. The specific storage, S_s, was set to 0.008 m^{-1} for all confined layers, and specific yield, S_y, was set to 0.1 for the top unconfined layer.

We first completed a base-case, steady-state simulation for the unconfined system to generate the initial conditions that existed prior to the sea-level rise. Figure 2.7 compares the steady-state salt wedge predicted for the unconfined flow system with the wedge predicted for a similar confined flow system (data from Figure 2.2). The figure shows the both wedges are almost

identical, indicating that both confined and unconfined systems would behave in a similar manner at steady-state conditions. The similarity between the two steady-state solutions can also be explained mathematically, as shown in Appendix 5.

To understand the impacts of sea-level rise on the unconfined aquifer, we instantaneously raised the sea-level by 4 m and let the system reach steady state. Figure 2.8 compares the initial and final steady-state saltwater wedge profiles in the unconfined system (dotted and continuous lines). These profiles show that, unlike the confined system (compare with Figure 3 results), the saltwater intrusion process is not reversible for the unconfined system. In unconfined aquifers, the initial location of the toe XT_i and the final location of the toe position XT_f are distinctly different. This is because, under unconfined conditions, the sea-level rise increases in the saturated thickness (or transmissivity) of the aquifer. This increased transmissivity allows the wedge to penetrate further into the system, resulting in a new steady-state condition. Comparing the initial and final salt-wedge profiles indicates the initial salt wedge was approximately raised by 4 m, similar to the level of sea-level rise. The groundwater level also rose over the entire aquifer by about 4 m (as illustrated in Figure 2.1b), all the way to the inland boundary (the predicted groundwater raise at the inland boundary was similar to the data shown in Figure 2.4). These data indicate that the aquifer lifting process is active in the unconfined system. The lifting process, however, was not able to fully reverse the wedge location since the system evolved from a steady-state solution for the 30-m thick aquifer (with initial toe, XT_i, at about 382 m) to a new steady-state solution for the 34-m thick aquifer (with final toe, XT_f, at about 510 m). The data points (marked with circles) shown in the figure are steady-state wedge data predicted for a 34-m thick "equivalent confined aquifer." As expected (see Appendix A for an analytical analysis),

the final unconfined steady-state solution matched with an equivalent confined aquifer solution with an appropriate value of aquifer thickness.

Figure 2.9 compares the results of transient changes in toe length predicted for the following three systems: Case-1) standard base-case confined system of 30 m thickness (same as the data shown in Figure 2.2); Case-2) unconfined flow system with base-case parameters; and Case-3) unconfined system with very high S_s value (0.02 m^{-1}). It is important to note the S_s value used for Case-3 is unrealistically high and this conceptual simulation was completed to demonstrate the existence of certain subtle self-reversal mechanisms. Several observations can be made from the results presented in Figure 2.9. All three solutions started at the initial toe location XT_i = 382 m and for about 1,000 days the unconfined solutions were approximately equal to the confined flow solution. After this time, the unconfined model solutions started to diverge. The Case-2 unconfined flow simulation reached the final steady-state toe position, XT_f, after about 50,000 days, and the system did not show any reversal effect. However, when we repeated the unconfined simulation using high S_s values (Case-3) we could clearly observe the reversal effect. Also, as expected, Case-3 required more time (about 100,000 days) to reach steady-state final toe position XT_f. In summary, the aquifer lifting effect is active in unconfined systems but it is difficult to observe any reversal effects in transient unconfined systems due to the changes in the aquifer transmissivity. When an appropriate value of aquifer thickness was used, the steady-solution for an unconfined flow system would be almost identical to an "equivalent confined flow system." The storage available within fully-saturated layers (which act as confined layers) are typically very low and this would allow rapid propagation of head perturbations; therefore, it is difficult to observe reversal effects in any realistic unconfined aquifers.
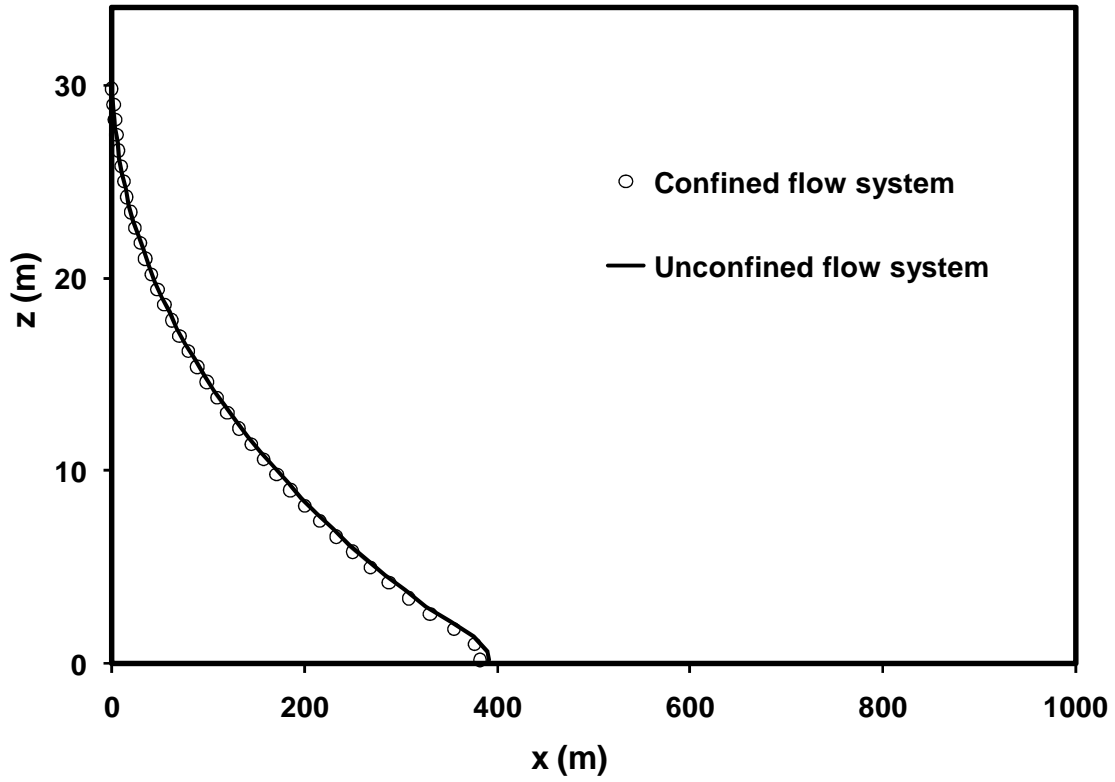
Figure 2.7. Comparison of steady-state salt wedges predicted before the sea-level rise (sea level at 30m) in the unconfined- and confined-flow systems.
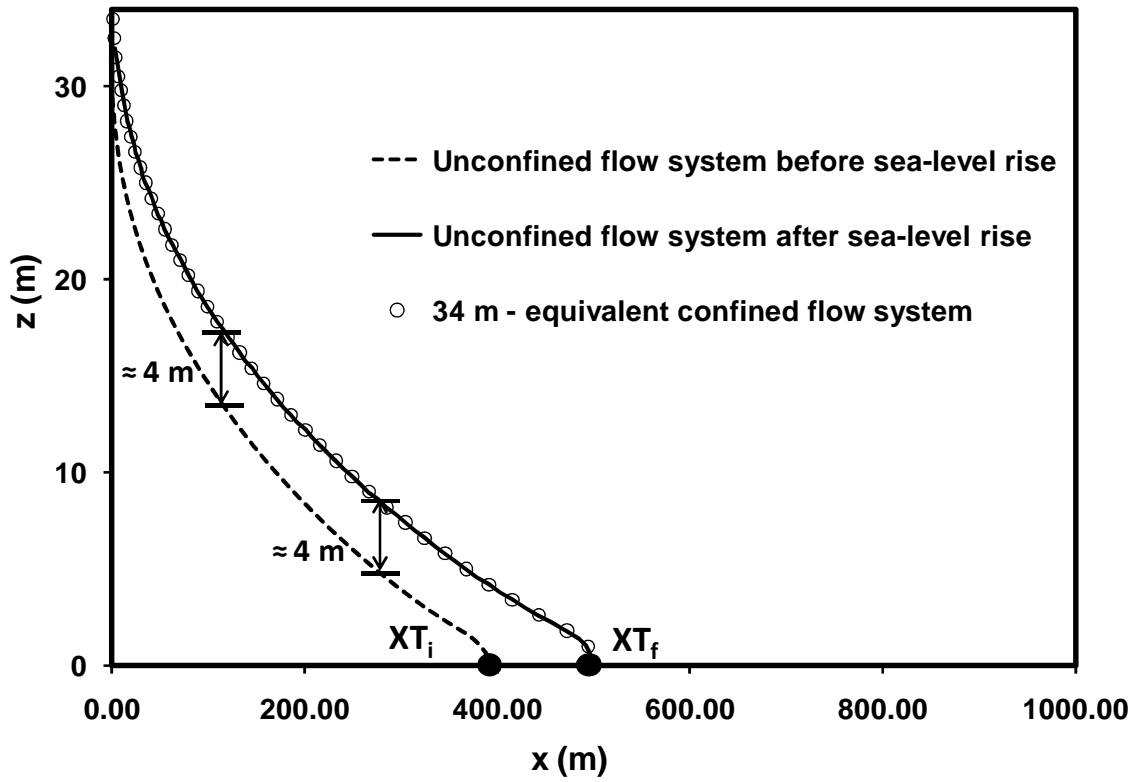
Figure 2.8. Comparison of steady-state salt wedges predicted before the sea-level rise in the unconfined system, after the sea-level rise in the unconfined system, and in an equivalent 34-m thick confined-flow system.
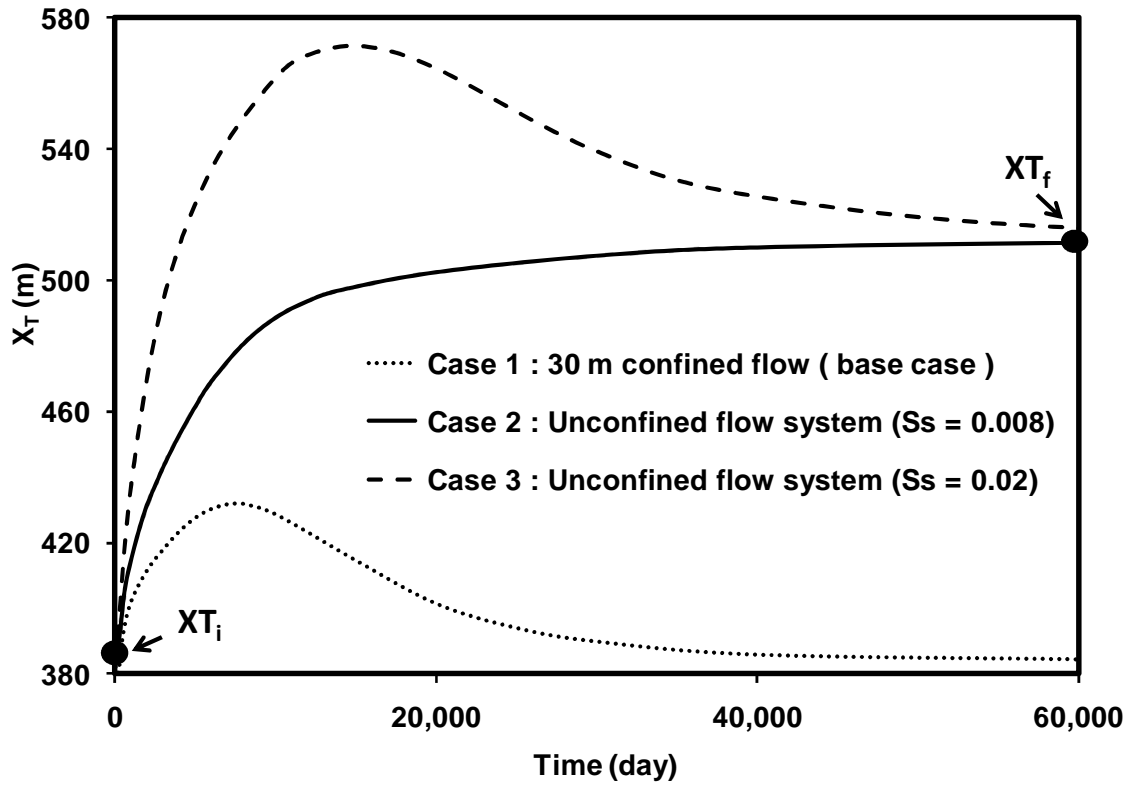
Figure 2.9. Comparison of transient variations in toe positions (XT) predicted for the confined and unconfined flow systems.

2.5 Conclusions

Detailed numerical experiments were completed using the MODFLOW-family computer code SEAWAT to study the transient effects of sea-level rise on saltwater wedge in confined and unconfined aquifers with vertical sea-land interface. The simulation results show that if the ambient recharge remains constant, the sea-level rise will have no impact on the steady-state salt wedge in confined aquifers. The transient confined-flow simulations help identify an interesting self-reversal mechanism where the wedge, which initially intrudes into the formation due to sea-level rise, would be naturally driven back to the original position. However, in unconfined-flow systems this self-reversal mechanism would have lesser effect due to changes in the value of the effective transmissivity (or average aquifer thickness). The increased trasmissivity resulted in a redistribution of freshwater flux at the inland boundary condition. Both confined and unconfined simulation experiments show that rising seas would lift the entire aquifer and this lifting process would help alleviate the overall long-term impacts of saltwater intrusion.

The sensitivity simulations show that the rate and the extent of the self-reversal process would depend on the value of specific storage (S_s) and the rate of sea-level rise. When the rate of rise was low the reversal cycle had a larger duration. Overall, the changes in the rate of sea rise had relatively less influence on the maximum level of intrusion and more influence on the time taken to reach the maximum level. On the other hand, variation in S_s values was more sensitive to the maximum level of intrusion than the duration of intrusion (the time taken to reach the maximum value).

It is important to note that the results presented in the conceptual modeling study are based on simulations completed for idealized rectangular aquifers with homogeneous aquifer

properties. While the results are useful for developing a large-scale conceptual understanding of the impacts of sea-level rise, evaluation of true impacts would require detailed site-specific modeling efforts [*Abarca et al.*, 2007a; *Loáiciga et al.*, 2011]. A better understanding the self-reversal mechanism (both its spatial and time scales) identified in this study would have an enormous implication on managing the impacts of sea-level rise in coastal groundwater aquifers. The results, however, do not imply that one could simply ignore climate change effects on saltwater intrusion process. Rather it implies that we can minimize its risks based on a sound scientific understanding of the transport processes and by developing pro-active management strategies that are appropriate to unconfined aquifers and confined aquifers. It is important to note that this study assumes the fluxes in the system would remain constant. However, site-specific climate change effects could greatly alter the recharge and regional fluxes (these natural hydrological fluxes can change due to variations in rainfall patterns), therefore the overall problem should be managed in the context of large-scale variations in hydrological fluxes expected to be induced by climate change effects. In addition, Loáiciga et al. [*Loáiciga et al.*, 2011] pointed out that variations in groundwater extraction (anthropogenic fluxes) was the predominant driver of sea water intrusion in a model that simulated sea-level rise scenarios for the City of Monterrey, California. Finally, it is very likely that rising heads might increase evapo-transpiration fluxes. This could impact the overall hydrological budget resulting in less recharge reaching the coastal area and this will hinder the self-reversal process. Therefore, site-specific management models for coastal areas should carefully integrate changes in both natural and anthropogenic fluxes with various sea-level rise scenarios.

Chapter 3

INVESTIGATION OF SALTWATER INTRUSION PROCESSES USING LABORATORY
EXPERIMENTS INVOLVING FLUX-TYPE BOUNDARY CONDITIONS

3.1.Introduction

Saltwater intrusion is a natural process where sea water would advance into coastal
groundwater aquifers due to the density difference between saline and fresh waters creating a
wedge that evolves landward. The horizontal extent of saltwater intrusion could range from a
few meters to many kilometers [*Barlow and Reichard*, 2010]. Several natural and anthropogenic
processes can enhance the effects of saltwater intrusion. For example, the water supply
operations in coastal regions may depend on pumping freshwater from local aquifers, and these
pumping activities can exacerbate both vertical and horizontal salt intrusion processes. Droughts
induced by climate change effects could result in the loss of freshwater resources and enhance
saltwater intrusion. Several modeling and field studies have provided evidence that climate
change could decrease the net freshwater input to groundwater resources [*Feseker*, 2007;
Loáiciga et al., 2011; *Masterson and Garabedian*, 2007; *Oude Essink*, 2001; *Oude Essink et al.*,
2010; *Ranjan et al.*, 2006; *Rozell and Wong*, 2010; *Yu et al.*, 2010], and this could aggravate the
impacts of saltwater intrusion. Climate change studies estimate that the global sea level could
increase between 18 cm and 59 cm this century [*IPCC*, 2007]; other worst-case scenario
predictions have forecast higher sea-level rises up to 180 cm [*Vermeer and Rahmstorf*, 2009],
which could result in more severe saltwater intrusion.

The number of scientific investigations related to climate change effects have increased
rapidly in the last decade [*Green et al.*, 2011]. Most of these investigations are based on the

premise that climate change will have severe adverse impacts on almost all natural systems including groundwater systems. As pointed out by *Kundzewics and Dölle* [2009], flat areas such as deltas and coral islands are expected to be inundated by rising seas leading to reduced freshwater availability. According to an extreme case reported by *Yu et al.* [2010], about a meter sea-level rise would inundate and contaminate over 18% of the total land in Bangladesh, threatening to physically displace about 11% of their population.

Chang et al. [2011] recently presented some interesting counter-intuitive results indicating that sea-level rise would have no impact on saltwater intrusion in certain idealized confined systems that ignore marine transgression effects, such as a tidal effect and seasonal variation. Their results show that rising seas would lift the entire water table, and this lifting process has the potential to alleviate the overall long-term impacts of saltwater intrusion via a natural self-reversal process. *White and Falkland* [2009] reviewed previously published field datasets and concluded that the freshwater lenses in several atoll islands might not be severely affected by sea-level rise up to 1 m, as long as the land mass is not lost due to inundation of the edges of these islands. On the other hand, potential variations in the recharge patterns, resulting from changes in the rainfall levels, are expected to have much larger impact on the overall water budget of these islands. *Rozell and Wong* (2010) used climate change scenarios available in the Intergovernmental Panel on Climate Change 2007 (IPCC) report and found that only a small portion of Shelter Island, located New York, USA, would experience inundation and salt-water intrusion even when the sea level was assumed to increase more than three times higher than those values reported in the IPCC report. Some of these conflicting results imply that the impacts of climate change on saltwater intrusion should be carefully predicted and managed at a

local scale, on a case-by-case basis, since the overall impacts would depend on various hydrological factors including spatial and temporal variations in rainfall/recharge patterns.

Werner and Simmons [2009] categorized saltwater intrusion problems into two types depending on how the freshwater would enter the aquifer. The first type of system is known as a head-controlled system, where the groundwater level fixed at the inland boundary would transmit various rates of freshwater flow depending on aquifer properties. The second type is a flux-controlled system where the net freshwater flow entering at the aquifer inland boundary is set to a constant flow rate. From a fundamental point of view, even in the head-controlled system the changes in saltwater intrusion patterns would be essentially due to the net decrease or increase in freshwater flow transmitted through the system. Therefore, the amount of freshwater flux moving through the system is an important fundamental parameter that would control saltwater intrusion effects. *Chang et al.* [2011] demonstrated how the impacts of sea-level rise on both unconfined and confined systems could be strongly influenced by the changes in fresh-water fluxes. They also found that when the fresh water flux is held constant the sea-level rise would have no impact on the steady-state saltwater wedge profiles of confined aquifers. Kuan [2012] reported that the saltwater wedge and the resulting upper saline plume in unconfined coastal systems will be affected by the changes in the regional freshwater influx induced by various tidal conditions. These studies have demonstrated the importance of understanding the effects of changes in different types of groundwater fluxes on saltwater intrusion mechanisms.

The objective of this research is to conduct experimental studies to investigate the impacts of variations in regional and areal-recharge fluxes on saltwater intrusion in unconfined aquifers. In this effort, we have explored two types of flux-controlled systems: one driven by regional flow delivered from the inland freshwater boundary and another driven by a fixed

amount of recharge flow distributed from the top. In the following sections, we refer to these two systems as regional-flux system and areal-recharge flux system, respectively. The results from the experiments were used to develop a better understanding of the influence of different types of flux-boundary conditions on the saltwater intrusion process, especially under transient flow conditions.

3.2 Methods

3.2.1 Experimental Approach

Figure 3.1 shows the experimental methods employed in this study. The laboratory setup shown in Figure 3.1a was used to conduct regional-flux aquifer (RFA) experiments, and Figure 3.1b was used to conduct areal-recharge flux aquifer (AFA) experiments. All the experiments were completed in a sand tank with dimensions: 50.5 cm × 28 cm × 2.2 cm. We used a relatively narrow tank to simulate a two-dimensional system that represents cross-sectional flow in an unconfined aquifer. As shown in the figure, the sand tank has three distinct chambers: an inlet chamber, porous media chamber, and an outlet chamber. In the regional flux experiment, the right inlet chamber was used to deliver freshwater flow to the system. The sea level variations were simulated by adjusting the saltwater head at the left outlet chamber. The central porous media chamber was filled with silica beads of diameter 1.1 mm. The beads were packed under saturated conditions to prevent the trapping of air bubbles inside the tank. The average hydraulic conductivity value of the system was estimated to be 1.46 cm/s. Other experimental methods used here were similar to those used in our previous experiments reported in Goswami and Clement [2007] and Abarca and Clement [2009]. It is important to note that our previous experimental studies and those published by others [*Karasaki et al.*, 2006] have used constant-

head boundary conditions; here we have employed two different types of flux boundary conditions. To simulate the areal recharge flux boundary condition, we used a multi-head peristaltic pump that delivered flow at various injection points. The flow was divided equally and was distributed from four outlet tubes. The tubes were placed on the top of a porous media chamber (well above the water table) at distances of 10 cm, 20 cm, 30 cm, and 40 cm away from the inlet chamber. To simulate the constant regional flux condition, we used the same multi-head pump that injected a constant amount of flow via a single outlet which was placed into the right chamber. All the saltwater intrusion experiments were recorded using a Panasonic video camera (HDC-HS250) and the photographs were later post-processed using methods described in Goswami and Clement [2007]. A commercial food dye was added at a ratio of 50 ml per 20 L of saltwater to help differentiate the saltwater from ambient fresh water. The measured density of the colored saltwater was 1.027 g/cm^3.
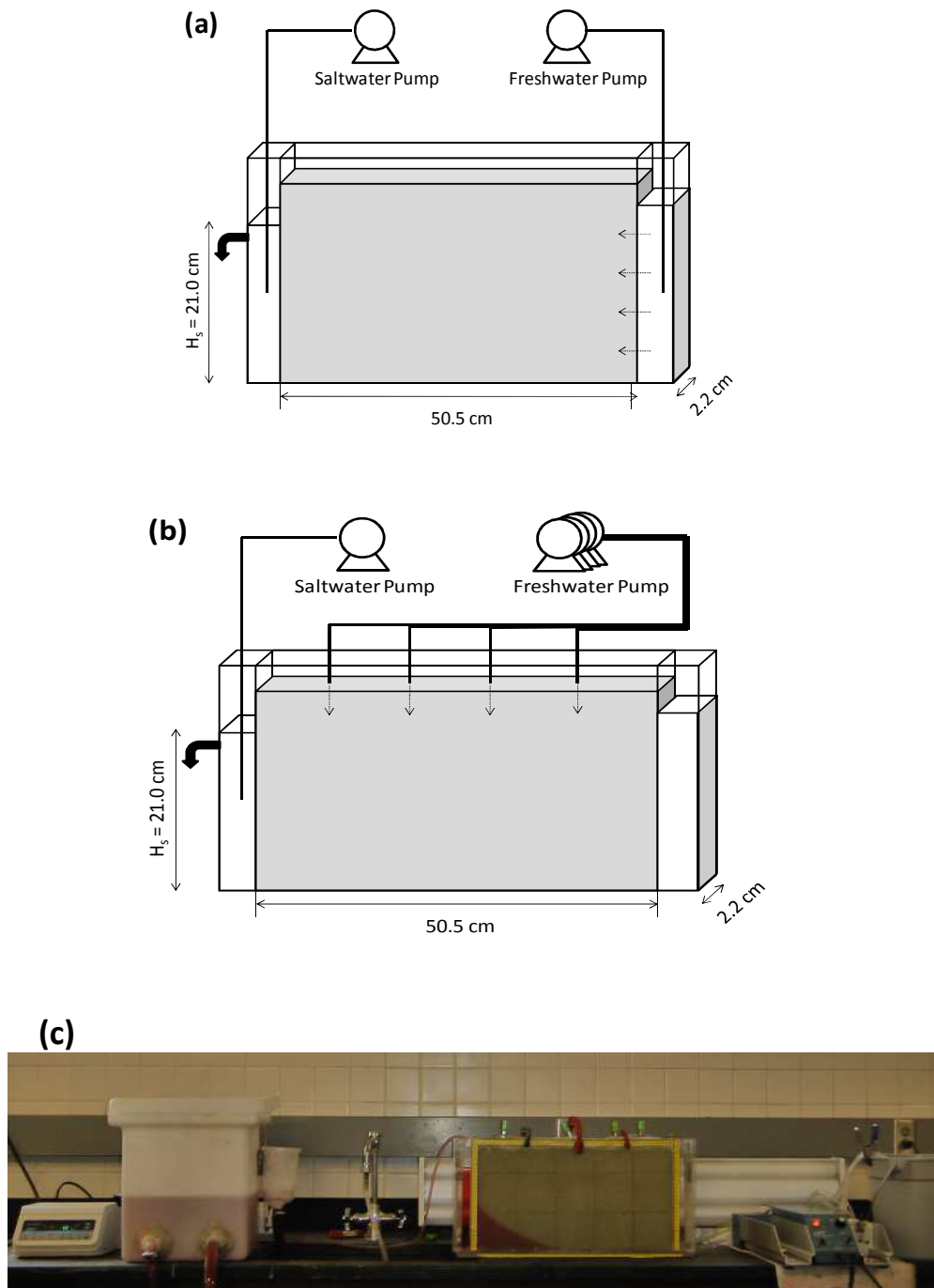
Figure 3.1. Schematic diagram of the (a) regional-flux and (b) areal-recharge flux experiments and (c) photograph of laboratory setup.

3.2.2 Numerical Modeling Approach

The MODFLOW-family variable density flow code SEAWAT [*Guo and Langevin*, 2002] was used to model the experimental data. The fully implicit option and the total variation diminishing (TVD) package were used in all our simulations. The code has been widely tested by solving various benchmark problems including *Simpson and Clement* [2003] and *Simpson and Clement* [2004]. In our model, the origin of an x-z coordinate system was set at the lower left-hand corner of the plane. A uniform finite-differences grid of size 0.5 cm (total of 102 cells in the x-direction) was used to discretize the horizontal direction. Forty-two uniform confined layers of width 0.5 cm were used to discretize the vertical direction; in addition, a single unconfined layer of width 1 cm was used to represent the top region. The depth of the top layer was selected such that the layer would remain unconfined (i.e., it did not fully drain or overfill) in all our simulations (note that the freshwater head in the tank varied from 21.6 to 22.0 cm, measured from the bottom, in our transient experiments and the saltwater head was set to 21.0 cm). The lower boundary nodes were set to no-flow conditions. The longitudinal (α_L) and transversal (α_T) dispersivity coefficients were assumed to be 0.05 cm and 0.005 cm, respectively; these are the values previously used by *Abarca and Clement* [2009]. The value of specific storage (S_s) was set to 10^{-6} cm^{-1} for the confined layers and the value of specific yield (S_y) was set to 0.1 for the top unconfined layer. The measured values of freshwater density and the saltwater density were 1.000 and 1.027 g/cm^3, respectively. Using the standard density-concentration slope factor of 0.714, the value of salt concentration was estimated to be 0.378 g/cm^3. The concentration value was also verified using data for the amount of salt used to prepare the saltwater solution. The entire flow domain was assumed to be initially filled with

saltwater, and a constant rate of freshwater flow was injected at the boundary to simulate the desired initial steady-state condition.

Table 3.1. Summary of numerical model parameters

Property	Symbol	values
Horizontal length	L	50.5 cm
Saltwater elevation	h_s	21 cm
Hydraulic conductivity	K	1.46 cm/s
Specific yield,	S_y	0.1
Specific storage,	S_s	0.00001cm^{-1}
Longitudinal dispersivity	α_L	0.05 cm
Transverse dispersivity	α_T	0.005 cm
Saltwater concentration	Cs	0.0378 g/cm3
Saltwater density	ρ_s	1.027 g/cm3
Freshwater density	ρ_f	1.000 g/cm3

Table 3.2. Summary measured and modeled flows

Experiment	Experimentally measured flows in the sand tank (2.2 cm wide)	Numerical flows for unit width model
RFA-test (SS1, SS3)	0.832 cm^3/s	0.378 cm^3/s (0.0086 cm^3/s for 42 confined cells, 0.017 cm^3/s for one unconfined cell)
RFA-test (SS2)	0.463 cm^3/s	0.211 cm^3/s (0.0048 cm^3/s for 42 confined cells, 0.009 cm^3/s for one unconfined cell)
AFA-test (SS1, SS3)	1.111 cm^3/s	0.505 cm^3/s (recharge rate is 0.0100 cm/s)
AFA-test (SS2)	0.755 cm^3/s	0.343 cm^3/s (recharge rate is 0.0068 cm/s)

3.3 Results

3.3.1 . Regional-Flux Experiments

We first completed a regional flux experiment to study the transient changes in saltwater intrusion patterns when the flux was varied at the right boundary. The saltwater level at the left boundary was fixed at 21 cm. Figure 3.2 shows the digital data collected for both advancing-wedge and receding-wedge experiments. The time levels required for conducting these experiments were estimated *a priori* from preliminary numerical simulations. To simulate the initial condition, a constant rate of freshwater (0.832 cm^3/s, see Table 4.2) was injected into the right chamber and the system was allowed to reach a steady-state pattern (designated as SS1 in Figure 3.2). To start the transient intruding conditions, the flow rate was instantaneously reduced from 0.832 to 0.463 cm^3/s (about 56% of the initial flow). The transient data were recorded for 90 min, after which the system reached the second steady-state condition (designated as SS2 in Figure 3.2). The receding-wedge experiment was then initiated by increasing the amount of freshwater flow back to the initial rate of 0.832 cm^3/s. This allowed the wedge to recede back towards the saltwater boundary and the system reached the third steady-state condition (designated as SS3 in Figure 3.2) after 60 mins.

Numerical simulations were completed using SEAWAT. The numerical model is assumed to be a unit-width aquifer and hence the total flow rate used was set to 0.378 cm^3/s; the real sand tank was, however, 2.2 cm wide and the measured experimental flow rate was 0.832 cm^3/s (Table 3.2 provides a summary of these conversions). In the model, the initial total flow of 0.378 cm^3/s was distributed into 0.0086 cm^3/s over 42 confined cells of thickness 0.5 cm; in addition, a 1-cm thick unconfined cell was used and it received a flow rate of 0.017 cm^3/s. To simulate the reduced freshwater flow condition, the flow rates for the confined cells were set to

0.0048 cm^3/s and the top unconfined layer flow was set to 0.009 cm^3/s. The results of the numerical model are compared against the experimental data in Figure 3.3. In the figures, -dot-shaped symbols represent experimental observations and the continuous lines represent numerical prediction of 50% concentration contour. The figures show excellent match between the experimental data and model predictions. The toe length, X_T, measured at the bottom of the aquifer is a standard metric used for delineating the location of a wedge [*Chang et al.*, 2011; *Watson et al.*, 2010; *Werner and Simmons*, 2009; *Werner et al.*, 2011]. However, in this study, due to some physical irregularities at the bottom joint of the tank (occurred due to smearing of the excess welding glue outside the tank) prevented us from accurately viewing the wedge at the bottom of the sand tank. This has introduced some uncertainties in measuring the length of the saltwater toe X_T (wedge extent at the bottom). To avoid any mismatch due to these uncertainties, we compared the values of $X_T@_{0.75}$ (i.e., the toe length estimated at 0.75 cm above the tank bottom) against numerical predictions for $X_T@_{0.75}$. Note we selected 0.75 cm since this height conveniently corresponded to the center of a second numerical model layer. Using this upper location allowed us to avoid the observational problem at the bottom of the physical model. Figure 3.4 compares $X_T@_{0.75}$ predicted by SEAWAT against those values estimated for the transient experimental data for both advancing and receding experiments. The figure shows that the numerical model was able to predict the saltwater toe lengths of both intruding and receding wedges.

Transient advancing wedge

0 min (SS1)   10 min   90 min (SS2)

Transient receding wedge

0 min (SS2)   10 min   60 min (SS3)
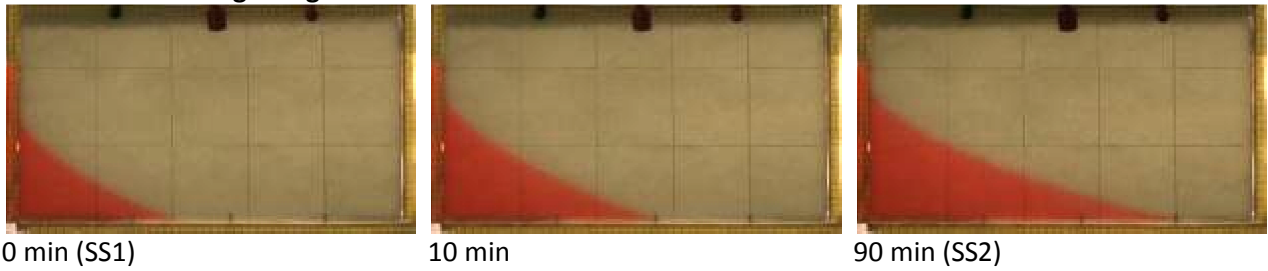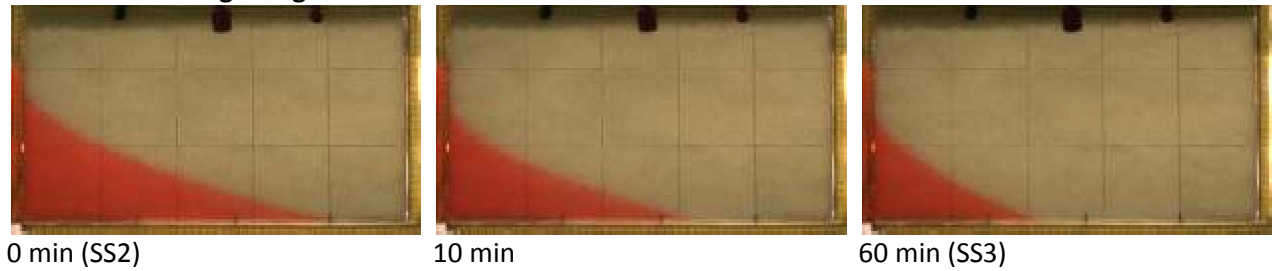
Figure 3.2. Transient variations in the salt-wedge patterns due to changes in the regional flux at the right boundary. The top figure shows intruding transport conditions when the flux was reduced from 0.833 cm^3/s to 0.467 cm^3/s, and the bottom figure shows receding transport conditions when the flux was increased from 0.467 cm^3/s to 0.833 cm^3/s.
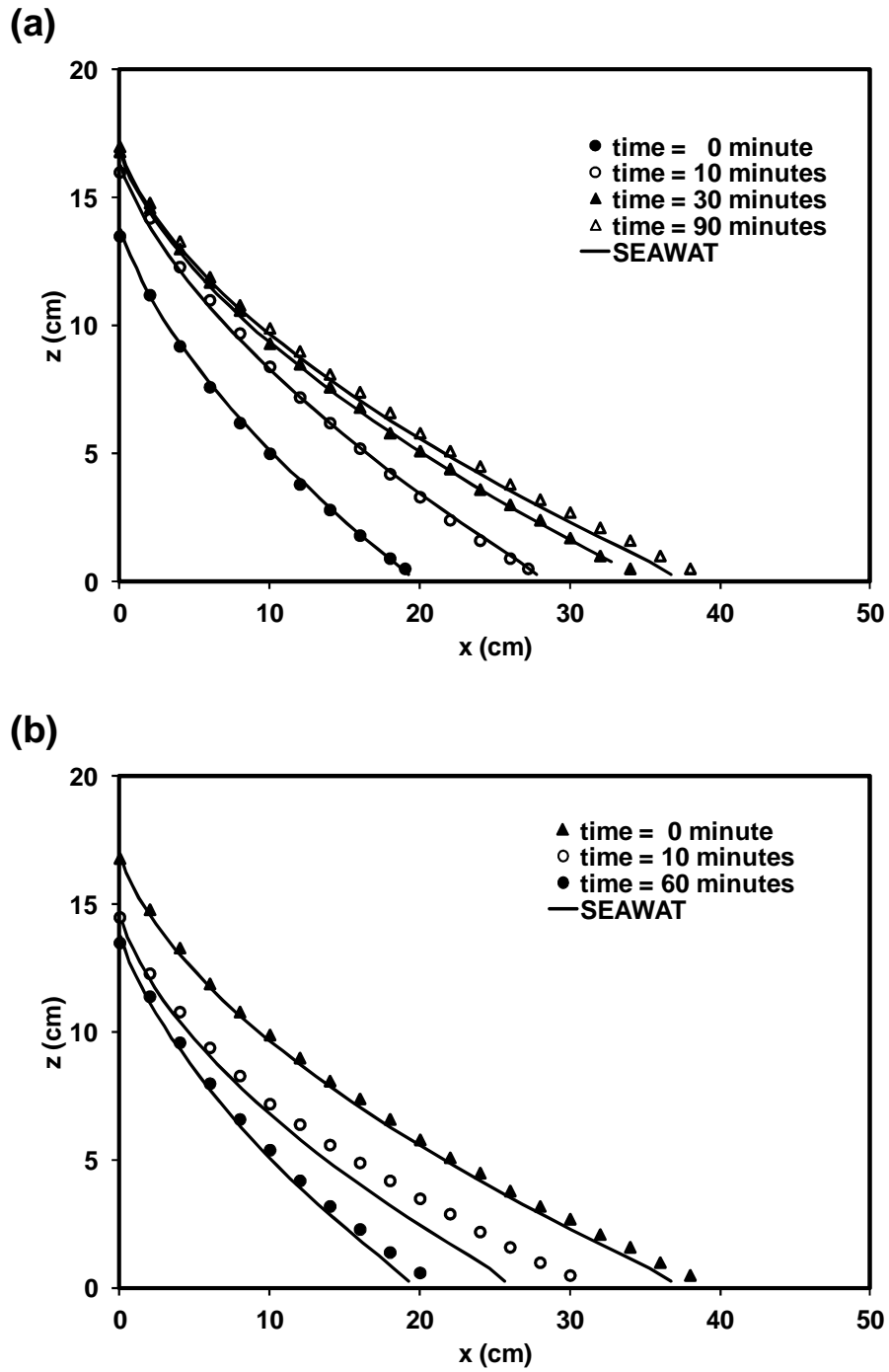
Figure 3.3. Comparison of experimental data model predictions of transient salt wedges for the regional-flux system: a) advancing-wedge experiment, and b) receding-wedge experiment.
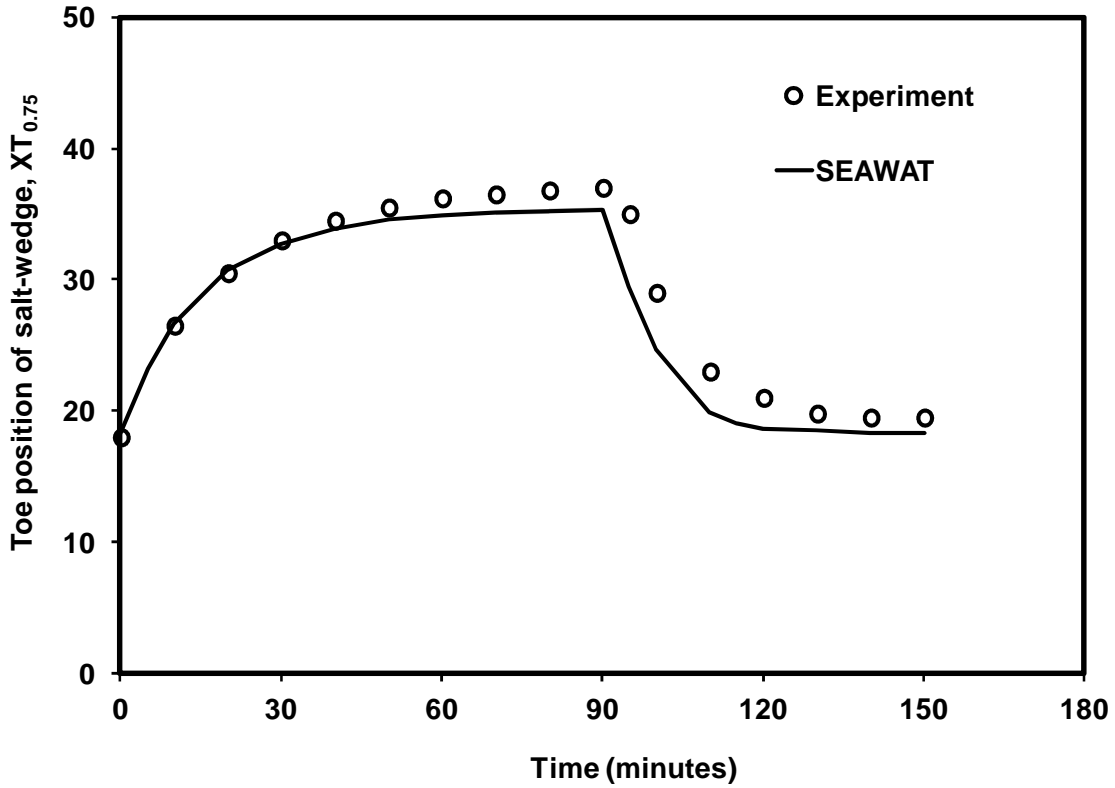
Figure 3.4. Comparison of experimental and model-simulated toe positions estimated at 0.75 cm

above tank bottom in the regional-flux experiment

3.3.2 Areal-Recharge Flux Experiments

The areal-recharge flux experiments were completed to study the extent of saltwater intrusion when the recharge-flux varied at the top of the model. In all these experiments, the saltwater level was fixed at 21 cm at the left boundary. Figure 3.5 shows the digital data for both advancing- and receding-wedge experiments. The time levels and flow rates required for conducting these areal-recharge flux experiments were estimated from preliminary test simulations. Note that the employed inflow freshwater rate in the areal-recharge test was larger than the regional-flux test; this increase was required to create a wedge profile similar to the previous test (see Table 3.2 for flow data). The wedge in the areal-recharge experiment would have advanced less into the flow tank if we would have set the volumetric inflow rates for the area-recharge flux experiment to be identical to the regional- flux experiment. To begin the areal-flux experiment, a constant total freshwater flow rate of 0.505 cm3/s was injected at the top of the tank and the system was allowed to reach a steady-state pattern (designated as SS1 in Figure 3.5). To initiate transient conditions, flow rate was instantaneously reduced to 0.343 cm^3/s (about 68% of the initial flow rate), which then allowed the wedge to advance to the right, towards the flux boundary, by approximately 20 cm. This transient data was recorded for 90 min, after which the system reached the second steady-state condition (designated as SS2 in Figure 3.5). Then, the receding-wedge experiment was initiated by increasing the amount of freshwater flow back to the initial rate of 0.505 cm^3/s. The wedge started to recede backward towards the saltwater boundary and reached the third steady state (designated as SS3 in Figure 3.5) and the transport data was recorded for 60 mins.

Numerical simulations were completed using SEAWAT. In the numerical model, the initial areal-recharge rate of 0.010 cm/s was distributed using the recharge package over the top

unconfined layer. To simulate the instantaneous reduction in the freshwater flow rate, the recharge rate was reduced to 0.0068 cm/s. The numerical predictions are compared against the experimental data in Figure 3.6. The figure shows good match between the experimental data and numerical predictions. Similar to previous experiments, in order to avoid the observational errors associated with our tank bottom, we compared the experimental values of X_T estimated at 0.75 cm against the corresponding X_T values computed by the numerical model. The results shown in Figure 3.7 compare the transient variations in toe length ($X_T@_{0.75}$) predicted by SEAWAT against data for both intruding and receding areal-recharge flux experiments. Results indicate that the model was able to predict the experimental data well.

Transient advancing wedge

0 min (SS1)   10 min   90 min (SS2)

Transient receding wedge

0 min (SS2)   10 min   60 min (SS3)
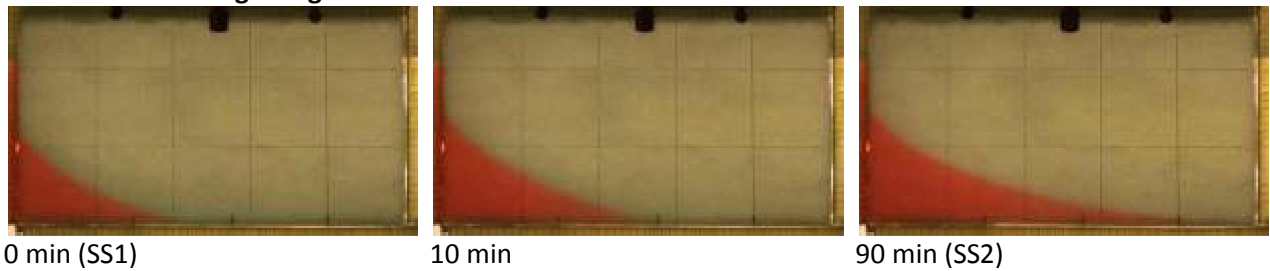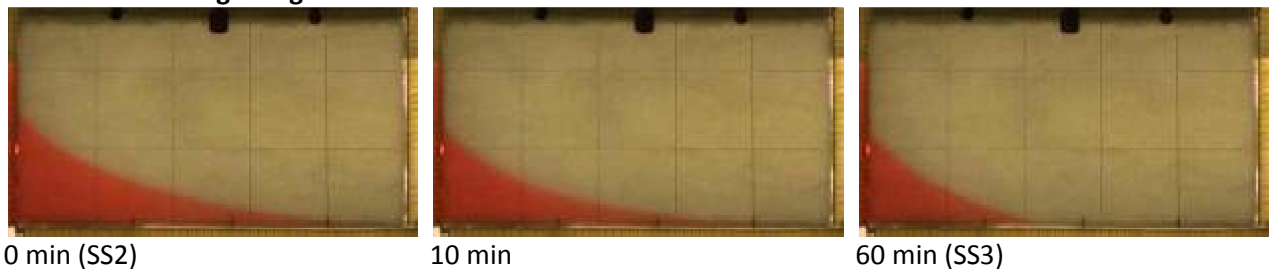
Figure 3.5. Transient variations in the salt-wedge patterns due to changes in the areal flux values. The top figure shows intruding transport conditions when the flux was reduced from 1.133 cm^3/s to 0.733 cm^3/s, and the bottom figure shows receding transport conditions when the flux is increased from 0.733 cm^3/s to 1.133 cm^3/s.
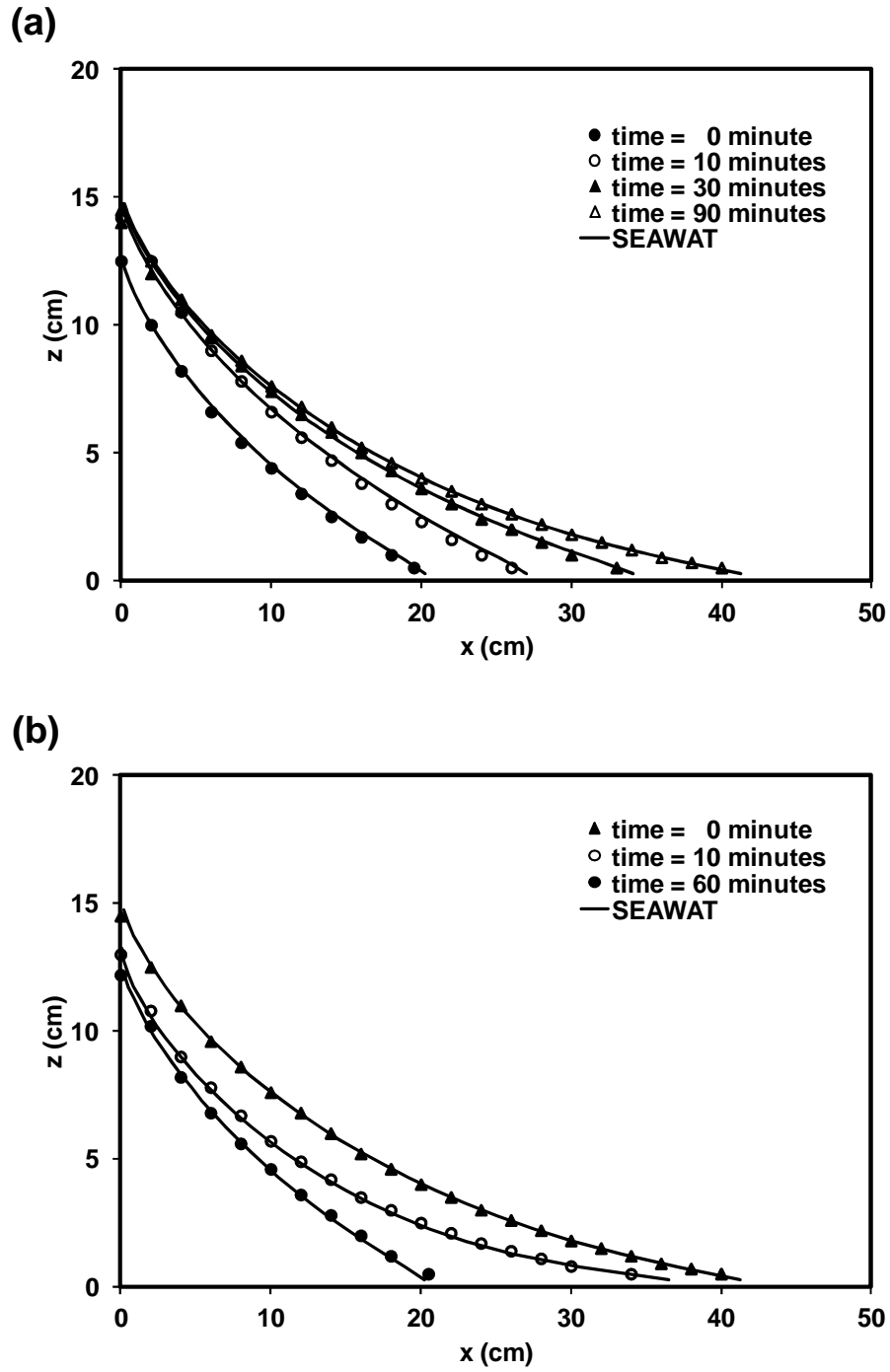
Figure 3.6. Comparison of experimental data model predictions of transient salt wedges for the areal-flux system: a) advancing-wedge experiment, and b) receding-wedge experiment.
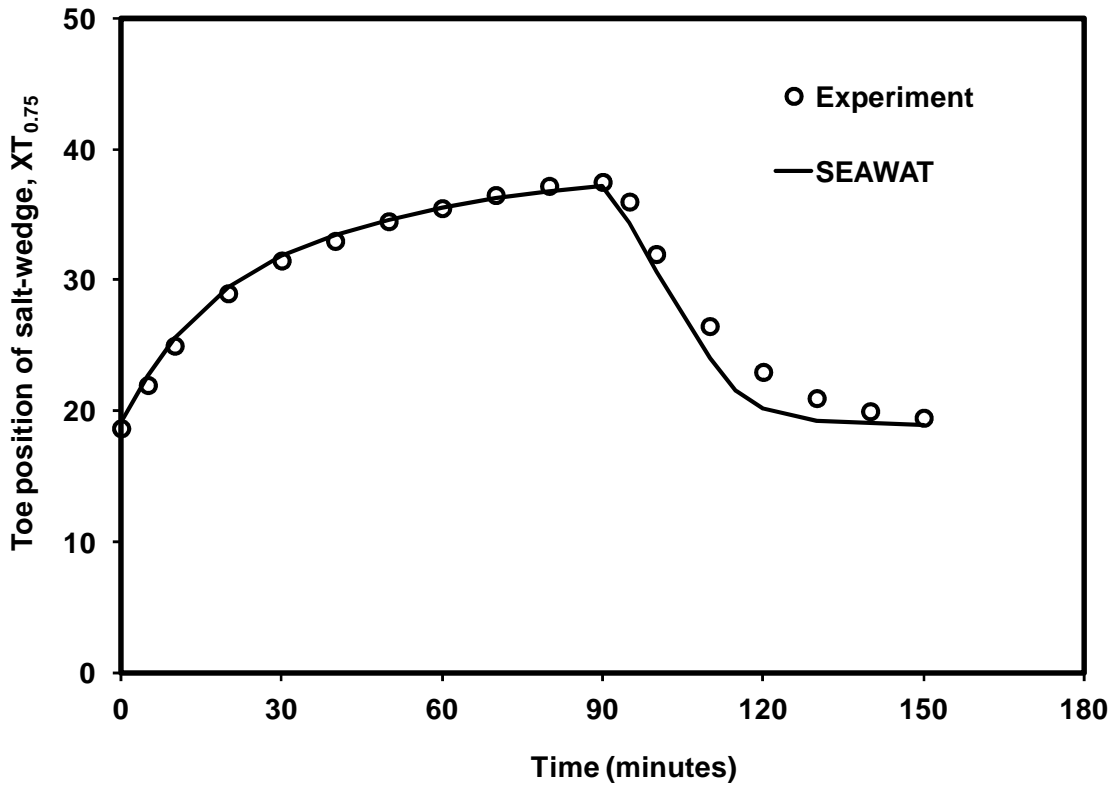
Figure 3.7. Comparison of experimental and model-simulated toe positions estimated at 0.75 cm above tank bottom in the areal-flux experiment

3.3.3 Analysis of Time Scales Associated with Intruding and Receding Salt Wedge Transport Processes

The transient data for the regional flux experiment, presented in Figure 3.4, show that the intruding wedge requires more time to reach steady-state when compared to the receding wedge. This trend is also observed in the recharge flux experiment shown in Figure 3.5. A previously published experimental dataset presented by *Goswami and Clement* [2007] for a constant head system also indicated a similar trend. This is an interesting, counter-intuitive result which implies that it will take relatively less time to remediate (or reverse) saltwater intrusion effects when compared to the time taken to contaminate (or advance the wedge into) the system. This is a subtle yet an important result that can play a significant role in managing water quality of coastal aquifers. However, so far no one has either quantified or analyzed the disparities in the time scales associated with saltwater intrusion and recession processes.

In order to quantify the difference between intruding- and receding-wedge migration rates, we first define a term $\Delta X_T(t)$, which is the distance that remains to be traversed by a migrating saltwaterwedge toe to reach its final steady-state condition (note, we will be using numerical data in this analysis and report the estimates of X_T at the bottom of the aquifer). Using this definition, for an intruding wedge $\Delta X_T(t) = ABS(X_T(t)-X_{T,for\ SS2})$ and for a receding wedge $\Delta X_T(t) = ABS(X_T(t)-X_{T\ for\ SS3})$. Note in our experiments the final steady state SS3 is identical to the initial steady state SS1. For the regional-flux test, the values of $X_{T\ for\ SS1}$ (or $X_{T\ for\ SS3}$) and $X_{T\ for\ SS2}$ were estimated using SEAWAT as 19.3 and 36.8 cm, respectively. The computed values of $\Delta X_T(t)$ for both intruding and receding wedges are presented in Figure 3.8(a).

The figure clearly shows that the receding wedge moves considerably faster than the intruding wedge as seen in Figure 3.8(a). The function $\Delta X_T(t)$ resembles a first-order decay

process, and hence one could fit an exponential decay curve of the form $\Delta X_T(t) = \Delta X_{T0} \exp(-t/\tau)$ to these data; where, the parameter ΔX_{T0} is the maximum distance traversed by a moving wedge, and τ is a characteristic time constant. It should be noted that this approximate fitting analysis was completed just to estimate a characteristic time for this transient problem. For the regional-flux test, the value of ΔX_{T0} was calculated as 17.5 cm [ABS ($X_{T \text{ of SS1}}$ - $X_{T \text{ of SS2}}$)], and the fitted values of τ for intruding and receding wedges were, 15.0 and 7.9 minutes, respectively. The time constant τ is a measure of the characteristic time associated with the underlying transport process (note, here the value of $\Delta X_T(t)$ starts from a maximum and decays with time). The value of τ computed for the intruding system is larger than the value computed for the receding system indicating that the intrusion process is inherently slower than the recession process. Based on this result one could hypothesize that it will take relatively less time for a salt wedge to recede from an aquifer when compared to the time taken for the wedge to intrude into an aquifer. To test the validity of this hypothesis at a larger scale, we completed a simulation study for a field scale problem reported in *Chang et al.* [2011]. The problem considered a two-dimensional unconfined aquifer system which is 1000 m long and 31 m thick with unit width. The sea level was set at 30 m along the left boundary. A regional flux of 0.186 m^3/day was injected at the right boundary. The initial steady-state (SS1) location of the salt wedge toe, $X_{T \text{ for SS1}}$, was 380 m away from the coastal boundary. To initiate transient intrusion conditions, the boundary flux was instantaneously reduced to 0.140 m^3/day (about 75% of the initial flux) which allowed the wedge to advance towards the landward direction. It took approximately 60,000 days for the system to reach the second steady state (SS2), and value of $X_{T \text{ for SS2}}$ was 485 m. The receding-wedge experiment was then initiated by restoring the freshwater flux back to the initial rate of 0.186 m^3/day. The wedge started to recede back and reached the third steady state (SS3) after

about 40,000 days. In Figure 3.8b, we provide the $\Delta X_T(t)$ profiles for both intruding and receding simulations. The value of ΔX_{T0} for the system is 105 m (485 m – 380 m) and the fitted values of the time constant τ for intruding and receding wedges are 13,600 and 9,400 days, respectively.

To compare the differences in intruding and receding transport times scales under areal-recharge-flux boundary conditions, we completed a new set of simulations and compiled the $\Delta X_T(t)$ data for the recharge condition. The initial amount of areal recharge used in the simulation was 0.0102 cm/sec and the corresponding value of $X_{T\ for\ SS1}$ was 19.7 cm. The flux was then reduced to 0.0071 cm/sec the corresponding value of $X_{T\ for\ SS2}$ was 37.3 cm. Note that the recharge rates were selected to match the values of X_T close to the regional flux scenario. Figure 3.9 shows the SEAWAT simulated data and the fitted exponential profiles for this problem. Similar to previous problems, the intruding wedge moved slower than the receding wedge even under areal-recharge flux conditions. The simulated data for the receding wedge however, did not show a smooth exponential trend. We evaluated the parameters of best fit exponential functions to both datasets and used it to estimate the values of the time constants for the intrusion and receding wedges as 22.7 and 10.1 mins, respectively. These results once again confirm that the transport time required for the intruding wedge is more than the time required for the receding wedge.
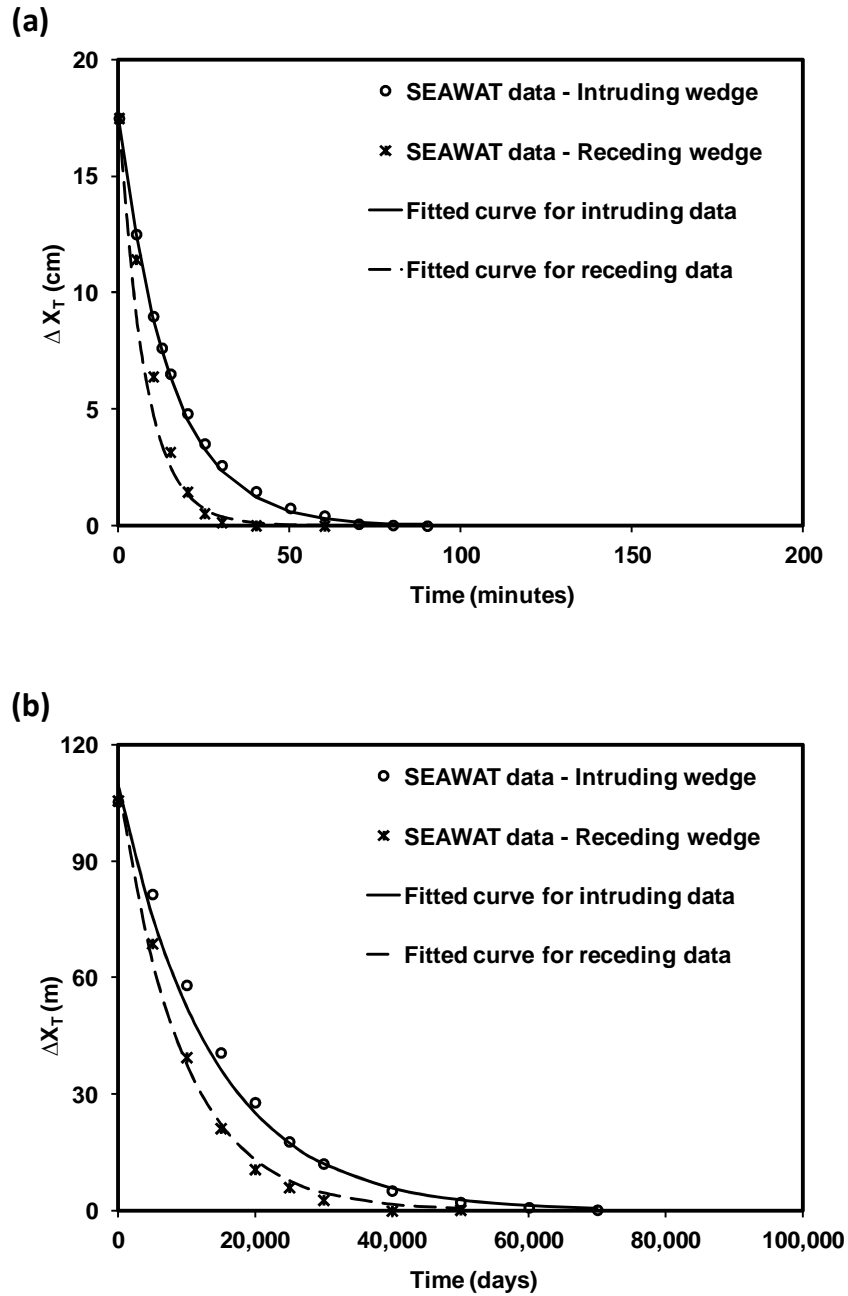
Figure 3.8. Comparison of toe migration rates for intruding and receding wedges for laboratory-scale problem of (a) regional flux experimental problem and (b) field scale problem (reported in Chang et al. 2011).
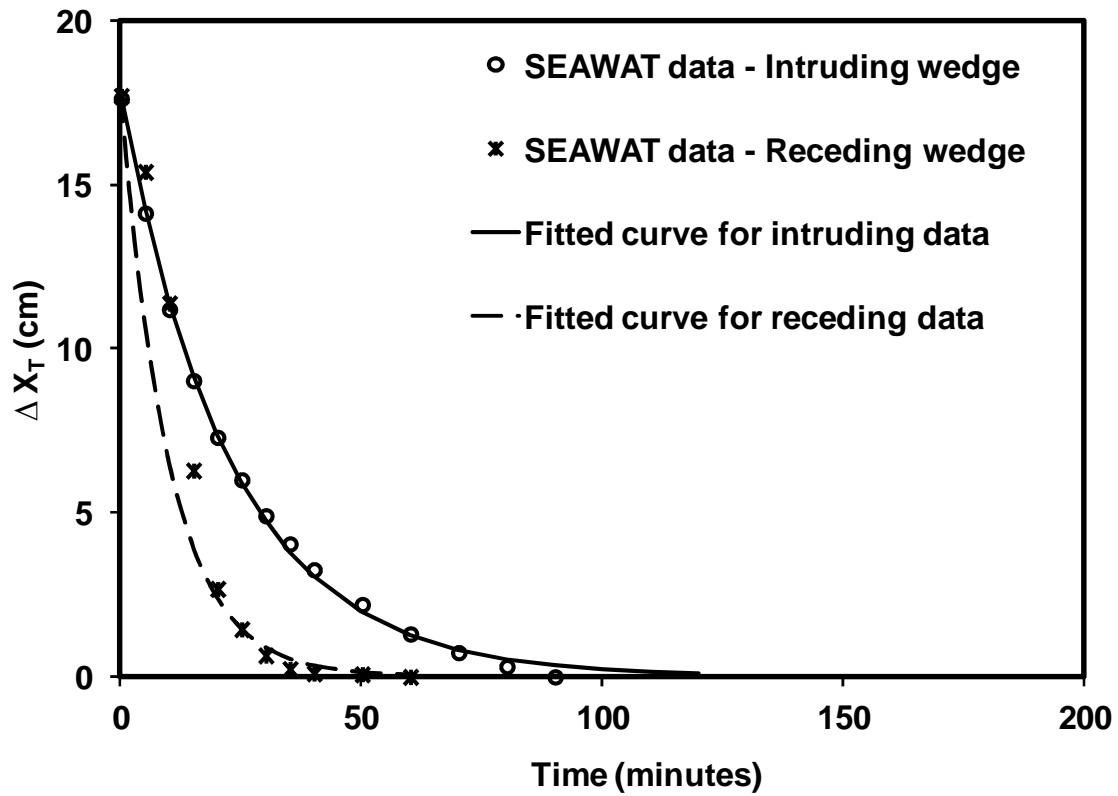
Figure 3.9. Comparison of toe migration rates for intruding and receding wedges for laboratory-scale problem of areal-recharge flux experimental problem.

In order to understand the fundamental reason for the difference in the transport time scales, we analyzed the underlying velocity distribution (or flow field) near the intruding and receding wedges. Figure 3.10 shows the model-predicted vector field for the system at the two steady state conditions SS1 and SS2 (for the regional flux system). The length of each velocity vector presented in Figure 3.10 is directly proportional to the magnitude of the velocity. The figures also show the 50% concentration contour to delineate the wedge location. Several interesting observations can be made from these steady-state data. First, the vector field shows that the velocities in the freshwater region above the wedge are much higher than the velocities in the saltwater region (velocity vectors of salt water are small and we will use log scale to better visualize these vectors in a later figure). It can be observed that the freshwater flow from the inland boundary converges into the narrow zone above the salt wedge and discharges within a high velocity region as it approaches the sea-side boundary. On the contrary, saltwater flow velocities below the wedge are small forming a relatively stagnant region. Upon closer observation one could observe a convection cell circulating saltwater beneath the wedge. Also, there is a stagnation point (with opposing flow vectors) present near the toe of the wedge at the bottom of the aquifer.

To better understand the transport dynamics under transient conditions, we plotted the velocity fields for both intruding and receding wedge after two minutes of transport (i.e., two minutes after the steady state condition was perturbed). This data is shown in Figure 3.11. In order to better visualize the low velocity patterns present beneath the salt wedge, we transformed the velocity vector field in log scale and Figure 3.12 shows the vector field computed at various times. The first picture, Figure 3.12a, simply presents the steady-state (SS1) data shown in Figure 3.10a in logarithmic scale. One could now clearly see the circulation cell and the

stagnation point (present at around 20 cm) in this log-transformed velocity vector plot. Note, under the wedge, saltwater continuously enters the aquifer from the bottom and exists slightly beneath the wedge, forming a convection cell.

Figure 3.11a and Figure 3.12b show the velocity field of the transient intruding salt wedge (2 mins of transport after SS1). The figures show that the transport process distorts the convection cell when wedge is migrating into the aquifer. All the vectors below the wedge are now pointing towards the landward direction. Within 2 minutes, the stagnation point has been pushed into the system by about 26 cm. The relative magnitude of saltwater velocity is still small (see Figure 3.11a) and the saltwater flow vectors are diametrically opposite to the freshwater flow vectors forming a stagnation region where the velocities reverse; also a distinct stagnation point continue to persist at the aquifer bottom (see Figure 3.12b). In the intruding system, the saltwater has to advance slowly against an opposing fresh water flow field. Once the steady state condition is reached (Figure 3.12c) the convection cell was restored.

Figures 3.11b and 3.12d show the velocity field of the transient receding wedge (2 mins of transport after SS2). A direct comparison of the flow fields intruding and receding flow fields presented in Figures 3.11a and 3.11b shows that the receding system is characterized by much higher velocities since the net freshwater flux transmitted through the system is higher in this case. Figure 3.12d clearly shows that once the fresh water flux was increased to initiate the receding condition, the direction of saltwater water flow is reversed towards seaward direction. This flow reversal is a transient phenomenon and was due to the sudden increase in freshwater flux and the associated changes in groundwater heads. There is no stagnation point in this system. Unlike the intruding system, which supports opposing flow fields, here the flow field is unidirectional with all the vectors pointing towards the saltwater boundary. Therefore, the

transport processes associated with a receding wedge can flush the saltwater rapidly out of the system, facilitating faster transport of the salt wedge.
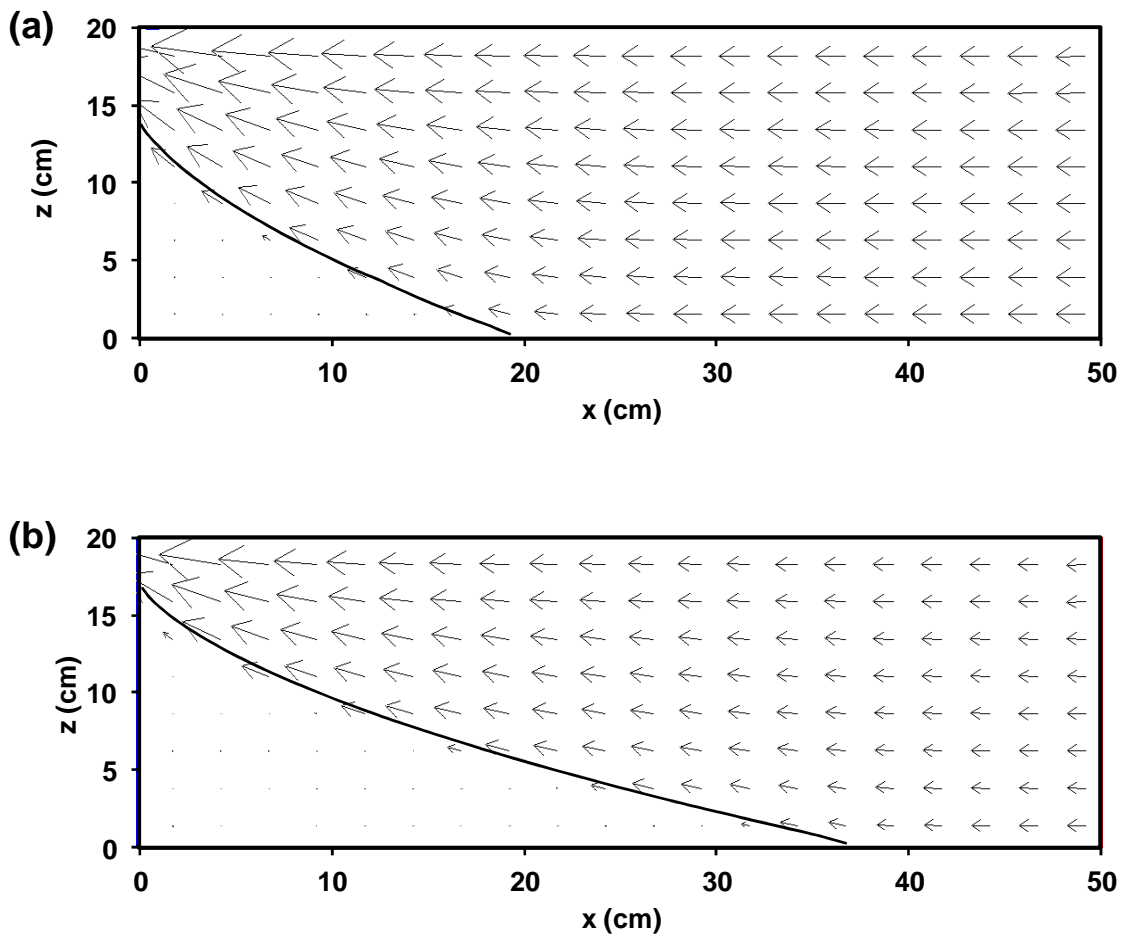
Figure 3.10. Simulated steady-state velocity fields for the regional flux experiment (a) SS1 and (b) SS2.
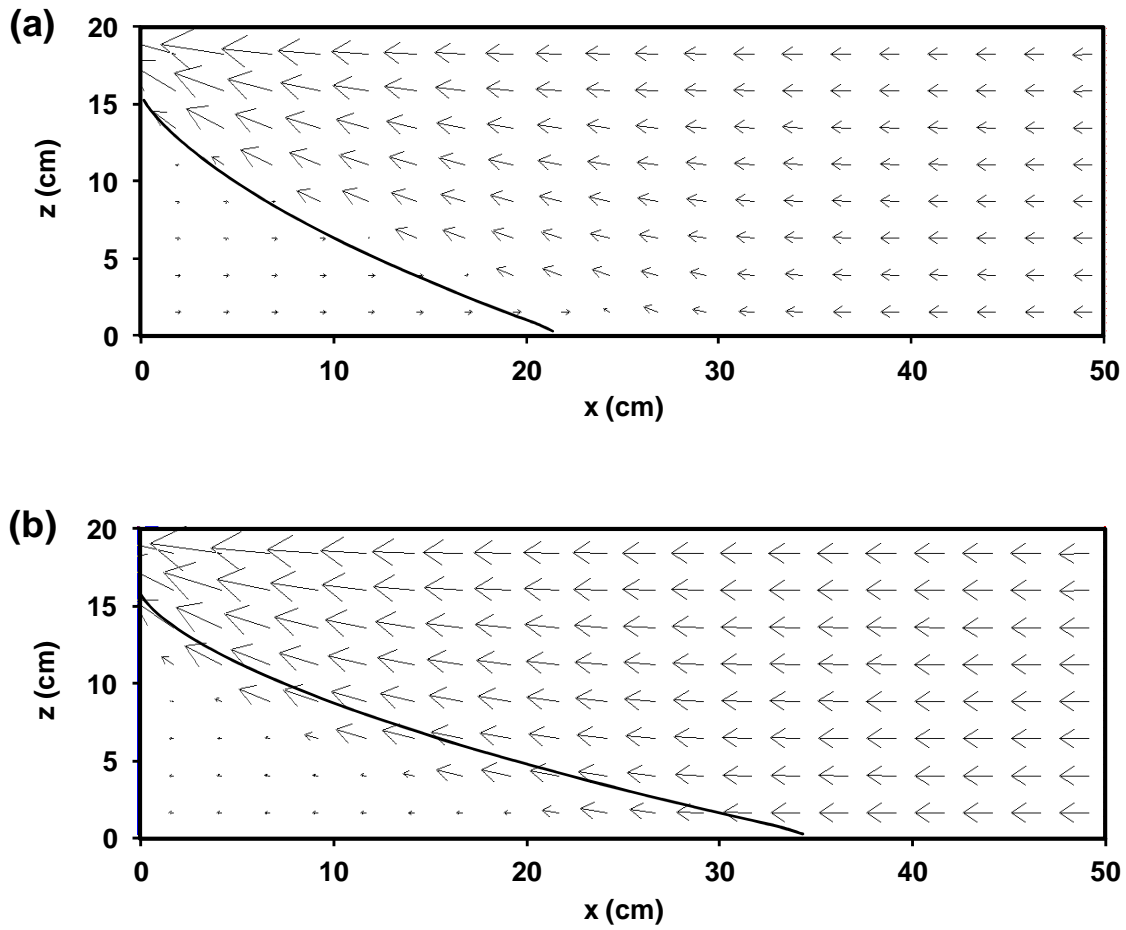
Figure 3.11. Simulated transient velocity fields for the regional flux experiment (a) 2 minutes after SS1 and (b) 2 minutes after SS2.
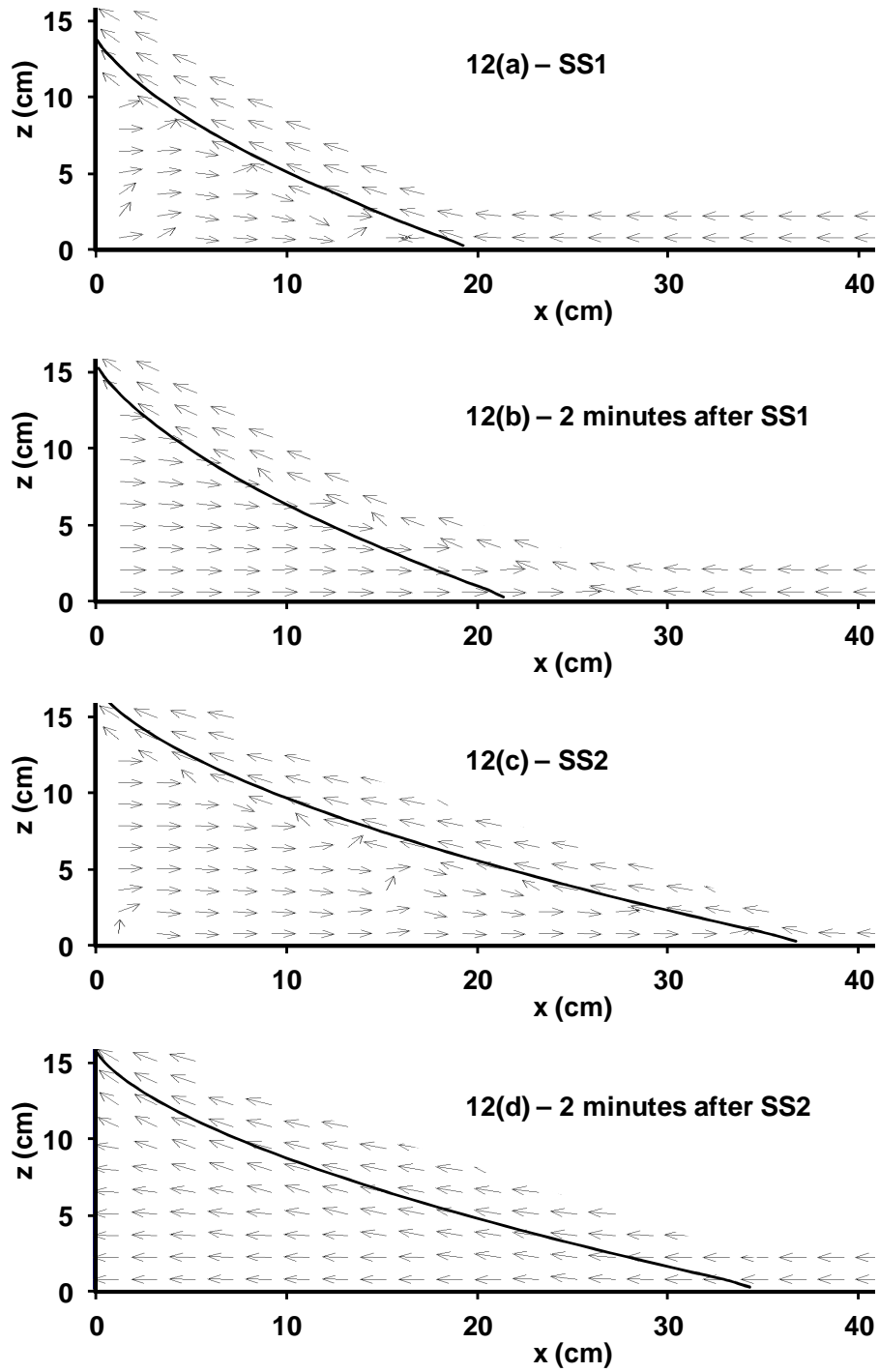
Figure 3.12. Visualization of the velocity fields near the salt wedge plotted in log scale at (a) SS1, (b) 2 minutes after SS1, (c) SS2, and (d) 2 minutes after SS2.

3.4 Conclusions

Sea-level rise and reduction of recharge due to changes in rainfall patterns and the associated changes in groundwater fluxes are the two major climate-change-induced hydrological processes that can affect saltwater intrusion processes in coastal aquifers. The objective of this research was to conduct laboratory-scale experiments to investigate the impacts of variations in regional and areal-recharge fluxes on saltwater intrusion in unconfined aquifers. We have successfully completed laboratory experiments to study two types of flux-controlled saltwater intrusion problems: one controlled by the regional flow delivered from the inland freshwater boundary, and the other controlled by the recharge flow delivered from the top boundary. The results of the experiments are used to develop a better understanding for the influence of changes in boundary fluxes on transient saltwater intrusion processes. The results were also modeled using the numerical code SEAWAT. The experimental data presented in this study are useful benchmarks for testing the validity of density-coupled flow and transport models involving flux-type boundary conditions.

Based on our experimental data we hypothesized that the time scales associated with an intruding wedge would be higher than a receding wedge. This hypothesis was confirmed using numerical simulations completed for problems involving two different scales (1-m and 1000-m scales). Our analysis also shows that the intruding system supports two opposing flow fields with a distinct stagnation point at the bottom of the aquifer, and a diffused stagnation zone along the wedge where the flow velocities reverse direction. On the other hand, receding systems support a unidirectional flow field with all the velocity vectors pointing towards the saltwater boundary. Due to the presence opposing flow fields and the stagnation zone, the time taken for saltwater to intrude into an aquifer will be relatively high when compared to the time taken for

the saltwater to recede out of an aquifer (which has a well-aligned unidirectional flow field). The insights gained from this study help us better understand the transport processes occurring within transient saltwater wedges, and these processes can be coupled to multi-species reactive transport formulations [*Clement et al.*, 1998; *Sun and Clement*, 1999] to predict the exchange of nutrients and other contaminants between terrestrial and marine waters. Overall, this study has the following two major contributions: 1) the experimental efforts report transient saltwater intrusion data for systems involving two types of flux boundary conditions; and 2) the experimental observations together with the numerical results point out the time-scale differences between intruding and receding saltwater wedges and offer a mechanistic explanation for their difference.

Chapter 4

LABORATORY AND NUMERICAL INVESTIGATION OF TRANSPORT PROCESSES

OCCURRING BENEATH A SALTWATER WEDGE

4.1 Introduction

Due to rapid urban development, shallow aquifers in coastal areas have become highly vulnerable to contaminants dissolved in urban runoff water and/or contaminants inadvertently discharged from leaking underground storage tanks or landfills that are located close to the shoreline. These contaminants not only pollute the local unconfined aquifer, but they also have the potential to contaminate the entire shoreline beach environment. This is due to the presence of a saltwater wedge, a common feature in coastal aquifers, which can influence transport pathways and force groundwater plumes to discharge along the beach face. Westbrook et al. [2005] completed a field study to document the transport of a dissolved hydrocarbon groundwater plume flowing towards a tidally and seasonally forced saline water body in Perth, Western Australia. Their field data indicate shore-focused discharge where the groundwater seepage occurred along beach-face sediments within a zone less than 10 m from the high tide mark. The plume discharge was impacted by the transient movement of the saltwater wedge. This study illustrated the need for understanding the groundwater flow dynamics in the vicinity of the wedge while predicting the exchange of contaminants between terrestrial to marine waters.

Figure 4.1 is a conceptual diagram that illustrates how contaminant discharged in coastal aquifers will be impacted by the presence of the salt wedge. The anthropogenic contaminants

discharged within the shallow freshwater zone (well above the wedge) would be transported towards the beach face. In addition, as shown in the figure, coastal groundwater systems can also circulate nutrients or other contaminants of marine origin within the saline water present beneath the wedge. The density contrast between the fresh groundwater and saline ocean water induces a circulation cell below the wedge which can enable exchange solutes between marine and terrestrial waters. Saltwater flow induced by this circulator motion is an important component of the submarine groundwater discharge (SGD) [Destouni and Prieto, 2003; Li et al., 1999; Smith, 2004]. It has been well established that chemicals entering coastal water via SGD have considerable consequence on the marine ecosystems [Johannes, 1980; Moore, 1996; Moore and Church, 1996; Robinson et al., 2007; Simmons, 1992]. Typical groundwater flow velocities within this circulatory cell would be relatively small (compared to the freshwater velocities above the wedge) and hence the transport within the wedge is expected to be dispersion dominated.
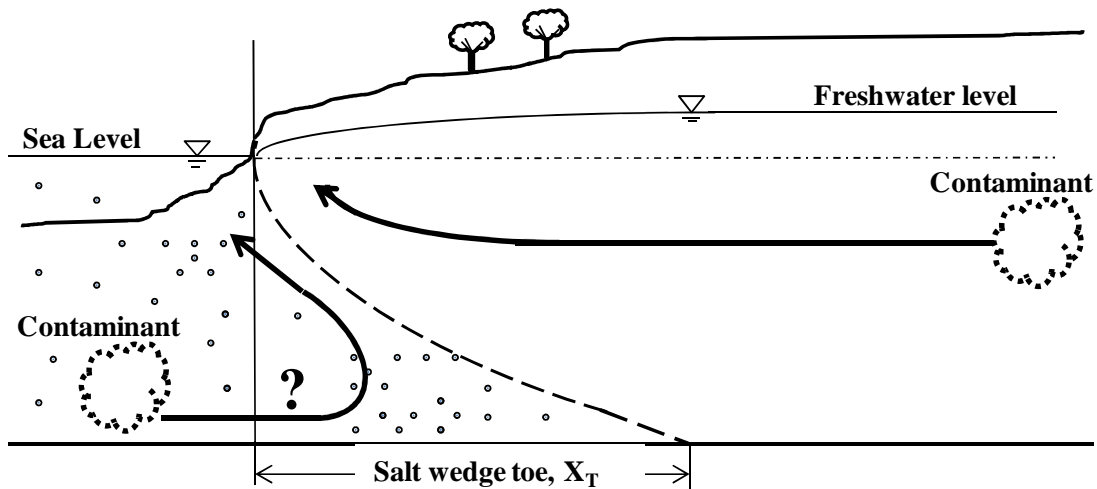
Figure 4.1. Conceptual transport model in unconfined coastal aquifer.

In the literature, only a few studies have focused on conducting physical experiments to investigate the contaminant transport processes occurring near a saltwater wedge. Zhang et al. [2002] conducted laboratory experiments to visualize contaminant transport above a wedge. They completed a set of tracer transport experiments that tracked the movement of a dense contaminant plume discharged above the salt wedge. Their observations showed that a dense contaminant plume became more diffusive compared to the less dense plumes as it approached the narrow discharge zone near the coastline. Non-dimensional parameters were developed to qualitatively characterize the plume; no attempts were made to reproduce the observations using any numerical models. Volker et al. [2002] completed a numerical modeling study to investigate the transport of a dense contaminant plume in an unconfined aquifer. Their simulation results were also compared against experimental data. The study modeled the sea-side boundary using two types of boundary conditions: a) as constant head freshwater boundary that neglected density effects, and b) as a constant head saltwater boundary that included density effects. Their results indicated that when the plume is away from the boundary, predictions based on both approaches matched reasonably well with experimental results. However, as the plume approached the coast, the experimental data indicated that the plume will be uplifted along the saltwater interface and finally exited along the shoreline. This observed uplifting and shore-focused discharge patterns were recreated only by the model that considered density effects. The model that ignored density effects predicted an incorrect travel path where the plume travelled further into the sea and exited under the seabed. The study concluded that ignoring seawater intrusion effects would not only underestimate the amount of contaminant mass exiting along the beach face, but it would also result in simulating unrealistic transport pathways.

A few laboratory studies have focused on understanding the effects of tides on controlling transport patterns in coastal aquifers near the groundwater-ocean boundary. For example, Boufadel [2000] studied the transport pathways of nutrients used for remediating beach-face contaminants resulting from the past oil spills. Laboratory experiments using two types of density gradients were completed to investigate the effects of tides and buoyancy on beach hydraulics. In both experiments, the authors observed that the groundwater flow from the aquifer moved seaward via the intertidal zone and pinched out near the low tide mark. The experimental data was modeled using a numerical simulator, which was then used to design nutrient delivery strategies for bioremediating oil contaminated beaches. Kuan et al. [2012] completed laboratory experiments to study tide-induced circulation processes that would lead to the formation of an upper saline plume within the intertidal zone. They found that the presence of the upper saline plume moved the fresh groundwater discharge zone towards the low tide mark and restricted the movement of the salt wedge. Illangasekare et al. [2006] presented a laboratory dataset that characterized the movement of dense saline plumes in a tsunami impacted aquifer. Their laboratory study first simulated the pre-tsunami initial conditions by setting up a constant regional hydraulic gradient. Their experiments used a variety of dyes to study the mixing of different types of salt waters and their interactions with regional freshwater. Initially, an uncolored fresh groundwater (identified as ''freshwater'') plume was allowed to flow from right to left toward the dense seawater boundary, which was marked green. The green seawater was allowed to intrude the aquifer from the left to form a steady-state saltwater wedge. The inundation caused by the tsunami wave was then simulated by evenly discharging a fixed amount of red-colored saltwater, identified as ''tsunami'' water. In addition, a blob of red-colored tsunami water was also injected directly into the aquifer to mimic saltwater flow via open wells.

69

Qualitative observations were made to understand the fate and transport of different saltwater plumes. The study used non-dimensional analysis to characterize the transport times, however no quantitative numerical assessments were made. Use of different types of colored waters allowed researchers to visualize various types of mixing effects; in the current effort, we employ a similar approach to study contaminant plume migration processes occurring near a saltwater interface.

Above studies have demonstrated the importance of understanding the role of a salt wedge when predicting the movement of a contaminant plume in coastal aquifers. While several experimental efforts have focused on studying contaminant transport above a wedge, as per our knowledge, so far no one has studied the fate and transport of contaminants beneath a saltwater wedge. Kohout [1960] was the first to complete a field study in Florida and estimated that the saltwater flux circulated through the system is about 10% of the fresh groundwater flux flowing towards the sea. Destouni and Prieto [2003] completed a modeling study to develop empirical correlations between groundwater fluxes present above and below a saltwater wedge. Their correlations also show that the saltwater flux is roughly an order of magnitude smaller than the freshwater flux. Smith [2004] completed a comprehensive modeling study and concluded that the amount of saltwater flux circulated within the system can vary widely and would depend on the level of dispersion in the system. However, most of these studies are based on theoretical modeling data and so far no one has provided experimental data to quantify the circulating saltwater flux and the associated transport processes.

The objective of this effort is to conduct well-controlled contaminant transport experiments to study the dynamics of groundwater flow transport patterns beneath a saltwater wedge and relate the transport to the flow patterns present above the wedge. We used a novel

70

experimental approach that employed a variety of dyed waters to map and compare the mixing and transport patterns occurring above and below a saltwater wedge. The experiments were simulated using a numerical model. The model was then used to investigate these transport problems in a larger scale problem.

4.2 Methods

4.2.1 Experimental Method

Figure 4.2 shows the experimental setup used in this study. The dimension of the flow tank was 50.5 cm × 28 cm × 2.2 cm. The origin of the Cartesian coordination system used to record experimental observations was set at the left bottom corner of the tank. The tank was fitted with three distinct flow chambers. The right inlet chamber was used to supply freshwater flow delivered using a peristaltic pump. The sea level was set to 25.1 cm by adjusting the saltwater head at the left outlet chamber. The central porous media chamber was filled with silica glass beads of diameter 1.1 mm. The beads were packed under saturated conditions to prevent the trapping of air bubbles inside the tank. Thin stainless-steel meshes were used to separate the side chambers (boundary conditions) from the porous media chamber. Freshwater level at the right boundary was set at 26.03 cm. The hydraulic conductivity (K) of the tank was measured using the in-situ method described in Simpson et al. [2003]. The average value of conductivity was 1.03 cm/s. The measured values of saltwater and freshwater densities were 1.025 g/cm3 and 1.000 g/cm^3, respectively. All the experimental parameters used in this study are summarized in Table 1. The transport experiments were recorded using a video camera (Panasonic HDC-HS250). Other experimental procedures used were similar to the ones reported in our previous studies [*Abarca and Clement*, 2009; *Goswami and Clement*, 2007; *Goswami et al.*, 2009]. However, in this study, as shown in Figure 4.2, the flow tank was slightly modified to accommodate a long needle and a short needle of lengths 300 mm and 50 mm, respectively, and thickness of 1.6 mm. These needles were buried in the tank to allow tracer injection above and below the wedge. Both needles were set in the tank when the porous medium was wet packed. In addition to this physical modification, in this study we employed a multi-colored tracer

72

scheme to map various transport processes. The scheme used three different types of waters to discern the colored freshwater (dyed red) and dense tracer water (dyed green) colorless the seawater (colorless). Note that in all our previous experiments, the saltwater wedge was colored red. In this effort, we reversed the coloring scheme and created a colorless salt wedge, which allowed us to better visualize the tracer transport patterns occurring under the wedge. The freshwater was marked using 1 ml of red food color for every liter of water. The dense tracer solution was prepared by mixing 1 ml of green dye for every 250 ml of saltwater.

4.2.2 Details of Tracer Transport Experiments

Three types of tracer solutions with density values of 1.000, 1.0125 and 1.025 g/cm^3 were prepared to conduct three different transport experiments (identified as Test-1, Test-2 and Test-3). Test-1 and Test-2 are baseline reference transport experiments that involved injection of 22 ml of tracer slug with density values of 1.000 (neutral tracer) and 1.0125 (dense tracer), respectively, above the saltwater wedge very close to the freshwater boundary (see Figure 4.2 for details). The volume of the tracer slug was 22 ml which was injected in about 8 seconds, yielding an injection rate of 2.75 ml/s. The x-z coordinates of the injection point are: $x = 45$ cm and $z = 22.5$ cm. The tracer slugs were allowed to transport with the freshwater flow and the images were recorded at different times until the plume reached the exit boundary. The result of Test-1 was used to calibrate a numerical model by adjusting the dispersivity values, and Test-2 data was used to test the model performance.

Test-3 was the most important tracer study that recorded the transport patterns occurring beneath the wedge. The coordinates of the injection point are: $x = 4.0$ cm and $z = 0.5$ cm. About 11 ml of saltwater solution with a density value of 1.025 g/cm^3 (which is identical to the

seawater in the left tank) was injected beneath the wedge. The injection time was 40 s, yielding an average injection rate of 0.275 ml/s. Note since the ambient density of water present beneath the wedge was 1.025 g/cm^3, and hence the tracer slug acted like a neutral tracer within the salt wedge.

4.2.3 Numerical Modeling Method

The MODFLOW-family variable density flow code SEAWAT [*Guo and Langevin*, 2002] was used to model the experimental data. A uniform two-dimensional grid of dimension 0.5 cm (102 cells in the x-direction and 50 cells in the z-direction) was used to discretize the flow tank. Thickness of numerical cells was set to 2.2 cm, which is identical to the thickness of the tank. The saltwater head at the left boundary was set to 25.1 cm for the entire simulation. Freshwater was allowed flow from the constant-head boundary set in the right hand side tank. The value of specific storage (S_s) was set to 10^{-6} cm^{-1}. Similar to the Goswami and Clement [2007] study, we used the confined flow approximation to simulate this steady-state experiment. All fifty model layers (of thickness 0.5 cm) were set as confined layers, and the boundary heads (i.e., the water levels at both saltwater and freshwater boundaries) always remained slightly above the top layer. The bottom of the model was set to a no-flow boundary condition. The values of longitudinal (α_L) and transversal (α_T) dispersivity were initially selected based on the values suggested by Abarca and Clement [2009], and were adjusted to fit the neutral tracer transport (Test-1) data and were later verified using dense tracer transport (Test-2) data. The total variance diminishing (TVD) scheme solver was selected for simulating all the lab experiments. A Courant number stability constraint of $Cr \leq 0.5$ was used in all the simulations.

Table 4.1: Model parameters used for simulating the lab problem

Parameter	Symbol	Value
Horizontal length	L	50.5 cm
Saltwater elevation	H_s	25.1 cm
Saltwater elevation	H_f	26.03 cm
Hydraulic conductivity	K	1.03 cm/s
Specific storage,	S_s	1×10^{-6} cm^{-1}
Longitudinal dispersivity	α_L	0.05 cm
Transverse dispersivity	α_T	0.005 cm
Saltwater concentration	Cs	0.035 g/cm^3
Saltwater density	ρ_s	1.025 g/cm^3
Freshwater density	ρ_f	1.000 g/cm^3
Density slope	E	0.714
Porosity	n	0.385

Table 4.2: Model parameters used for simulating the field problem (modified from Chang et al. 2011)

Parameter	Symbol	Value
Horizontal aquifer length	L	1000 m
Vertical aquifer thickness	B	30 m
Inland groundwater flow rates	Q_1 (low flux)	0.105 m^3/day
	Q_2 (High flux)	0.210 m^3/day
Hydraulic conductivity	K	10 m/day
Specific storage,	S_s	1×10^{-5} m^{-1}
Longitudinal dispersivity	α_L	0.4 m
Transverse dispersivity	α_T	0.04 m
Saltwater concentration	C_s	35 kg/m^3
Saltwater density	ρ_s	1,025 kg/m^3
Freshwater density	ρ_f	1,000 kg/m^3
Density Slope	E	0.714
Porosity	n	0.35
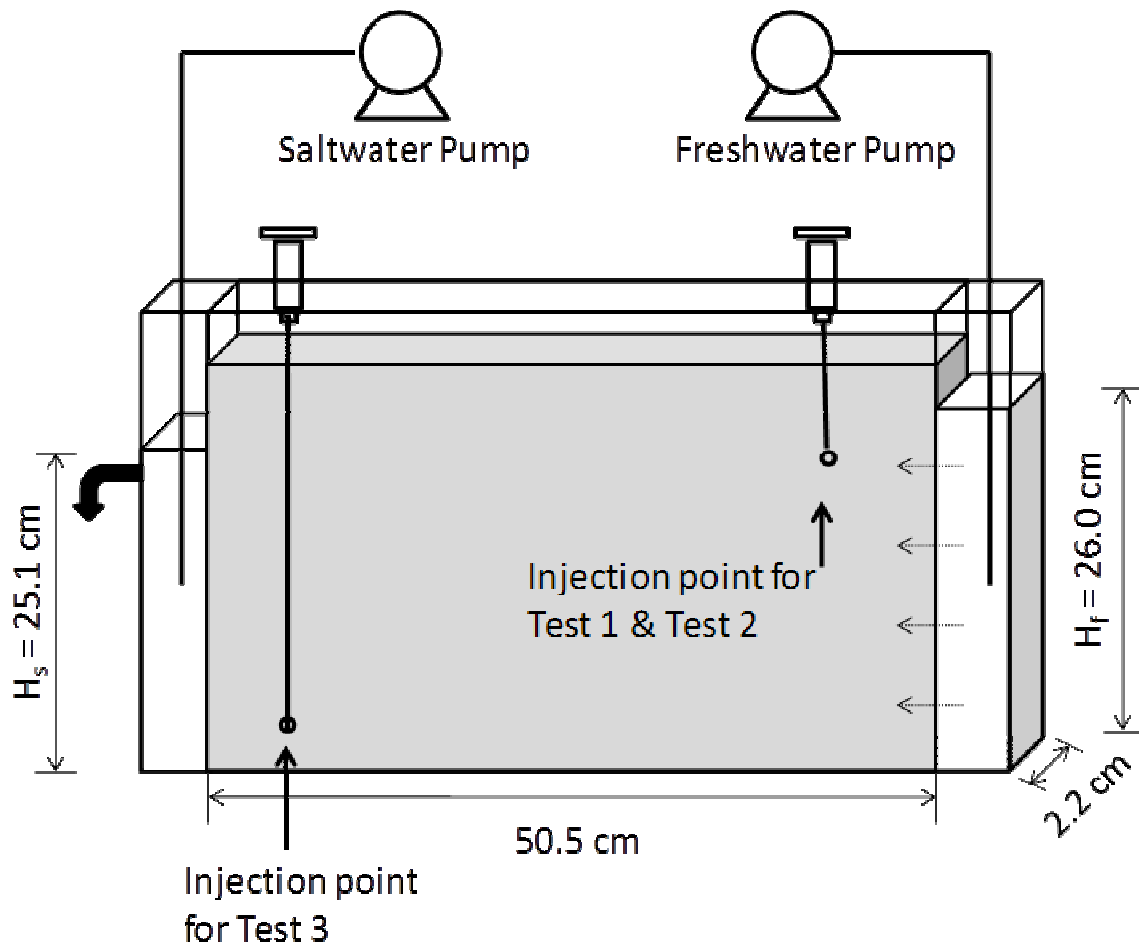
Figure 4.2. Schematic diagram of the flow tank equipped with solute injection syringes.

4.3 Results

4.3.1 Transport of Tracer Slugs Injected above the Wedge

Figure 4.3 shows time series of pictures of the neutral tracer slug as it travelled from the injection point, located near the freshwater boundary, to the saltwater boundary. The photographs were taken at 0, 5, 10 and 15 minutes after injecting the slug. The experimental data indicated that the plume required about 20 minutes for traversing the entire flow domain. The figure also shows the model simulated plume at different times. In the figure, the salt wedge is identified by white solid line which represents the 50% isochlor. The color filled plumes were generated by the contouring software that used the following color coding scheme: red > 0.8 %; yellow 0.8–0.7 %; green 0.7–0.3 %; turquoise 0.3–0.05 %; and blue < 0.05 %. As a part of this simulation study, the dispersion parameters α_L and α_T were adjusted within an expected range to reproduce the observed plume spreading levels. Based on qualitative comparison, dispersivity values of $\alpha_L = 0.05$ cm and $\alpha_T = 0.005$ cm were able to recreate the observed plume spreading patterns. These values are within the range of values reported in a previous study [*Abarca and Clement*, 2009] that used a similar type of flow tank. All the model parameters used for simulating this baseline experiment are summarized in Table 1. Both lab and model-simulated results (see Figure 4.3) indicate that the shape and spatial extent of the plume lifted upward as it approached towards the discharge boundary. Overall, the model simulated tracer transport patterns agreed well with the experimental data.

The second tracer experiment was completed to primarily assemble a dataset to test the performance of the model. In addition, the second tracer test also explored how a dense plume would behave as it sunk and interacted with the wedge. All the model parameters including the dispersion coefficients used were identical to the values used for simulating the Test-1 dataset.

Figure 4.4 shows the experimental data for the dense tracer plume as it travelled from the injection point to the saltwater boundary. The photographs were taken at 0, 5, 10 and 15 minutes after slug injection. The dense plume also took about 20 minutes to traverse the flow tank. The figure shows that the model-simulated plumes at different times

It is interesting to note that the dense plume initially started to sink and the sinking process continued for about 10 minutes; during this time, the core of the plume sank by about 10 cm in the vertical direction. The model was able to reproduce this sinking pattern. As the dense plume approached the salt wedge, the flow direction started to change and the tracer plume started to rise upwards due to the presence of saltwater wedge that almost acted as a flow barrier. Since the freshwater flow regime was characterized by strong advection the dense plume remained stable throughout the experiment. Kanel et al. [2008] studied the transport of a dense plume of nano-particles under strong advection-dominated flow conditions, and their data also showed such a stable dense plume transport pattern. Goswami et al. [2012] recently published a comprehensive study to investigate the dynamics of sinking and buoyant plumes and demonstrated the role of advection in inhibiting plume instabilities.
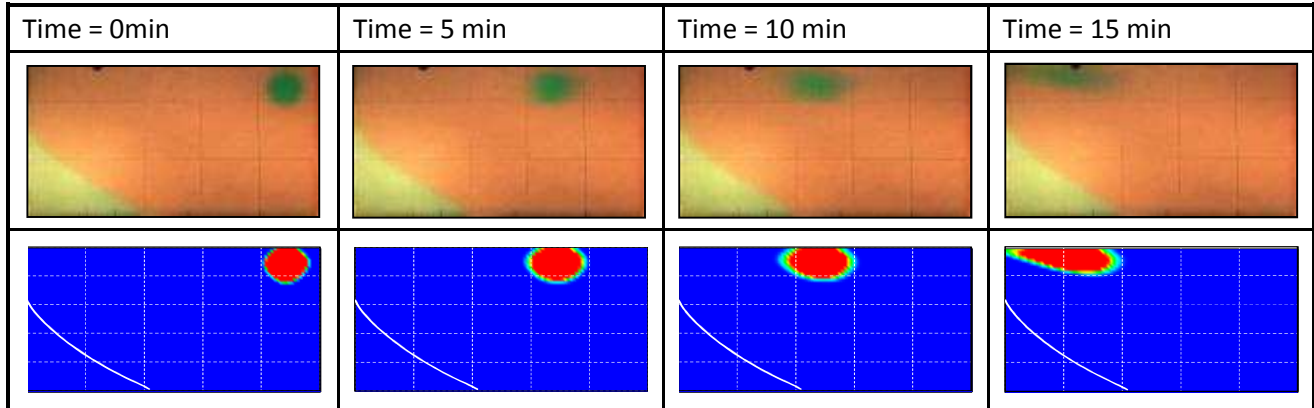
Fig.4.3. Comparison of observed data with numerical predictions for the neutral plume transport experiment (Top figure: lab data; Bottom figure: SEAWAT predictions with color filled contour -- red > 20 %; yellow 20-14 %; green 14-8 %; and turquoise 8-1 %; also, white line is the 50% saltwater contour of the wedge)
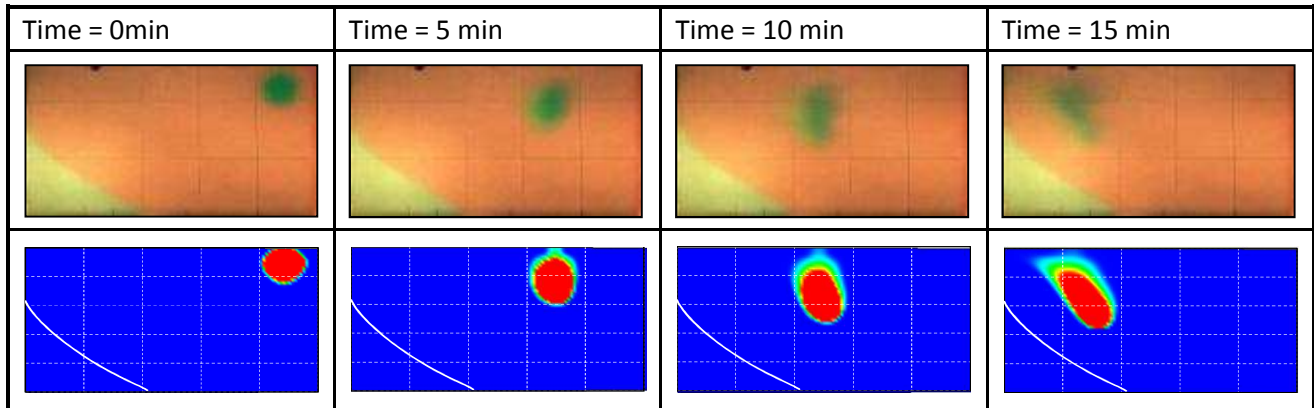
Fig. 4.4. Comparison of observed data with numerical predictions for the dense plume transport experiment (Top figure: lab data; Bottom figure: SEAWAT predictions with color filled contour -- red > 20 %; yellow 20-14 %; green 14-8 %; and turquoise 8-1 %; also, white line is the 50% saltwater contour of the wedge)

4.3.2 Characterizing Tracer Transport Patterns beneath a Saltwater

The above two tests allowed us to estimate the transport parameters for the experimental system, and also allowed to visualize the transport patterns occurring within the freshwater zone, which served as baseline information. Test-3 was the most important experiment that directly mapped the transport patterns occurring beneath the wedge. Our preliminary experiments indicated that transport under the wedge would have very little advection, and hence even a small fraction of density difference between the ambient water and the tracer slug would lead to buoyancy effects. Therefore, we carefully matched the density of the green-dyed dense tracer solution as identical to the ambient saltwater solution. Figure 4.5 shows the migration patterns of this neutral (neural since the tracer density was matched to the ambient saltwater density) plume release beneath the saltwater wedge. The digital pictures were taken at 0, 60, 120 and 180 minutes after injecting the tracer slug. The figure also shows the model predicted results, which are in good agreement with observed data. Unlike the transport in the freshwater domain, the transport beneath the wedge was extremely slow. The tracer slug was circular in shape at the time of injection; however, the circular slug started to degenerate rapidly and the evolved into an elongated plume of irregular geometry within a relatively short period. The bulk of the plume mass remained at the bottom of the tank with a "finger like" structure evolving upward; the fingers rapidly extended and were flushed out of the system by the strong advective flow active near the interface. Due to dilution of the plume mass, it was difficult to delineate a distinct plume in the digital photographs taken after about 4 hours of transport; however, some residual mass was still visible in the tank. It took approximately 6 hours (estimated based on visual

observation of the remnant green residues in the tank) for the tracer slug to flush out of the saltwater region.

Several interesting observations can be made from this laboratory dataset. First, the plume residence time within the saltwater region was about 6 hours, which is much higher than the 20 minute residence time estimated for the freshwater region. The numerical model also required about 6 hours to fully flush the tracer slug out of the system. Second, the plume was not tracking the idealized circular flow path commonly depicted in textbooks [*Fetter*, 2001; *Goswami et al.*, 2009]. Due to dispersion effects, the plume attained an elongated shape as it approached the interface. Once the plume reached the interface, a diffused fraction of the plume transported rather rapidly along the mixing zone and discharged out as a narrow finger. The model was able to reproduce these complex transport patterns well.

To test the scalability of the observed transport patterns, we completed numerical simulations for a field scale problem, which based on a modified version a problem discussed in Chang et al. [2011]. The problem considered a two-dimensional confined aquifer which is 1000 m long, 30 m deep and 1 m wide. Dispersivity coefficients are set to: $\alpha_L = 0.4$ m and $\alpha_T = 0.04$ m. Porosity was assumed to be 0.35. The sea level was fixed at 30 m along the left side of the model boundary. A constant amount of regional freshwater flow was allowed to flow from the inland boundary, and areal-recharge was set to zero. Numerical simulations were completed for two conditions that modeled low and high regional groundwater flow scenarios which used the flow rates of 0.105 m^3/day and 0.210 m^3/day, respectively. These relatively low levels of fluxes were selected to allow simulation of relatively long salt wedges. In order to study the tracer transport patterns, two tracer slugs (one above the wedge and one beneath the wedge) were released simultaneously by setting the initial condition of four model grid cells (total grid volume

82

of 64 m^3) to 100 kg/m^3. To be consistent with Chang et al. (2011) study, we used the fully implicit method option available in SEAWAT for all our field scale simulations. Other model parameters used were identical to the ones used in Chang et al. [2011] study (details are summarized in Table 4.2). Steady-state location of the salt wedge toe for the high flow rate problem was found to be around 390 m away from the coastal boundary and for the low flow rate problem it was around 730 m away from the boundary. Figure 4.6 summarizes the tracer transport scenarios predicted under both high and low flow conditions. In the figure, the salt wedge is identified by a black solid line which represents the 50% isochlor. The color filled plumes were generated by the contouring software that used the following color coding scheme: red > 0.8 kg/m^3; yellow 0.8–0.7 kg/m^3; green 0.7–0.3 kg/m^3; turquoise 0.3–0.05 kg/m^3; and blue < 0.05 kg/m^3. The figures show the observed plume patterns after 360, 20,000, 40,000, and 60,000 days of transport. The data show that after 40,000 days of transport, the center of the freshwater slug that was released above the wedge travelled about 400 meters and 800 meters under low and high flux conditions, respectively. Based on these transport times the average pore-scale transport velocity calculated for these systems are 1 and 2 cm/day, respectively, which agrees with the expected values. The presence of the salt wedge lifted the freshwater plumes, and at later times, due to converging flow conditions, the center mass moved slightly faster than the average freshwater velocity. During the same transport period (of 40,000 days), the saltwater slug, which was released beneath the wedge, travelled only about 170 m and 220 m under low and high flux conditions, respectively. Once the saltwater plume reached the plume wedge, it fingered along the wedge and flushed out rapidly from the system. The overall transport patterns predicted by the field scale model were quite similar to those observed in our experimental tank. Due to dispersion effects, the circular transport pathway could not be established within the

system; once the slug reached the wedge the bulk of the contaminant mass transported rather rapidly along the wedge. The flow budget analysis indicated that the amount of saltwater flow circulated within the low and high flux systems were 0.069 and 0.096 m³/day, respectively. These fluxes primarily control the transport processes occurring beneath the wedge. Therefore, we completed further simulation studies to quantify the sensitivity these fluxes to changes in model parameters (dispersivity values) and boundary forcings.

Time = 0 min	Time = 60 min	Time = 120 min	Time = 180 min
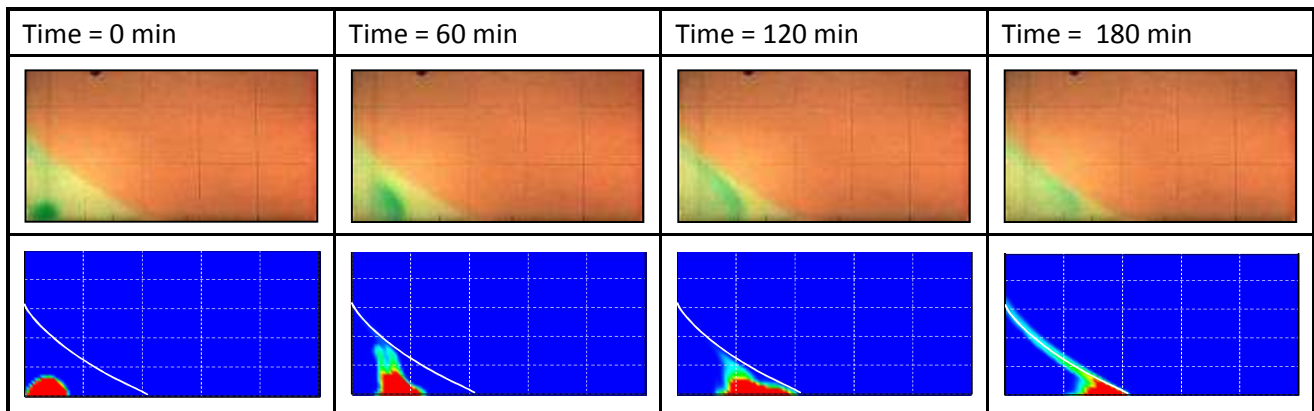
Fig.4.5. Comparison of observed data with numerical predictions for the transport experiment completed beneath the wedge (Top figure: lab data; Bottom figure: SEAWAT predictions with color filled contour -- red > 20 %; yellow 20-14 %; green 14-8 %; and turquoise 8-1 %; also, white line is the 50% saltwater contour of the wedge)
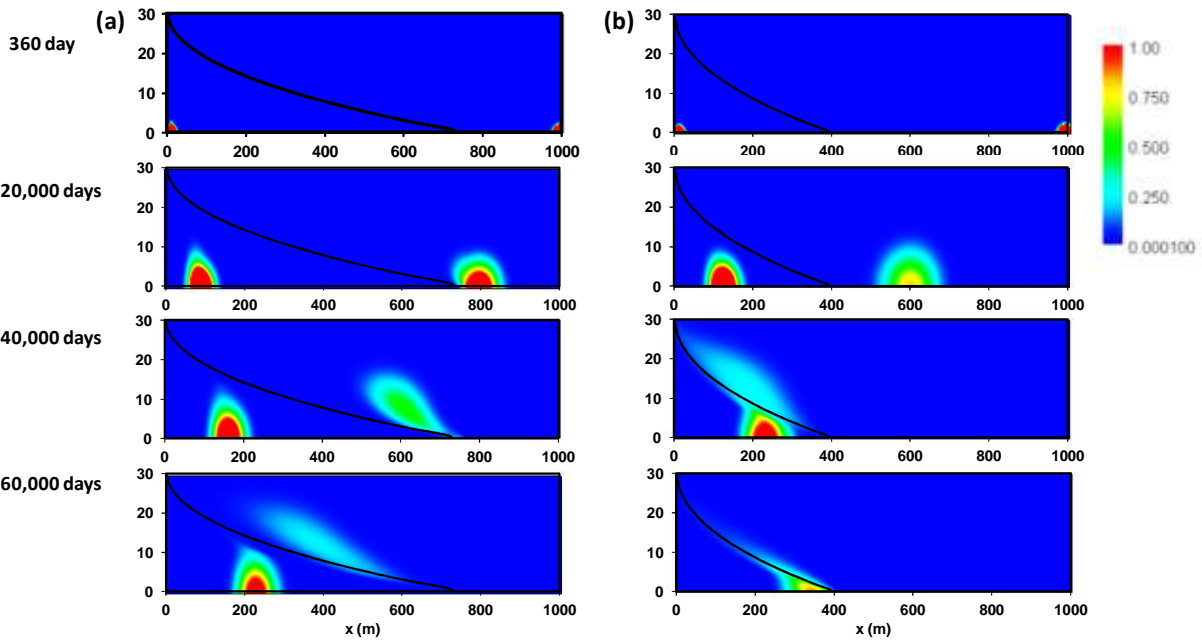
Fig. 4.6. Model simulated results illustrating the transport processes occurring above and below the saltwater wedge for the field-scale test problem: (a) simulations for low regional flow of 0.105 m^3/day and (b) simulations for high regional flow of 0.210 m^3/day. Initial contaminant concentration at the sources was 100 kg/m^3.

4.3. 3 Sensitivity of Recirculating Saltwater Flux to Dispersion and the Type of Boundary Condition

Smith [2004] pointed out that the saltwater flux circulated within the system under steady state conditions is strong function of the level of mixing (value of dispersivity) in the system. Therefore, we first completed numerical experiments to characterize impacts of dispersion on our field-scale problem at different boundary flux values. Simulations were completed by varying the regional flux from 0.15 to 1.8 m^3/day; the model was run for a sufficiently long period until steady state conditions were reached. Two sets of simulations were completed using longitudinal dispersivity values of 0.4 m and 4 m; the ratio of the transverse to longitudinal dispersivity value was set to 0.1. Furthermore, additional simulations were also completed using identical model parameters and freshwater flux values, but the freshwater deliver point was modified; instead of injecting the flow from the right regional boundary, we distributed the same amount of flow from the top of the model to simulate a system involving areal recharge flux boundary condition. The regional flux was set to zero in these simulations. Chang and Clement [2012b] completed laboratory experiments to compare saltwater intrusion problems involving regional and areal recharge boundary conditions. Their data indicate that while the extent of saltwater intrusion is highly sensitive to the magnitude of the freshwater flux, the extent is almost insensitive to the type of boundary (recharge or areal) condition. Their results also revealed that the wedge in the regional-flux experiment was thick and almost linear, whereas the wedge in the areal-flux experiment was relatively thin and shaped like an exponential decay curve. However, the impact of these differences on saltwater recirculation patterns was not investigated in Chang and Clement [2012b] study.

Figure 4.7 summarizes the results of this sensitivity study. Firstly, as expected, the amount of saltwater flux entering system was proportional to the amount of freshwater flux entering the system. Furthermore, when the dispersivity value was increased, the amount of saltwater flux circulated within the system also increased. This is because, higher dispersion resulted in more mixing which facilitated saltwater flushing; this resulted in driving a cyclic process that allowed more saltwater to enter the system. Interestingly, the relationship between saltwater and freshwater fluxes was not sensitive to the type of boundary condition used for modeling the inlet boundary; i.e., the location where the freshwater flux is allowed to enter the system. The results show that both regional and area flux boundary conditions resulted in inducing almost identical amount of saltwater flux. We completed an analytical analysis to generalize some of these results using the non-dimensional parameters proposed by Smith [2004]. In order to normalize the relationship between freshwater inflow Q_f and saltwater inflow Q_s, we used a modified version of a dimensionless freshwater flux parameter proposed by Smith (2004), which is defined as:

$$V^* = \frac{\beta KBW}{Q_f} \tag{1}$$

Where β is the fluid density ratio, $K \, [LT^{-1}]$ is the hydraulic conductivity, $B \, [L]$ is the saturated aquifer depth, $Q_f \, [L^3T^{-1}]$ is the rate of freshwater inflow, and W is the aquifer width of the aquifer $[L]$. The amount of saltwater circulated within the system was quantified using the following dimensionless parameter (defined as the percent saltwater circulation (PSC) in Smith [2004] study):

$$PSC = Q_s/Q_f \tag{2}$$

87

Where Q_s [L^3T^{-1}] is the rate of saltwater flow into the system. As pointed out by Smith (2004), the parameter V^* is the ratio of free convection velocity to forced convection in the system. Also, V^* is simply the inverse of the non-dimensional parameter "a" commonly used in Henry problems [*Henry*, 1964; *Simpson and Clement*, 2004]. The derivation for Henry problem's parameters are shown in Appendix 6. Figure 4.8 presents the data reported in Figure 7 in a non-dimensionless form. Visualizing the data in this non-dimensional format allowed us to compare the data for the current problem with other literature-derived data (which are shown marked using various symbols in Figure 4.8). The figure shows that the percentage of saltwater circulated within the system scales well with the non-dimensional freshwater flux parameter V*. Furthermore, the values V* and PSC predicted for the current problem are within the range of values observe in other published problems of different scales. Similar to Smith (2004) study, the relationship between PSC and V* shows a non-linear trend, and it is a strong function of the mixing level (or value of dispersivity). The figure shows that the non-dimensional format proposed by Smith [2004] provides a robust framework for correlating the relationship between freshwater and saltwater fluxes for a variety of problems of different scales.
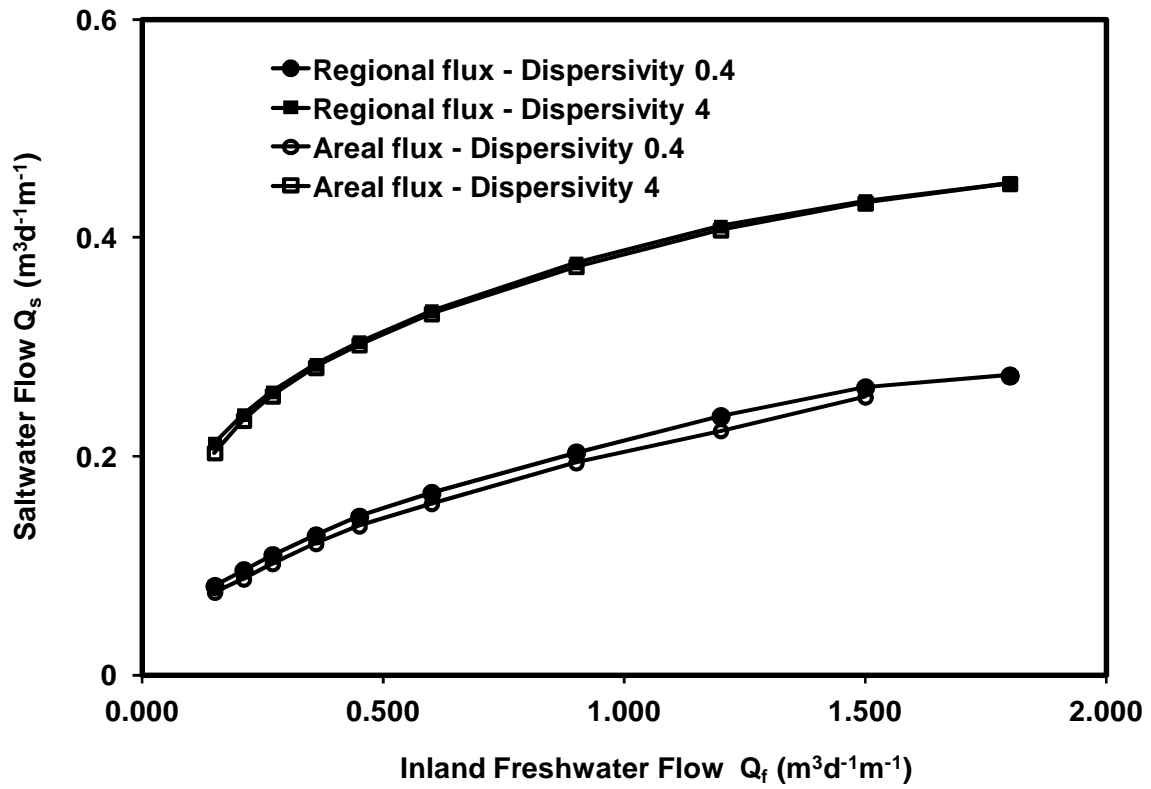
Fig.4.7. Relationship between freshwater flow and recirculate-saltwater flow for regional and areal recharge problems with different dispersivity values
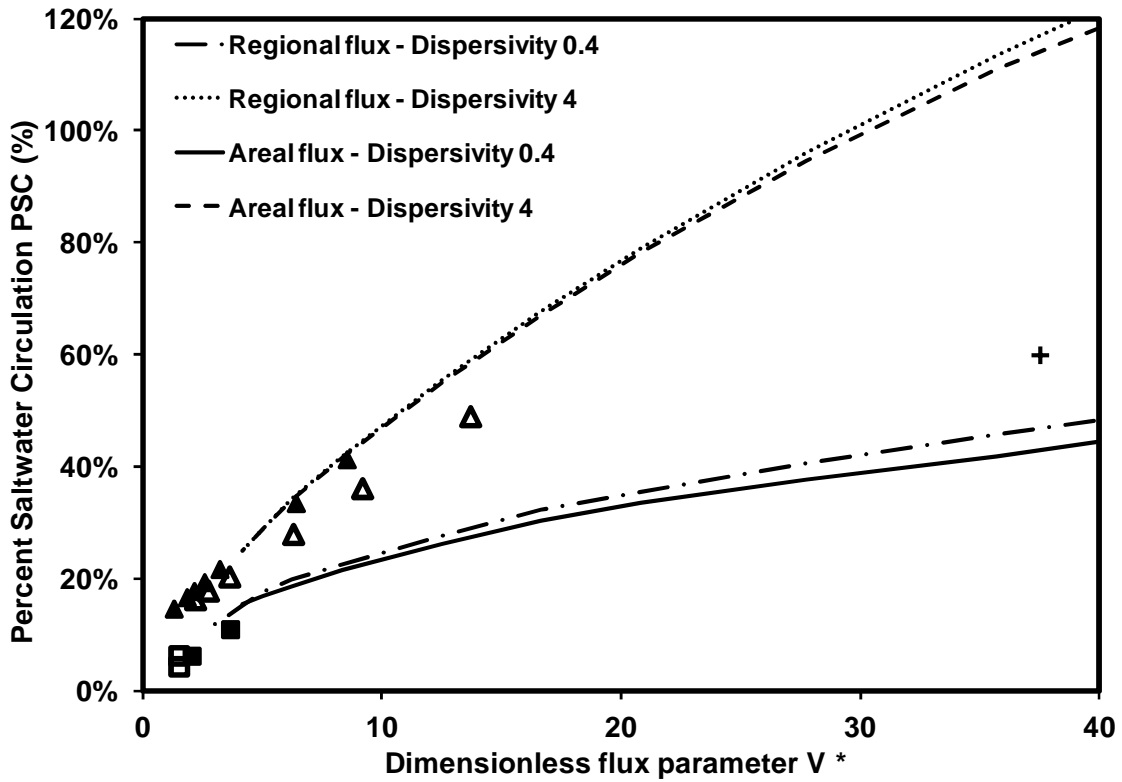
Fig. 4.8 Non-dimensional analysis of the relationship between freshwater and saltwater fluxes [The symbols indicate the following literature data points: + from Chang et al. (2011) study, ■ regional flux experimental data from Chang and Clement (2012), □ areal flux experiment data from Chang and Clement (2012), ▲ Cyprus case study from Destouni and Prieto (2003), △ Israel case study from Destouni and Prieto (2003)]

4.4 Conclusions

In this effort we have completed both laboratory and numerical experiments to study the contaminant transport patterns occurring beneath a saltwater wedge. For comparison purposes, we have also completed transport experiments to map contaminant transport patterns occurring above the wedge. Results indicate that the time scales associated with the transport processes occurring below the wedge are distinctly different from the transport processes occurring above the wedge. The typical solute residence times associated with steady state saltwater circulation cell beneath a saltwater wedge are at least an order of magnitude higher than the residence times associated with the freshwater flow occurring above the wedge. The experimental dataset showed that it took approximately 6 hours to fully flush the tracer slug when it was released beneath the wedge, and on the other hand, it took about 30 minutes to flush the tracer slug when it was released above the wedge. The experimental data also indicated that the tracer slugs released below the wedge did not follow an idealized circular flow path commonly depicted in textbooks [*Fetter*, 2001; *Goswami et al.*, 2009]. Due to dispersion effects, the plume attained an elongated shape as it approached the interface. Once the interface was reached, a diffused fraction of the plume transported rather rapidly along the mixing zone and discharged out as a narrow finger. The modeling results for both small and large scale systems showed similar transport patterns. The modeling data also confirmed that dispersion plays an important role in controlling the amount of saltwater flux recirculated beneath a wedge. Model simulations show that when mixing across the wedge was allowed to increase (by using high dispersivity values) the amount saltwater flux circulated beneath the wedge also increased. The percentage of recirculated saltwater flow in a system correlates well with a dimensionless flux parameter, proposed by Smith [2004], for a variety of problems of different scales. While the experimental

results showed that the saltwater flux was about an order magnitude less than the freshwater flux, the theoretical modeling results show that when the value of dispersion is high the saltwater flux could be comparable (or even be higher) than the freshwater flux. These theoretical results were consistent with the results reported in Smith (2004).

The insights gained from this study help us better understand the solute exchange processes occurring between terrestrial and marine waters. The current and Smith (2004) studies, however, have focused only on understanding steady-state systems with a constant sea level boundary condition. Further studies are needed to study dynamic systems which can be influenced by transient boundary conditions which are impacted by tidal cycles and other long term changes such as sea level rise. It will be also interesting to quantify the impacts of mixing due to fluctuations transport velocities induced by changes in boundary conditions, changes in recharge fluxes, and perturbations arising from spatial heterogeneities.

Chapter 5

CONCLUSIONS AND RECOMMENDATIONS

6.1 Summary and Conclusions

The overall goal of this research is to develop a better scientific understanding of the dynamics of a saltwater intrusion and the associated transport processes in coastal groundwater aquifers. Our first objective of this investigation is to understand the long term impacts of sea-level rise on saltwater intrusion processes in confined and unconfined coastal aquifers. We completed numerical simulations for a field-scale problem with a sea level boundary rising with time. Numerical results provided conceptual insights into the transient effects of sea-level rise on saltwater intrusion in coastal aquifers. The simulation results demonstrated that the rising sea would initially force the wedge to migrate inland; however, the rise would also result in lifting of the regional groundwater table which in-turn would naturally drive the wedge back towards the sea. Due to this self-reversal process, the impact of sea level rise will be negligible on the steady-state salt wedge if the total freshwater discharge in the system remained constant. The self-reversal process will also be active in unconfined aquifers; however, in unconfined systems there would be some level of intrusion caused due to the increase in the value of aquifer transmissivity (or saturated aquifer thickness). However, it is important to note that this numerical investigation ignored inundation of low lying coastal areas due to sea-level rise and the associated movement of the coastline. Future studies should investigate these effects.

The result of the first phase of this study demonstrated the amount of freshwater flux transmitted through the system is most important fundamental parameter that would have the

greatest impact on the dynamics of saltwater wedges in coastal aquifers. Therefore, the second objective of this study is to conduct experimental studies to investigate the dynamics of saltwater intrusion processes in an unconfined aquifer involving different types of flux-type boundary conditions. We investigated the influence of variations in regional flow and recharge flows (resulting from changes in local and regional rainfall patterns, respectively) on a salt wedge using a laboratory-scale aquifer model. Both transient and steady-state data were collected from two types of experiments namely the areal-recharge experiment and regional-flow experiment. The experimental results were simulated using the SEAWAT numerical code. The experimental data themselves are unique and can be used as benchmarks for testing numerical codes that use different types of flux-type boundary conditions. In addition, based on the results of the transient experiments, we hypothesized that the times scales associated with the salt wedge intrusion step (where the wedge moved in towards the land due to reduction in groundwater recharge) is larger than the times scales associated with salt wedge recession step (where the wedge moved back towards the sea due to increase in recharge). This implies that if natural fluxes are restored, it will require relatively less time to drive the wedge backward and restore a saltwater contaminated aquifer. Clearly, this is an important result that has an enormous practical implication for managing coastal aquifers.

Many of the shallow coastal unconfined aquifers are routinely contaminated by various type of chemical discharges released from a variety of anthropogenic sources (Westbrook et al., 2005). Furthermore, regional groundwater flow can also transport large amount of nutrients, which then could be exchanged across the salt wedge. Therefore, the third objective of this study is to conduct laboratory studies to investigate the contaminant transport processes near a salt wedge. We completed laboratory experiments to study solute transport patterns in both fresh and

salt water regions present above and below a saltwater wedge, respectively. The experimental

data showed that it took approximately 6 hours to fully flush a tracer slug released beneath the

wedge, whereas it took only about 30 minutes to flush a tracer slug released above the wedge.

This result indicates the rate of transport beneath a saltwater wedge will be an order of

magnitude slower than the transport rate above the wedge. Based on the experimental and

numerical results we estimated that the transport times are expected to differ approximately. The

data also indicated that the tracer slugs released below the wedge did not follow the idealized

circular flow path commonly depicted in textbooks. Due dispersion effects, the circular slug

released beneath the wedge attained an elongated shape as it approached the interface. In the

vicinity of the interface, a fraction of the diffused plume transported rather rapidly along the

mixing zone and moved towards the boundary as a narrow finger. The modeling data simulated

for a large scale system also showed similar solute transport patterns. The insights gained from

this study help us better understand the solute transport processes occurring near a saltwater

wedge.

6.2 Recommendations for Future Work

Several additional investigations could be conducted to further extend our understanding

of saltwater intrusion mechanisms in coastal aquifers. First, the findings of this study which

were primarily based on laboratory data and numerical simulation results could be verified in the

field study impacted by climate change effects (i.e., sea-level rise, rainfall variations). The

laboratory efforts focused on understanding an idealized sea level boundary condition that

ignored marine transgression effects, such as a tidal condition and seasonal variation. Future

studies are needed to study dynamic systems which can be influenced by transient boundary

forces that are impacted by tidal cycles and other long term changes such as inundation.

Secondly, the developed two-dimensional code has several computational limitations and should be improved to reduce the simulation time. More robust advection tracking techniques and/or more efficient numerical solvers can be used to speed-up code. The code could be combined with an optimization method to analyze water resource management options in coastal aquifers. Finally, future modeling efforts should focus on coupling density-coupled transport within a multi-species reactive transport formulation to predict the exchange of nutrients and other reactive contaminants between terrestrial to marine waters.

Appendix 1: Transient Variations in the Toe Position (X_T) for 10%, 50% and 90% Isochlor of saltwater wedge
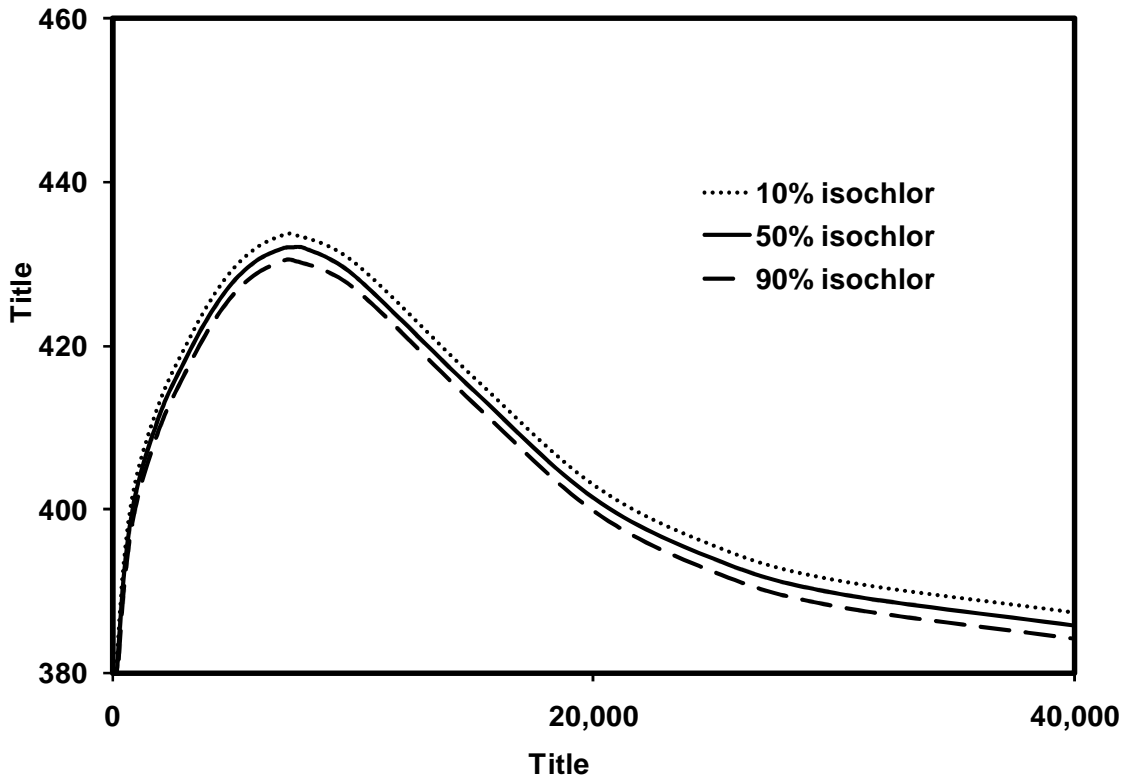
Figure A1. The temporal variation of X_T 10%, 50% and 90% of saltwater wedge.

The behavior of X_T 10% and 90% isochlor of saltwater wedge follow similar pattern to 50% isochlor. Therefore, X_T 50% islcholor is useful to represent the temporal change of saltwater wedge.

Appendix 2 Comparison of Salt-wedge between Central-difference and Upstream-weighting for density-weighting scheme
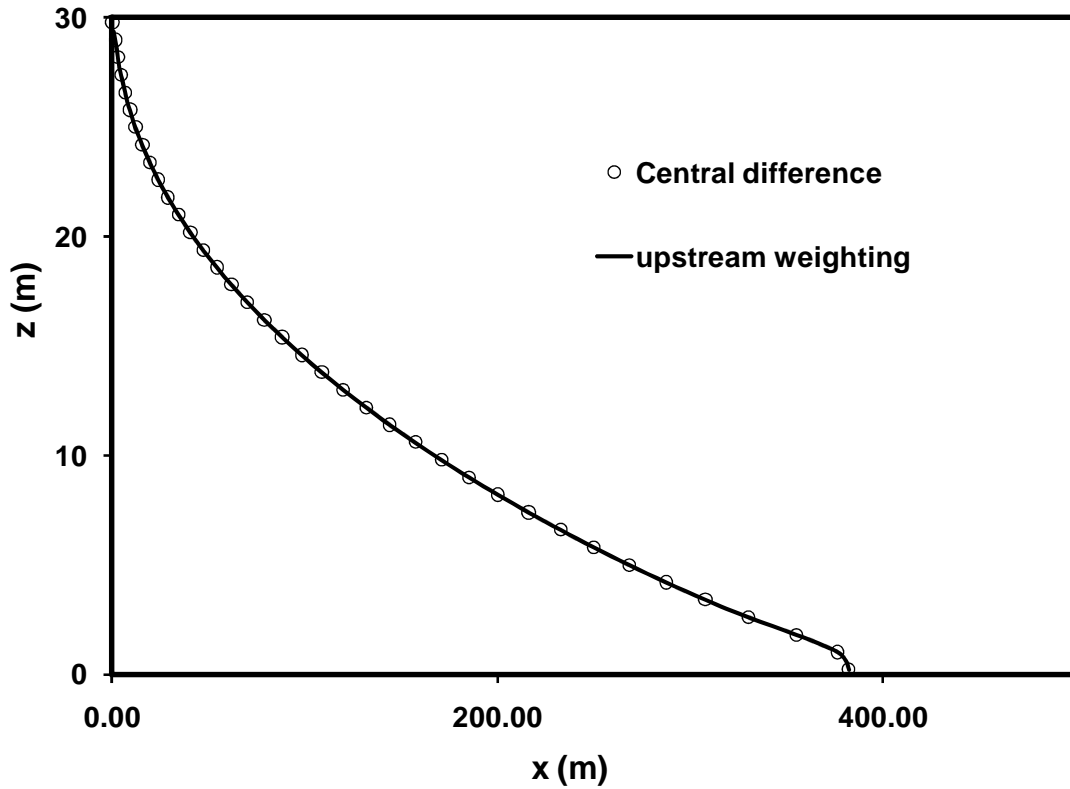
Figure A2. The comparison of saltwater wedge influenced by central difference and upstream weighting for density-weighting scheme.

Based on $\Delta x = 4$ m and $\alpha_L = 1$ m (Table 2.1), the grid Peclet number in the x-direction is $Pe_x = \Delta x/ \alpha_L = 4.0$. Also, based on $\Delta z = 0.4$ m and $\alpha_T = 0.1$ m (Table 2.1), the grid Peclet number in the z-direction is $Pe_z = \Delta z/ \alpha_T = 4.0$. These are relatively large values that may have led to instabilities in the solutions if the central-difference weighting method was used to obtain the solutions. However. we have not observed any instability issues in our solution. We also completed some preliminary simulation to test various schemes and model convergence and found that the wedge location was insensitive to the differencing scheme used.

98

Appendix 3 Comparison of Salt-wedge between FDM and TVD scheme
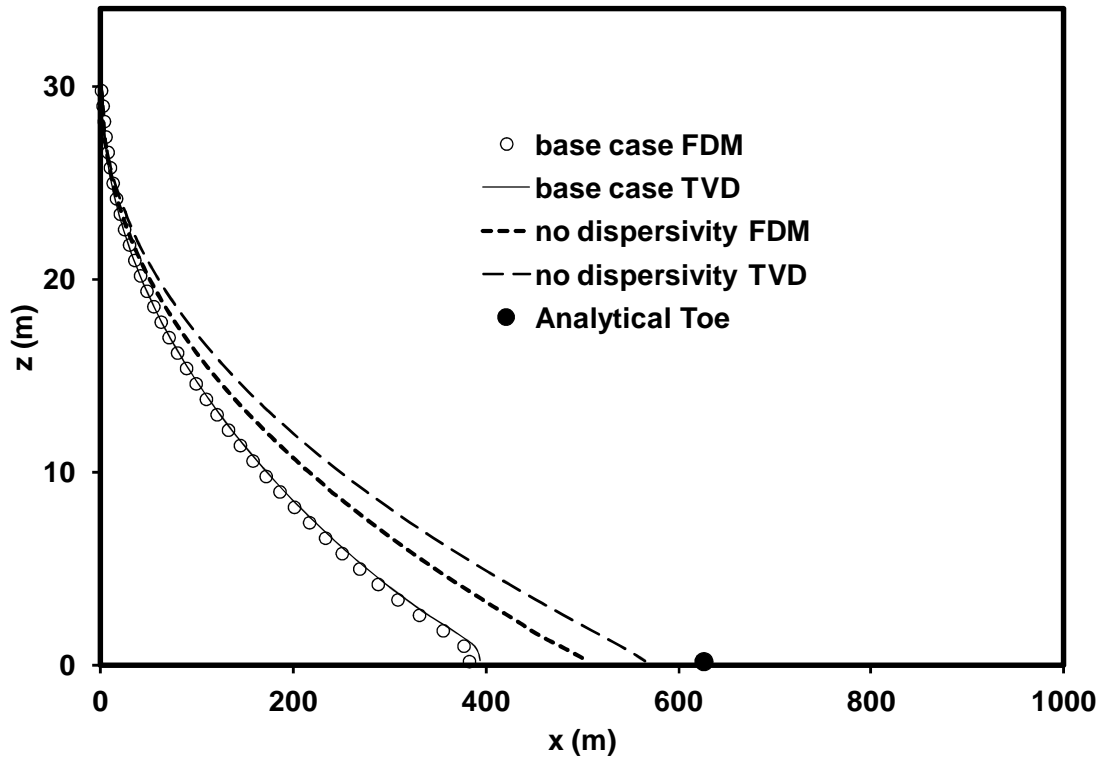
Figure A3. The comparison of saltwater wedge influenced by dispersivity and by advection schemes (Implicit FDM and TVD scheme).

The analytical toe position that computed using by equations of Appendix 1 is 625.5 m. Figure shows that the length of X_T is increased by decreasing dispersivity. For more accurate prediction of toe position, TVD scheme is applied and compared to implicit finite difference scheme. In results, the X_T, 565 m, located close to analytical solution when dispersivity value was 0 for TVD scheme.

Appendix 4 Analytical Comparison of Salt-wedge Toe Positions in Unconfined and Confined Aquifers

The basic concepts used for deriving analytical solutions for salt wedge locations using the sharp-interface approximation are presented by Strack and others [*Cheng et al.*, 2000; *Custodio and Bruggeman*, 1987; *Mantoglou*, 2003; *Strack*, 1976]. Using the sharp-interface approach, the toe position (X_T) in a steady-state, unconfined flow system can predicted using the following expression [*Custodio and Bruggeman*, 1987]:

$$X_T = \left(\frac{q^*}{W} + L\right) - \sqrt{\left(\frac{q^*}{W} + L\right)^2 - \delta B_o^2 (1 + \delta)\left(\frac{K}{W}\right)} \tag{1A}$$

Where, q^* is is the depth-averaged flow through the boundary per unit width of the aquifer [L^2T^{-1}], B_o is the depth of aquifer bottom measured from the mean sea level [L]. W is the uniform recharge rate [LT^{-1}], δ is equal to $\frac{\rho_s - \rho_f}{\rho_f}$, where ρ_f is the density of fresh water [ML^{-3}] and ρ_s is the density of saltwater [ML^{-3}]. Note the above equation is purely a function of groundwater flows (or fluxes) and it does not depend on boundary head levels. Hence, the location of the saltwater toe position will be insensitive to changes in head levels at the sea-side boundary.

A similar expression for estimating the toe position in a confined flow system can be derived from the expressions presented by Cheng et al [*Cheng et al.*, 2000] as:

$$X_T = \left(\frac{q^*}{W} + L\right) - \sqrt{\left(\frac{q^*}{W} + L\right)^2 - \delta B^2 \left(\frac{K}{W}\right)} \tag{2A}$$

Where, B is the thickness of the confined aquifer [L]. Equation (2A) is similar to (1A) and the only difference is the $(1 + \delta)$ term. For seawater, the value of the dimensionless parameter $\delta = 0.025$, and hence the term $(1 + \delta) \sim 1$. Therefore, when $B^2 K \sim B_o{}^2 K$ (or when aquifer thicknesses are matched approximately) the X_T values predicted for confined and unconfined flow systems would almost be the same.

Appendix 5 Derivation of Dimensionless Parameters for the Henry Problem and Analysis of

Henry-type Problem with Areal-recharge flux and zero regional flux

Notations

$a = \dfrac{Q\,\rho_0}{kd(\rho_s - \rho_0)}$

$b = D/Q$

$\xi = l/d$, aspect latio.

c = concentration of salt, in mass per unit volume of solution $[ML^{-3}]$.

c_s = concentration of salt in sea water $[ML^{-3}]$.

Q = net fresh-water discharge per unit length of beach $[L^2]$.

u = horizontal velocity $[LT^{-1}]$.

v = vertical velocity $[LT^{-1}]$.

ρ = density of solution $[ML^{-3}]$.

ρ_0= density of freshwater $[ML^{-3}]$.

ρ_s= density of saltwater $[ML^{-3}]$.

φ'= dimensionless stream function

k = permeability of sand $[L^2]$.

d = thickness of aquifer $[L]$.

l = length of aquifer $[L]$.

P = fluid pore pressure $[ML^{-1}T^{-2}]$.

g= acceleration of gravity $[LT^{-2}]$

μ = viscosity of freshwater $[ML^{-1}T^{-1}]$.

q^*_o = flux at the coastline or left boundary $[L^2T^{-1}]$.

N = recharge rate $[LT^{-1}]$.

1. Dimensionless parameter of Henry Problem with regional flux

Scalar form of Darcy's law can be written as:

$$q_x = u = -\frac{k}{\mu}\left(\frac{\partial P}{\partial x}\right) \tag{1}$$

$$q_y = v = -\frac{k}{\mu}\left(\frac{\partial P}{\partial y} + \rho g\right) \tag{2}$$

Stream function definition in dimensionless form

$$u' = \frac{\partial \varphi'}{\partial y'}$$

$$v' = -\frac{\partial \varphi'}{\partial x'}$$

$$\nabla^2 \varphi' = \frac{\partial}{\partial x'}\left(\frac{\partial \varphi'}{\partial x'}\right) + \frac{\partial}{\partial y'}\left(\frac{\partial \varphi'}{\partial y'}\right) = \frac{\partial u'}{\partial x'} - \frac{\partial v'}{\partial x'} \tag{3}$$

From the dimensionless form

$$u' = \frac{ud}{q^*} \ v' = \frac{vd}{q^*} \ x' = \frac{x}{d}, \ y' = \frac{y}{d}, \ c' = \frac{C}{C_s}, \ \rho' = \frac{\rho - \rho_o}{\rho_s - \rho_o}$$

Dimensionless derivation

$$\frac{\partial x}{\partial x'} = d$$

$$\frac{\partial y}{\partial y'} = d$$

$$\frac{\partial u'}{\partial y'} = \frac{\partial}{\partial y'}\left(\frac{ud}{q^*}\right) = \frac{d}{q^*}\frac{\partial u}{\partial y}\frac{\partial y}{\partial y'} = \frac{d^2}{q^*}\frac{\partial u}{\partial y}$$

$$\frac{\partial v'}{\partial x'} = \frac{\partial}{\partial x'}\left(\frac{vd}{q^*}\right) = \frac{d}{q^*}\frac{\partial v}{\partial x}\frac{\partial x}{\partial x'} = \frac{d^2}{q^*}\frac{\partial v}{\partial x}$$

$$\frac{\partial C'}{\partial x'} = \frac{\partial}{\partial x'}\left(\frac{C}{C_s}\right) = \frac{1}{C_s}\frac{\partial C}{\partial x}\frac{\partial x}{\partial x'} = \frac{d}{C_s}\frac{\partial C}{\partial x}$$

103

$$\frac{\partial \rho^{'}}{\partial x^{'}} = \frac{\partial}{\partial x^{'}}\left(\frac{\rho - \rho_o}{\rho_s - \rho_o}\right) = \frac{1}{\rho_s - \rho_o}\frac{\partial \rho}{\partial x}\frac{\partial x}{\partial x^{'}} = \frac{d}{\rho_s - \rho_o}\frac{\partial \rho}{\partial x}$$

Using these dimensionless form

Equation (3) is converted into dimensioned form

$$\nabla^2 \varphi^{'} = \frac{\partial u^{'}}{\partial x^{'}} - \frac{\partial v^{'}}{\partial x^{'}} = \frac{d^2}{q^*}\frac{\partial u}{\partial y} - \frac{d^2}{q^*}\frac{\partial v}{\partial x} = \frac{d^2}{q^*}\left(\frac{\partial u}{\partial y} - \frac{\partial v}{\partial x}\right)$$

$\frac{\partial u}{\partial y}, \frac{\partial v}{\partial x}$ terms are transformed in terms of pressure,

$$\frac{\partial u}{\partial y} = \frac{\partial}{\partial y}\left[-\frac{k}{\mu}\left(\frac{\partial P}{\partial x}\right)\right] = \frac{k}{\mu}\frac{\partial P}{\partial x \partial y}$$

5)

$$\frac{\partial v}{\partial x} = \frac{\partial}{\partial x}\left[-\frac{k}{\mu}\left(\frac{\partial P}{\partial y} + \rho g\right)\right] = \frac{k}{\mu}\frac{\partial P}{\partial x \partial y} - \frac{kg}{\mu}\frac{\partial \rho}{\partial x}$$

6)

When Subtract between equation (6) from (5) is

$$\frac{\partial u}{\partial y} - \frac{\partial v}{\partial x} = g\frac{\partial \rho}{\partial x}$$

Therefore

$$\nabla^2 \varphi^{'} = \frac{d^2}{q^*}\left(\frac{\partial u}{\partial y} - \frac{\partial v}{\partial x}\right) = \frac{d^2}{q^*}\left(\frac{kg}{\mu}\frac{\partial \rho}{\partial x}\right) = \frac{d^2}{q^*}\left(\frac{\mu_f K}{\mu \rho_o}\frac{\rho_s - \rho_o}{d}\frac{\partial \rho^{'}}{\partial x^{'}}\right) = \frac{Kd(\rho_s - \rho_o)}{q^*}\frac{\partial c^{'}}{\partial x^{'}}$$

using

$$K = \frac{k\rho_o g}{\mu_f}$$

$$\frac{\partial \rho}{\partial x} = \frac{\rho_s - \rho_o}{d}\frac{\partial \rho^{'}}{\partial x^{'}}$$

$$\frac{\partial \rho^{'}}{\partial x^{'}} = \frac{\partial c^{'}}{\partial x^{'}}$$

2. Dimensionless parameter of Henry Problem with areal-recharge flux

$$q^* = q^*_o - Nx = f(x)$$

$$\frac{\partial q^*}{\partial x} = -N$$

From the dimensionless form

$$u' = \frac{ud}{q^*_o - Nx}, \quad v' = \frac{vd}{q^*_o - Nx}, \quad x' = \frac{x}{d}, \quad y' = \frac{y}{d}, \quad c' = \frac{C}{C_s}, \quad \rho' = \frac{\rho - \rho_o}{\rho_s - \rho_o}$$

Dimensionless derivation

$$\frac{\partial x}{\partial x'} = d$$

$$\frac{\partial y}{\partial y'} = d$$

$$\frac{\partial u'}{\partial y'} = \frac{\partial}{\partial y'}\left(\frac{ud}{q^*}\right) = \frac{d}{q^*}\frac{\partial u}{\partial y}\frac{\partial y}{\partial y'} = \frac{d^2}{q^*}\frac{\partial u}{\partial y}$$

$$\frac{\partial v'}{\partial x'} = \frac{\partial}{\partial x'}\left(\frac{vd}{q^*}\right) = d\left(-\frac{v}{q^{*2}}\frac{\partial q^*}{\partial x}\frac{\partial x}{\partial x'} + \frac{1}{q^*}\frac{\partial v}{\partial x}\frac{\partial x}{\partial x'}\right) = d\left(-\frac{v}{q^{*2}}(-N)d + \frac{1}{q^*}\frac{\partial v}{\partial x}d\right)$$

$$= \frac{d^2}{q^{*2}}\left(Nv + q^*\frac{\partial v}{\partial x}\right)$$

$$\frac{\partial C'}{\partial x'} = \frac{\partial}{\partial x'}\left(\frac{C}{C_s}\right) = \frac{1}{C_s}\frac{\partial C}{\partial x}\frac{\partial x}{\partial x'} = \frac{d}{C_s}\frac{\partial C}{\partial x}$$

$$\frac{\partial \rho'}{\partial x'} = \frac{\partial}{\partial x'}\left(\frac{\rho - \rho_o}{\rho_s - \rho_o}\right) = \frac{1}{\rho_s - \rho_o}\frac{\partial \rho}{\partial x}\frac{\partial x}{\partial x'} = \frac{d}{\rho_s - \rho_o}\frac{\partial \rho}{\partial x}$$

Equation (3) is converted into dimensioned form

$$\nabla^2 \varphi' = \frac{\partial u'}{\partial x'} - \frac{\partial v'}{\partial x'} = \frac{d^2}{q^*}\frac{\partial u}{\partial y} - \frac{d^2}{q^{*2}}\left(Nv + q^*\frac{\partial v}{\partial x}\right) = \frac{d^2}{q^*}\left(\frac{\partial u}{\partial y} - \frac{\partial v}{\partial x}\right) - \frac{d^2}{q^{*2}}Nv$$

Due to the presence of the last term, which has dimensions, we were unable to cast this problem in a fully non-dimensional form. Further analysis is needed to study this problem.

Appendix 6 Development of Two-dimensional Numerical Code for Simulating Saltwater
Transport in Groundwater Systems

A7.1.Introduction

In the published literature, several numerical codes are available for simulating density-coupled flow problems. The most commonly used codes are: SEAWAT [*Guo and Langevin*, 2002] which is based on a finite-difference formulation and FEFLOW [*Diersch*, 2002] and SUTRA [*Voss and Provost*, 2002] which are based on a finite-element formulation. The source code for SEAWAT uses a modified version of the USGS groundwater model MODFLOW to simulate equivalent freshwater head as the principal dependent variable. In addition, it uses the popular solution transport code MT3DMS to simulate salt and other solute transport processes. Despite the availability of these public-domain/commercial codes, many researchers have pointed out the need for more robust density coupled flow and transport models to study more complex problems (e.g. metal leachate migration, transport of zero-valent iron, and redox controlled dense metal plume transport, to name a few) [*Goswami et al.*, 2012; *Oostrom et al.*, 1992; *Schincariol and Schwartz*, 1990]. *Goswami et al. [2012]*, for example, has shown that there are still several inaccuracies in simulating certain variable-density systems and hence more research is needed to formulate computationally efficient codes to solve these systems.

Henry problem and Elder problem are commonly used benchmark problems for verifying density-dependent groundwater codes. Simpson and Clement [2003] studied these two benchmark problems using a coupled and uncoupled approach. The test showed that the Elder problem is better than the Henry problem for testing variable-density codes.

The Henry problem, however, is the only variable density problem that has a semi-analytical solution [*Henry*, 1964]. Henry used an analytical framework to define the location and shape of the interface under a constant seaward freshwater flow moving toward an oceanic boundary. Since Henry's initial effort, several other analytical and numerical solutions have been developed for the original Henry problem by Pinder and Cooper [1970], Lee and Cheng [1974], Segol et al. [1975], Frind [1982], Huyakorn et al.[1987], and Voss and Souza [1987]. These studies have tested and modified some of the original parameters to fit Henry's solution; Croucher and O'sullivan [1995], reviewed all these studies and concluded that Henry's original analytical solution might have a minor error. Segol [1994] reinvestigated the errors associated with the Henry solution and suggested some corrections. Simpson and Clement [2004] developed an improved Henry problem. Goswami and Clement [2007] completed experimental studies to develop a new benchmark dataset and used the coupled-uncoupled analysis to test the worthiness of the new experimental problem for testing density-coupling effects. The results of the analysis showed that the proposed experimental benchmark problem is a more robust alternative to the traditional Henry problem.

The objective of the present work is to develop a computationally efficient finite-difference algorithm that can solve a wide variety of two-dimensional, density-dependent flow problems in saturated groundwater systems. The code was then tested using several benchmark problems discussed in the previous section. The numerical code is built in Microsoft Excel based Visual Basic framework. The finite-difference MODFLOW-family variable density flow code SEAWAT [*Guo and Langevin*, 2002] was also used to simulate the benchmark datasets. The model uses the pressure-based, finite-difference approach for formulating the governing flow equations. The pressure based approach is relatively simple and direct compared to other

head-based formulations. For solving the solute transport, the advection process was solved using the third-order TVD scheme and the dispersion/source terms are solved using implicit finite-difference scheme.

A7.2 Governing Equation

The governing equations for density-dependent saturated flow through a two-dimensional homogeneous and isotropic porous medium can be expressed as:

$$\frac{\partial}{\partial x}\left[\frac{K}{g}\left(\frac{\partial P}{\partial x}\right)\right] + \frac{\partial}{\partial z}\left[\frac{K}{g}\left(\frac{\partial P}{\partial z} - \rho g\right)\right] = \rho S_p \frac{\partial P}{\partial t} + \theta E \frac{\partial C}{\partial t} \qquad (A7.1)$$

where, S_p $[M^{-1}LT^2]$ is the specific storage in terms of pressure $\left(= \frac{S_s}{\rho_f g}\right)$, P $[ML^{-1}T^{-2}]$ is pressure, ρ $[ML^{-3}]$ is the fluid density, θ is the water content, K $[LT^{-1}]$ is the hydraulic conductivity, t $[T]$ is time and x and z are the Cartesian coordinates, E is the density concentration slope. The first term in the right-hand side of equation (A7.1) represents the rate of fluid mass accumulation due to ground-water storage effects (for example, due to the compressibility of the bulk porous material and fluid compressibility). The second term in the right-hand side of the equation represents the rate of fluid mass accumulation due to the change of solute concentration.

The two-dimensional transport is modeled using the advection-dispersion equation, which is solved using the operator split strategy. The governing equation and the operator split version of the transport equations can be written as:

$$\frac{\partial C}{\partial t} = -V_x \frac{\partial C}{\partial x} - V_y \frac{\partial C}{\partial y} + \frac{\partial}{\partial x}\left(D_x \frac{\partial C}{\partial x}\right) + \frac{\partial}{\partial y}\left(D_y \frac{\partial C}{\partial y}\right)$$

(A7.2)

$$\frac{\partial C}{\partial t} = -V_x \frac{\partial C}{\partial x} - V_y \frac{\partial C}{\partial y} \tag{A7.2a}$$

$$\frac{\partial \overline{C}}{\partial t} = \frac{\partial}{\partial x}(D_x \frac{\partial \overline{C}}{\partial x}) + \frac{\partial}{\partial y}(D_y \frac{\partial \overline{C}}{\partial y}) \tag{A75.2b}$$

where, V_x and V_y [L/T] are velocity, C [ML^{-3}] is the solute concentration, D_x and D_y [L^2/T] are are the hydrodynamic dispersion coefficient.

In the operation split method, the advection part of the equation is solved as shown in equation (A7.2a) using TVD package. Subsequently, the concentration obtained from advection ($\overline{C}$) is used to solve the dispersion part of the equation as shown in equation (A7.2b) using Implicit FDM. To calculate velocity at nodes, the specific discharge is divided by porosity. The general expression for specific discharge (Darcy flux) can be written as:

$$q_x = -\frac{k_x}{\mu} \frac{\partial P}{\partial x}$$

$$q_z = -\frac{k_z}{\mu} (\frac{\partial P}{\partial z} + \rho g) \tag{A7.3}$$

where q_x and q_x are the individual component of specific discharge, P is pressure [$ML^{-1}T^{-2}$], ρ is the fluid density [ML^{-3}], g is acceleration due to gravity [LT^{-2}].

Equation (A7.1) and (A7.2) are coupled through equation (A7.4).

$$\rho = \rho_f + EC \tag{A7.4}$$

Based on SI unit, the value of typical seawater concentration is about 35 kg/m3 and the freshwater density is set to 1,000 kg/m^3 and saltwater density is set to 1,025 kg/m^3 with the density slope of 0.714 ($= \frac{\text{density difference, 25 kg/m}^3}{\text{Saltwater concentration, 35 kg/m}^3}$).

A7.3 Model Development

Flow Equation

$$\frac{\partial}{\partial x}\left[\frac{K}{g}\left(\frac{\partial P}{\partial x}\right)\right] + \frac{\partial}{\partial z}\left[\frac{K}{g}\left(\frac{\partial P}{\partial z} - \rho g\right)\right] \tag{A7.5a}$$

$$\approx \frac{K}{g\Delta x}\left[\left(\frac{P_{i+1,j}{}^{m,n} - P_{i,j}{}^{m,n}}{\Delta x}\right) - \left(\frac{P_{i,j}{}^{m,n} - P_{i-1,j}{}^{m,n}}{\Delta x}\right)\right]$$

$$+ \frac{K}{g\Delta y}\left[\left(\frac{P_{i,j+1}{}^{m,n} - P_{i,j}{}^{m,n}}{\Delta y}\right) - \left(\frac{P_{i,j}{}^{m,n} - P_{i,j-1}{}^{m,n}}{\Delta y}\right)\right]$$

$$- \frac{K}{g\Delta y}\left[\rho_{i+\frac{1}{2},j}{}^{m-1,n}g - \rho_{i-\frac{1}{2},j}{}^{m-1,n}g\right]$$

where n denotes the nth discrete time level, t^n, when the solution is known, and m is the Picard iteration level, $P_{i,j}$ is the pressure head at node ij. The subscripts i+1/2, i-1/2 refer to the value between two neighboring cells. The density between two cells expressed as average value. The nodal order matches the numbering order of VBA language for all formulation in this study. The current and previous iteration levels are denoted as m and m-1, respectively.

$$\rho S_p \frac{\partial P}{\partial t} + \theta E \frac{\partial C}{\partial t} \approx \rho_{i,j} S_p \frac{P_{i,j}{}^{m,n} - P_{i,j}{}^{n-1}}{\Delta t} + \theta E \frac{C_{i,j}{}^{m-1,n} - C_{i,j}{}^{n-1}}{\Delta t} \tag{A7.5b}$$

where, $\Delta t = t^n - t^{n-1}$ is the time step, which in general is set to maintain acceptably small temporal variation in pressure head.

The finite difference form reduced to

$$\text{a1 } P_{i-1,j}{}^{m,n} + \text{b1 } P_{i,j-1}{}^{m,n} + \text{c1 } P_{i,j}{}^{m,n} + \text{d1 } P_{i,j+1}{}^{m,n} + \text{e1 } P_{i+1,j}{}^{m,n} = \text{RHS} \qquad \text{(A7.6)}$$

where,

$$a1 = -\frac{K_x}{g\Delta x^2}$$

$$b2 = -\frac{K_z}{g\Delta z^2}$$

$$c1 = 2\left(\frac{K_z}{g\Delta x^2} + \frac{K_z}{g\Delta z^2}\right) + \rho_{i,j}\frac{S_p}{\Delta t}$$

$$d1 = -\frac{K_z}{g\Delta z^2}$$

$$e1 = -\frac{K_x}{g\Delta x^2}$$

$$\text{RHS} = \frac{K_z}{2\Delta z}\left[\rho_{i+1,j}{}^{m-1,n} - \rho_{i-1,j}{}^{m-1,n}\right] + \rho_{i,j}\frac{S_p}{\Delta t}P_{i,j}{}^{n-1} - \frac{\theta E}{\Delta t}(C_{i,j}{}^{m-1,n} - C_{i,j}{}^{n-1})$$

Eq. (A7.6) applies to all interior nodes: at boundary nodes this equation is modified to reflect the appropriate boundary conditions. This would lead to a system of linear equations of the form:

$$A \cdot \widehat{P} = b \qquad\qquad\qquad \text{(A7.7)}$$

Where, A is a banded square matrix, $\widehat{P}$ is the vector of unknown pressure at the current time level n and iteration level, m, and b is the forcing vector. The set of linear algebraic equations are solved using a banded version of a Gauss–elimination solver.

Transport Equation

The linear formulation for TVD scheme for advection package is described below. Equation (A7.7a) is spatial formulation and equation (A7.7b) is temporal formulation.

$$-V_x \frac{\partial C}{\partial x} - V_y \frac{\partial C}{\partial y}$$

$$\approx -\frac{V_{i,j+1/2} C^n_{i,j+1/2} - V_{i,j-1/2} C^n_{i,j-1/2}}{\Delta y} - \frac{V_{i+1/2,j} C^n_{i+1/2,j} - V_{i-1/2,j} C^n_{i-1/2,j}}{\Delta x} \qquad \text{(A7.7a)}$$

$$\frac{\partial C}{\partial t} \approx \frac{C^{n+1}_{i,j} - C^n_{i,j}}{\Delta t} \qquad \text{(A7.7b)}$$

The TVD scheme adopts a universal flux limiting procedure to minimize numerical oscillations which may occur if sharp concentration fronts are involved. This scheme is mass conservative, without excessive numerical dispersion, and essentially oscillation-free. Appendix 8 illustrates the detailed TVD formulation procedure and the application of universal limiter.

The implicit FDM formulation is described below for dispersion package. Equation (A7.8a) is spatial formulation and equation (A7.8b) is temporal formulation.

$$-\frac{\partial}{\partial x}\left(D_x \frac{\partial C}{\partial x}\right) + \frac{\partial}{\partial y}\left(D_y \frac{\partial C}{\partial y}\right)$$

$$\approx \frac{1}{\Delta x}\left[D^{m-1,n}_{i+\frac{1}{2},j} \left(\frac{C_{i+1,j}{}^{m,n} - C_{i,j}{}^{m,n}}{\Delta x}\right) - D^{m-1,n}_{i-\frac{1}{2},j} \left(\frac{C_{i,j}{}^{m,n} - C_{i-1,j}{}^{m,n}}{\Delta x}\right) \right] \qquad \text{(A7.8a)}$$

$$+ \frac{1}{\Delta x}\left[D^{m-1,n}_{i,j+\frac{1}{2}} \left(\frac{C_{i,j}{}^{m,n} - C_{i,j-1}{}^{m,n}}{\Delta x}\right) - D^{m-1,n}_{i,j-\frac{1}{2}} \left(\frac{C_{i,j}{}^{m,n} - C_{i,j-1}{}^{m,n}}{\Delta x}\right) \right]$$

$$\frac{\partial C}{\partial t} \approx \frac{C^{n+1}_{i,j} - C^n_{i,j}}{\Delta t} \qquad \text{(A7.8b)}$$

Note that the average dispersion tensor used in the spatial terms is the value that was updated by the previous iteration step, m-1. The value is calculated explicitly so that the equation has only concentration as an independent variable to solve in linear matrix.

The general expression for finite difference form is

$$a_2 C_{i-1,j}{}^{m,n} + b_2 C_{i,j-1}{}^{m,n} + c_2 C_{i,j}{}^{m,n} + d_2 C_{i,j+1}{}^{m,n} + e_2 C_{i+1,j}{}^{m,n} = \text{RHS} \qquad \text{(A7.9)}$$

where,

$$a_2 = D_{x_{i-\frac{1}{2},j}}^{m-1,n} \frac{1}{\Delta x^2}$$

$$b_2 = D_{y_{i,j-\frac{1}{2}}}^{m-1,n} \frac{1}{\Delta y^2}$$

$$c_2 = -\frac{1}{\Delta x^2}\left(D_{x_{i-\frac{1}{2},j}}^{m-1,n} + D_{x_{i-\frac{1}{2},j}}^{m-1,n}\right) - \frac{1}{\Delta y^2}\left(D_{y_{i,j-\frac{1}{2}}}^{m-1,n} + D_{y_{i,j+\frac{1}{2}}}^{m-1,n}\right) - 1$$

$$d_2 = D_{y_{i,j+\frac{1}{2}}}^{m-1,n} \frac{1}{\Delta y^2}$$

$$e_2 = D_{x_{i+\frac{1}{2},j}}^{m-1,n} \frac{1}{\Delta x^2}$$

$$RHS = \frac{C^{*m,n}_{i,j}}{\Delta t}$$

Eq. (A7.9) applies to all interior nodes: at boundary nodes this equation is modified to reflect the appropriate boundary conditions. The resulting system of linear equations is also solved by the banded Gauss-elimination solver.

Boundary Conditions

Test problems-1, 2 and 4 use Dirichlet boundary condition for freshwater boundary. Test problem-3 uses Numann boundary condition for freshwater inflow. Also, the tank bottom is set to no-flow boundary for all test problems. Saltwater intrusion modifies the concentration at the boundary. The detailed modification is expressed in the model setup for each test problem.

Time Step Determination

Since advection is solved by explicitly, Courant condition is required to limit transport time step, Δt. Courant condition is applied to all simulations to maintain sufficiently small time steps. The length of time step is calculated by Courant condition to satisfy the stability

constraints and accuracy requirements of the transport equation. In this study, saltwater simulation generally set the Courant number to 0.5. The Elder problem decreases the Courant number to 0.1.

A7.3 Results

Test Problem 1: Sinking plume model

The first test problem is an example of dense solute transport. Goswami et al. [2012] provided an experimental and numerical solution conducted in a two-dimensional flow tank using three different numerical techniques available in SEAWAT/MT3DMS. The experiments were designed to represent a sinking groundwater plume and a rising groundwater plume. This problem is also helpful when applied to practical environmental issues such as contaminant transport and tsunami issues in coastal aquifers. The domain and boundary conditions describe a confined aquifer; constant freshwater pressure heads are maintained on the left and the right boundary of the main, respectively (see Figure A7.1). The two-dimensional modeling domain is 225 mm long and 180 mm high. The longitudinal dispersivity value was set to 0.1 mm and transverse dispersivity is set to 0.01 mm. Three stress periods were employed to simulate the following three experimental stages: (1) steady-state conditions prior to injection, (2) injection of freshwater/saltwater slug, and (3) migration of slug through the tank. The time step size was set to an initial minimum value of 0.1 s and a maximum value of 1 s. The Courant number constraint was set to 0.5. Values for this model are presented in Table A7.1.

The simulated results of third state (migration stage) were compared to SEAWAT results and shown in Figure A7.2. The simulation shows good agreement with SEAWAT (See Figure A7.4). The density-dependent sinking study can be also applied to a different composition in fluid from typical seawater or the salt concentration. For example, Kanel et al. [2008] simulated the fate and transport of Zero-valent iron nanoparticles (INP) and stabilized zero-valent iron nanoparticles using poly acrylic acid (S-INP) in porous media under saturated, steady-state flow conditions.

(b)
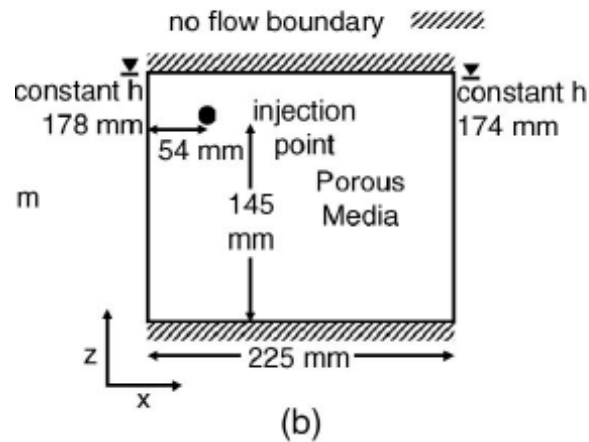
Figure A7.1 Conceptual description of the numerical model used for simulating the sinking-plume experiments (Goswami et al, 2012).

Table A7.1 Summary of numerical model parameters

Property	Symbol	values
Horizontal length	L	23 cm
Vertical Length	h_s	18 cm
Hydraulic conductivity	K	1.16 cm/s
Porosity	n	0.38
Specific storage,	S_s	0.000001cm^{-1}
Longitudinal dispersivity	α_L	0.01 cm
Transverse dispersivity	α_T	0.001 cm
Saltwater concentration	Cs	0.035 g/cm^3
Saltwater density	ρ_s	1.025 g/cm^3
Freshwater density	ρ_f	1.000 g/cm^3
Density slope	E	0.714
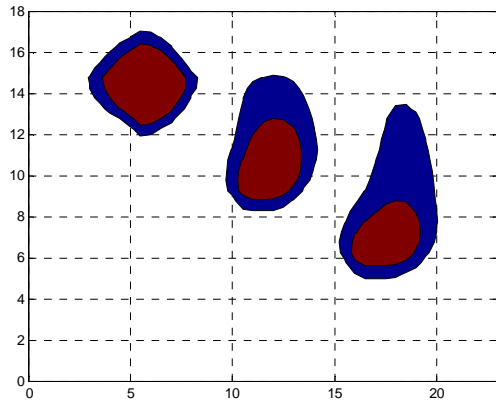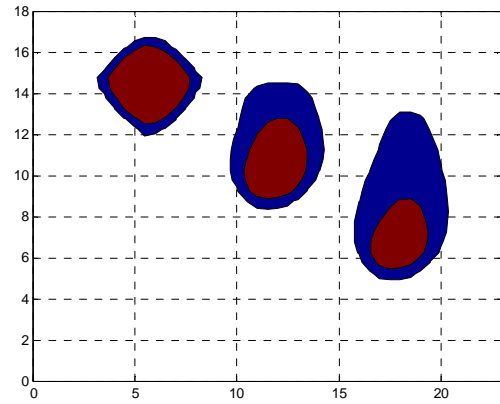
(a) VDFT code   (b) SEAWAT

Figure A7.2 Comparison of VDFT code simulation results against to SEAWAT for the sinking plume experiment at various times at 0 min (left plume) , 2 min (middle) and 4 min (right), Red color > 10% and Blue color 1 – 10 % .

Test Problem 2: Saltwater Intrusion Model

A conceptual model based on Goswami and Clement [2007] was simulated. The saltwater behavior in the saltwater intrusion problem is relatively stable. Goswami and Clement [2007] proposed the experimental data set that can be used as a benchmark problem. The domain and boundary conditions describe a confined aquifer; constant pressure heads are maintained on the left and the right boundary of the main, respectively (see Figure A7.3). This Henry-type problem is useful to understand the role of several hydrodynamic and geologic factors affecting the flow and transport process in the simplified flow system. In order to construct the numerical model, the origin of an x-z coordinate system was set on the lower left-hand corner of the plane. A uniform grid of size 1.0 cm (54 cells in the x-direction and 26 cells in the z-direction) was used to discretize the 53.0 cm $\times$ 26.0 cm dimensional model. The saltwater head is imposed on left boundary where the head is set to 25.5 cm for the entire simulation time. The value of specific storage (Ss) was set to 10^{-6} cm^{-1} for all nodes. All layers are set to confined layer and bottom of the model is set to no-flow condition. Freshwater flux is allowed to penetrate from the right constant-head boundary. The value of 0.05 cm and 0.005 cm were selected for the longitudinal and transversal dispersivity coefficient, respectively. Values for this model are presented in Table A7.2.

Three steady state conditions were selected and simulated using VDFT code and compared to SEAWAT results. The simulation shows good agreement with SEAWAT for the steady-state condition (See Figure A7.4). Transient simulations for an intruding condition and a receding condition also show good agreements (See Figure A7.5).
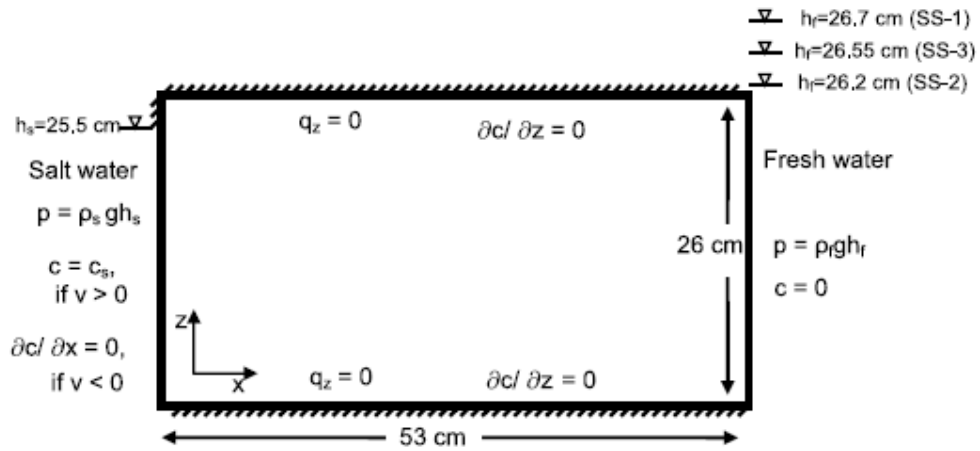
Figure A7.3 Computation domain and boundary conditions used in the numerical model (Goswami and Clement, 2007)

Table A7.2 Summary of numerical model parameters

Property	Symbol	values
Horizontal length	L	53 cm
Saltwater elevation	h_s	26 cm
Hydraulic conductivity	K	1.215 cm/s
Porosity	n	0.385
Specific storage,	S_s	0.000001cm^{-1}
Longitudinal dispersivity	α_L	0.01 cm
Transverse dispersivity	α_T	0.001 cm
Saltwater concentration	Cs	0.0371 g/cm^3
Saltwater density	ρ_s	1.026 g/cm^3
Freshwater density	ρ_f	1.000 g/cm^3
Density Slope	E	0.714

Figure A7.4 Comparison of VDFT code simulation results against to SEAWAT for steady state in saltwater problem.

(a)

(b)

Figure A7.5 Comparison of VDFT code simulation results against to SEAWAT for (a) intruding

and (b) receding condition in saltwater problem.

Test Problem 3: Flux-type Henry Problem
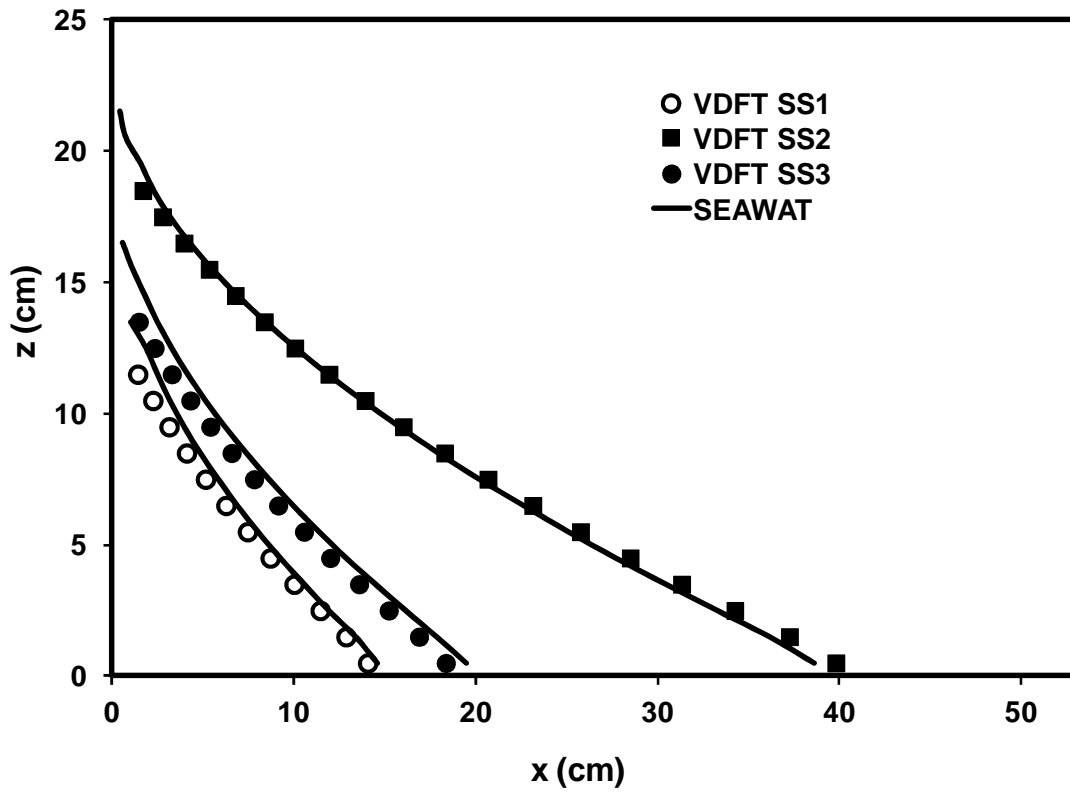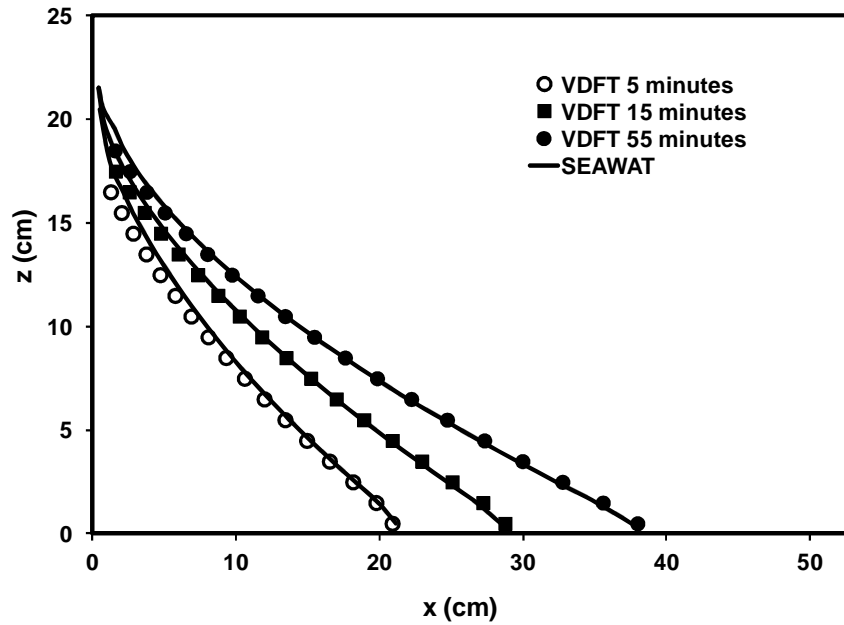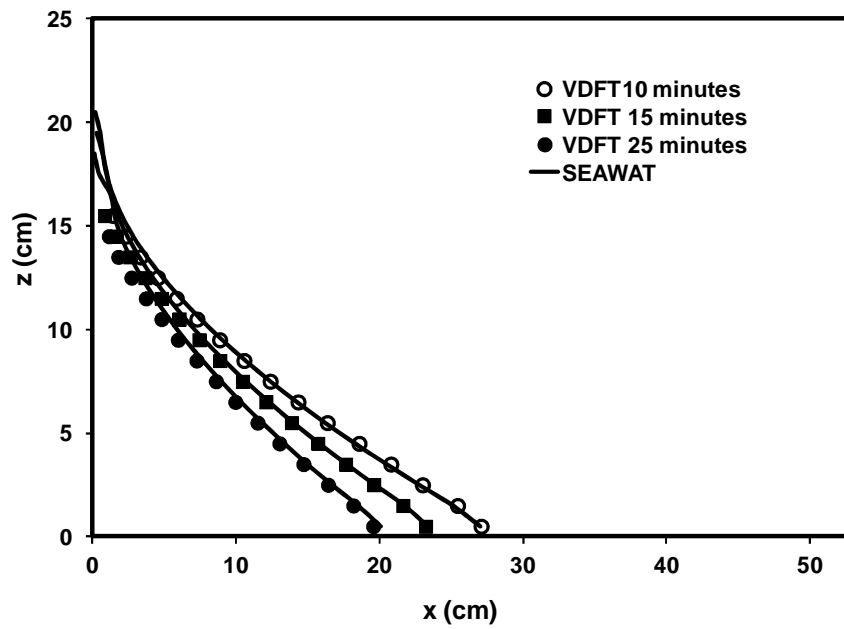
Conceptual models based on original Henry problem [1964]   and modified Henry problem [*Simpson and Clement*, 2004] were simulated. The domain and boundary conditions for the Henry and Modified Henry problem describe a confined aquifer. A constant pressure head is maintained on the right boundary and constant flux is maintained on the left boundary of the main (see Figure A7.6).   In order to construct a numerical model, the origin of an x-z coordinate system was set on the lower left-hand corner of the plane. A uniform grid of size 5.0 cm (41 cells in the x-direction and 20 cells in the z-direction) was used to discretize the 200 cm $\times$ 100 cm dimensional model. The saltwater head is imposed on the right boundary where the head is set to 100 cm for the entire simulation time. The value of specific storage (Ss) was set to 10^{-6} cm^{-1} for all nodes. All layers are set to confined layer and bottom of the model is set to no-flow condition.   The longitudinal and transversal dispersivity coefficients are set to zero.   Values for this model are presented in Table A7.3.

The simulated results for (a) original Henry problem and (b) modified Henry problem were compared to SEAWAT results and shown in Figure A7.7. This difference indicates that the relative importance of the density effects is greater for the modified case where the influence of the boundary forcing is reduced [Simpson and Clement, 2004]. In this figure, bigger discrepancy is shown at the bottom of the model when the modified Henry problem was simulated. The VDFT code is still under development to predict more accurate density effects.
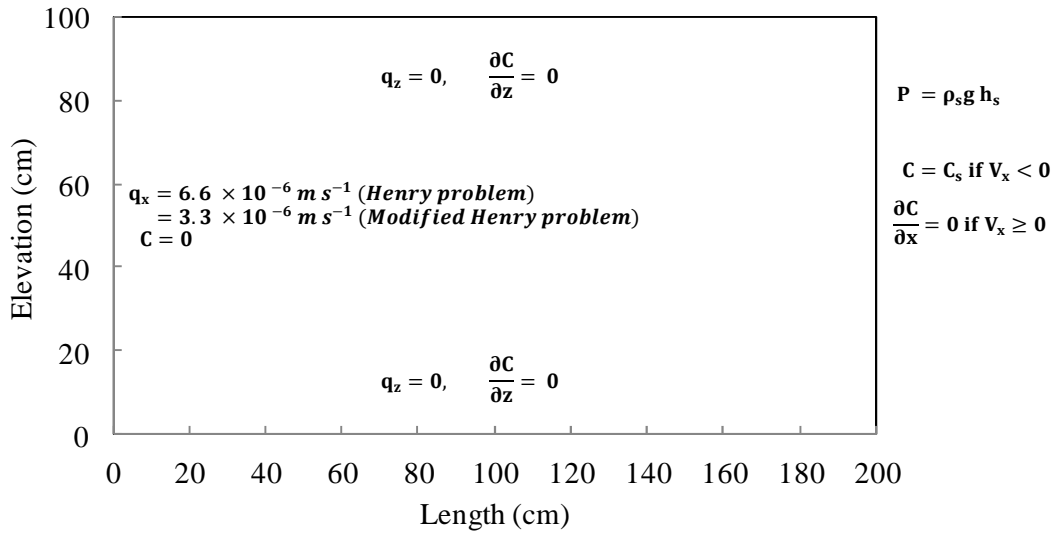
Figure A7. 6 Boundary conditions applied for solving Henry saltwater intrusion Problem (Henry, 1964; Simpson and Clement, 2003).

Table A7.3 Summary of numerical model parameters

Property	Symbol	values
Horizontal length	L	200 cm
Saltwater elevation	h_s	100 m
Freshwater darcy flow	q	6.6×10^{-3} cm/s
Hydraulic conductivity	K	1.0 cm/s
Porosity	n	0.35
Specific storage,	S_s	0 cm^{-1}
Longitudinal dispersivity	α_L	0 cm
Transverse dispersivity	α_T	0 cm
Saltwater concentration	Cs	35 kg/m^3
Saltwater density	ρ_s	1,025 kg/m^3
Freshwater density	ρ_f	1,000 kg/m^3
Density slope	E	0.714
Diffusion coefficient	D_m	1.886×10^{-5} cm^2/s
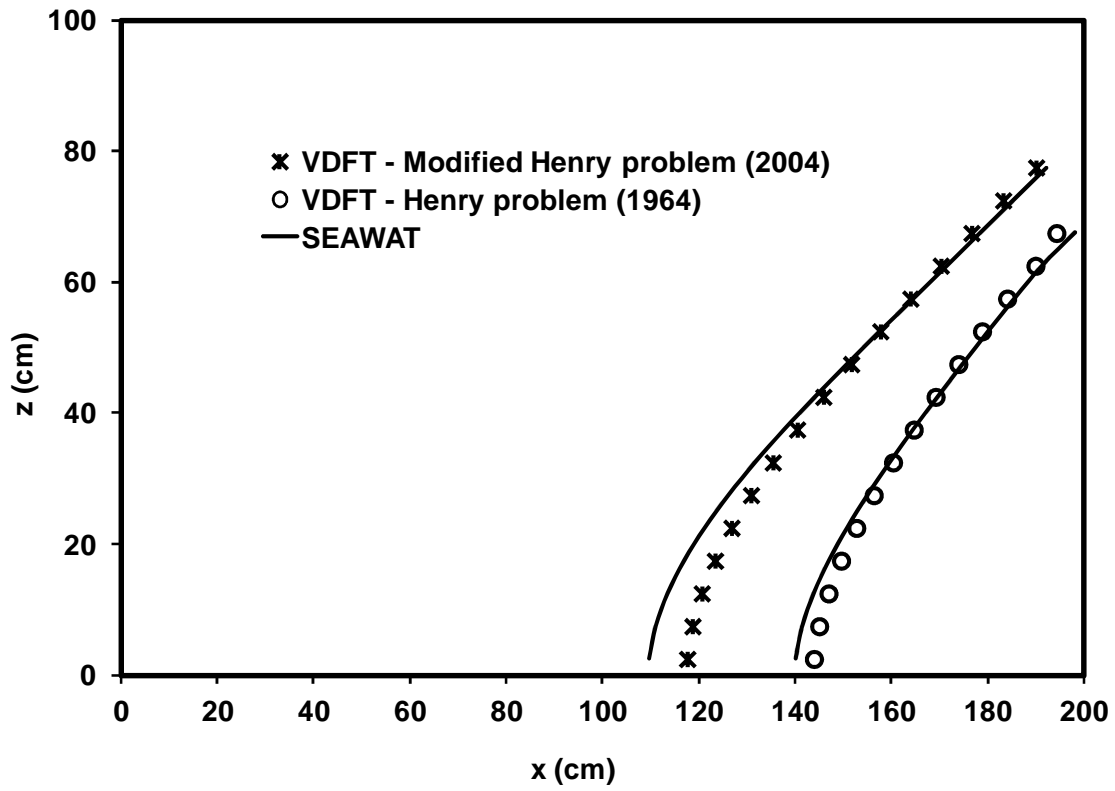
Figure A7.7. Steady-state 50% isochlor distribution for the Henry Problem and the modified Henry problem.

Test Problem 4: Elder Problem

A conceptual model based on original Elder Problem [Elder, 1967] was simulated. This study follow the aquifer property and parameter values suggested by Simpson and Clement [2003]. The domain and boundary conditions for the Elder problem describe a confined aquifer, a zero pressure head is maintained on the left and right upper corner of the domain (see Figure A7.8). In order to construct a numerical model, the origin of an x-z coordinate system was set on the lower left-hand corner of the plane. A grid of size of 16.8 m for x-direction and 6 m of z-direction (44 cells in the x-direction and 25 cells in the z-direction) was used to discretize the 600 m $\times$ 150 m dimensional model. The value of specific storage (Ss) was set to zero for all nodes. All layers are set to confined layer and bottom of the model is set to no-flow condition. The longitudinal and transversal dispersivity coefficients are set to zero. Cells in layer 1 from columns 12 to 33 are imposed by constant concentration with a value of 285.7 kg/m^3. The Courant number is set to 0.1. The model summary is presented in Table A7.3.

The simulated results were compared to SEAWAT results and shown in Figure A7.9. VDFT results show relatively smooth migration downward where SEAWAT shows clear vortices in the model. The VDFT code is still under development to predict more accurate density effects.
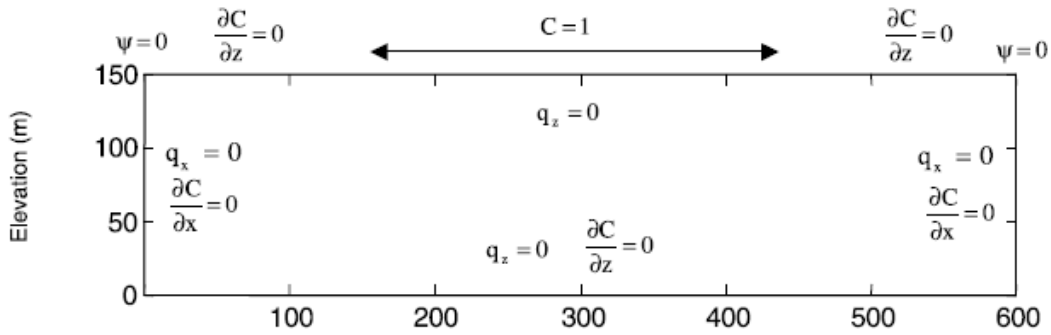
Figure A7.8. Domain and boundary conditions for the Elder problem (Simpson and Clement, 2003).

Table A7.4 Summary of numerical model parameters

Property	Symbol	values
Horizontal length	L	600 m
Saltwater elevation	h_s	150 m
Hydraulic conductivity	K	4.76×10^{-6} cm/s
Porosity	n	0.1
Specific storage,	S_s	0 cm^{-1}
Longitudinal dispersivity	α_L	0 cm
Transverse dispersivity	α_T	0 cm
Saltwater concentration	Cs	286 kg/m^3
Saltwater density	ρ_s	1,200 kg/m^3
Freshwater density	ρ_f	1,000 kg/m^3
Density Slope	E	0.7
Diffusion coefficient	D_m	3.57×10^{-6} cm^2/s
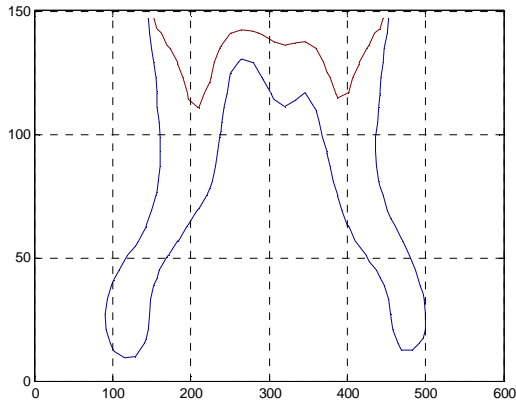
(a) 2 years at SEAWAT
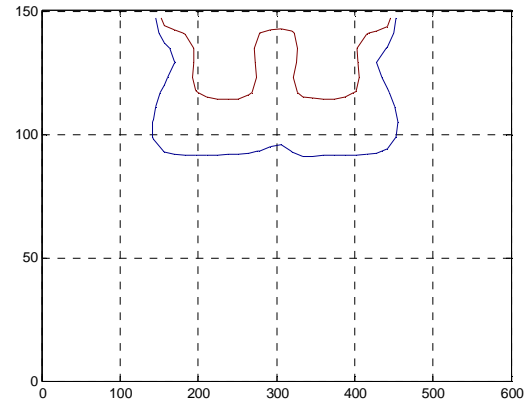
(b) 2 years at VDFT
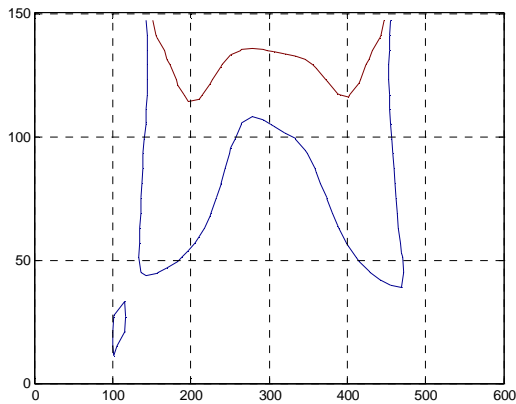
(c) 4 years at SEAWAT
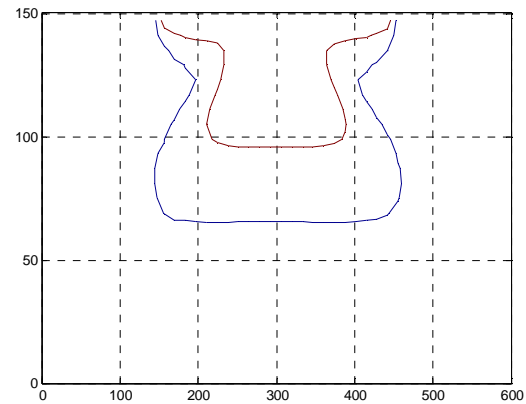
(d) 4 years at VDFT

Figure A7.9. 20% (blue line) and 60% (red line) of the flow pattern of the dense fluid into the aquifer for the Elder Problem.

A7.4 Discussion

The VDFT code currently reproduces the experiment data well; however, some discrepancies where observed for certain benchmark problems (Henry problem and Elder problem). The implicit transport package of VDFT code is still under development, and further work is needed to improve this package.

Appendix 7 Code Formulation based on TVD Scheme for Advection Package

1. General Formulation (assume constant **Δx**)

$$\theta \frac{C_{i,j}^{n+1} - C_{i,j}^n}{\Delta t} = -\frac{q_{i,j+1/2}C_{i,j+1/2}^n - q_{i,j-1/2}C_{i,j-1/2}^n}{\Delta y} - \frac{q_{i+1/2,j}C_{i+1/2,j}^n - q_{i-1/2,j}C_{i-1/2,j}^n}{\Delta x}$$

Rearranging terms

$$C_{i,j}^{n+1} = C_{i,j}^n - (\gamma)_{right}C_{i,j+1/2}^n + (\gamma)_{left}C_{i,j-1/2}^n - (\gamma)_{bottom}C_{i+1/2,j}^n + (\gamma)_{top}C_{i-1/2,j}^n$$

Where the Courant number, γ, is defined as

$$(\gamma)_{left} = \frac{q_{i,j-1/2}\Delta t}{\theta\Delta x} = \frac{v_{xi,j-1/2}\Delta t}{\Delta x}$$

$$(\gamma)_{right} = \frac{q_{i,j+1/2}\Delta t}{\theta\Delta x} = \frac{v_{xi,j+1/2}\Delta t}{\Delta x}$$

$$(\gamma)_{top} = \frac{q_{i-1/2,j}\Delta t}{\theta\Delta y} = \frac{v_{yi-1/2,j}\Delta t}{\Delta y}$$

$$(\gamma)_{bottom} = \frac{q_{i+1/2,j}\Delta t}{\theta\Delta y} = \frac{v_{yi+1/2,j}\Delta t}{\Delta y}$$

Applying the same procedure for third-order polynomial interpolation of nodel concentrations as described in chapter 3 (MT3DMS manual), the concentration values at the left interface can be derived as

$$C_{i,j-1/2}^n = \bar{C}_{i,j-1/2}^n - \frac{d_x}{2}f_x - \frac{d_y}{2}f_y - \frac{(\Delta y^2 - d_y^2)}{6}f_{yy} + \left(\frac{d_x^2}{6} - \frac{\Delta x d_x}{4}\right)f_{xx} + \left(\frac{d_x d_y}{3} - \frac{\Delta y d_x}{4}\right)f_{yx}$$

Where,

$$d_y = v_{xi,j-1/2}\Delta t$$

$$d_x = v_{yi,j-1/2}\Delta t$$

128

$$\bar{C}^n_{i,j-1/2} = \frac{C^n_{i,j-1} + C^n_{i,j}}{2}, \text{ in this study}$$

The normal gradient

$$f_y = \frac{C^n_{i,j} - C^n_{i,j-1}}{\Delta y}$$

The upwind gradient along the y-direction depends on the directions of the velocities

$$f_x = (C^n_{i,j-1} - C^n_{i-1,j-1})/\Delta x \qquad v_{yi,j-1/2} > 0, v_{x\,i,j-1/2} > 0$$

$$= (C^n_{i+1,j-1} - C^n_{i,j-1})/\Delta x \qquad v_{yi,j-1/2} > 0, v_{x\,i,j-1/2} < 0$$

$$= (C^n_{i,j} - C^n_{i-1,j})/\Delta x \qquad v_{yi,j-1/2} < 0, v_{x\,i,j-1/2} > 0$$

$$= (C^n_{i+1,j} - C^n_{i,j})/\Delta x \qquad v_{yi,j-1/2} < 0, v_{x\,i,j-1/2} < 0$$

Based on the first-order derivatives,

Second order derivatives can be calculated below:

$$f_{yy} = \left[(f_y)_{i,j-\frac{1}{2}} - (f_y)_{i,j-1-\frac{1}{2}} \right]/\Delta y \qquad v_{yi,j-1/2} > 0$$

$$= \left[(f_y)_{i,j+\frac{1}{2}} - (f_y)_{i,j-\frac{1}{2}} \right]/\Delta y \qquad v_{yi,j-1/2} < 0$$

$$f_{xx} = \left[(f_x)_{i+\frac{1}{2},j-1} - (f_x)_{i-\frac{1}{2},j-1} \right]/\Delta y \qquad v_{yi,j-1/2} > 0$$

$$= \left[(f_x)_{i+\frac{1}{2},j} - (f_x)_{i-\frac{1}{2},j} \right]/\Delta y \qquad v_{yi,j-1/2} < 0$$

Mixed second-order derivatives (twist terms)

$$f_{yx} = \left[(f_x)_{i-\frac{1}{2},j} - (f_x)_{i-\frac{1}{2},j-1} \right]/\Delta y \qquad v_{xi,j-1/2} > 0$$

$$= \left[(f_x)_{i+\frac{1}{2},j} - (f_x)_{i+\frac{1}{2},j-1} \right]/\Delta y \qquad v_{xi,j-1/2} < 0$$

$$C^n_{i-1/2,j}$$

129

$$C_{i-1/2,j}^n = \bar{C}_{i-1/2,j}^n - \frac{d_x}{2}f_x - \frac{d_y}{2}f_y - \frac{(\Delta x^2 - d_x^2)}{6}f_{xx} + \left(\frac{d_y^2}{6} - \frac{\Delta y d_y}{4}\right)f_{yy} + \left(\frac{d_x d_y}{3} - \frac{\Delta x d_y}{4}\right)f_{xy}$$

Where,

$$d_x = v_{xi-1/2,j}\Delta t$$

$$d_y = v_{yi-1/2,j}\Delta t$$

$$\bar{C}_{i-1/2,j}^n = \frac{C_{i-1,j}^n + C_{i,j}^n}{2}, \text{ in this study}$$

The normal gradient

$$f_x = \frac{C_{i,j}^n - C_{i-1,j}^n}{\Delta x}$$

The upwinding gradient along the y-direction depends on the directions of the velocities

$$f_y = \left(C_{i-1,j}^n - C_{i-1,j-1}^n\right)/\Delta y \qquad v_{yi-1/2,j} > 0, v_{xi-1/2,j} > 0$$

$$= \left(C_{i,j}^n - C_{i,j-1}^n\right)/\Delta y \qquad v_{yi-1/2,j} > 0, v_{xi-1/2,j} < 0$$

$$= \left(C_{i-1,j+1}^n - C_{i-1,j}^n\right)/\Delta y \qquad v_{yi-1/2,j} < 0, v_{xi-1/2,j} > 0$$

$$= \left(C_{i,j+1}^n - C_{i,j}^n\right)/\Delta y \qquad v_{yi-1/2,j} < 0, v_{xi-1/2,j} < 0$$

Based on the first-order derivatives,

Second order derivatives can be calculated below:

$$f_{xx} = \left[(f_x)_{i-\frac{1}{2},j} - (f_x)_{i-1-\frac{1}{2},j}\right]/\Delta x \qquad v_{xi,j-1/2} > 0$$

$$= \left[(f_x)_{i+\frac{1}{2},j} - (f_x)_{i-\frac{1}{2},j}\right]/\Delta x \qquad v_{xi,j-1/2} < 0$$

$$f_{yy} = \left[(f_y)_{i-1,j+\frac{1}{2}} - (f_y)_{i-1,j-\frac{1}{2}}\right]/\Delta y \qquad v_{xi,j-1/2} > 0$$

$$= \left[(f_y)_{i,j+\frac{1}{2}} - (f_y)_{i,j-\frac{1}{2}}\right]/\Delta y \qquad v_{xi,j-1/2} < 0$$

Mixed second-order derivatives (twist terms)

$$f_{xy} = \left[(f_y)_{i,j-\frac{1}{2}} - (f_y)_{i-1,j-\frac{1}{2}} \right] / \Delta x \qquad v_{yi-1/2,j} > 0$$

$$= \left[(f_y)_{i,j+\frac{1}{2}} - (f_y)_{i-1,j+\frac{1}{2}} \right] / \Delta x \qquad v_{yi-1/2,j} < 0$$

2. Limiter Application

$$\tilde{C} = \frac{C - C_{j-2}}{C_j - C_{j-2}}$$

Note   that

$$\tilde{C}_{j-2} = 0 \text{ and } \tilde{C}_j = 1$$

If the concentration profile across the three nodes are monotonic,

$$\tilde{C}_{j-1} \leq \tilde{C}_{j-\frac{1}{2}} \leq 1$$

Which equal to

$$\frac{C_{j-1} - C_{j-2}}{C_j - C_{j-2}} \leq \frac{C_{j-\frac{1}{2}} - C_{j-2}}{C_j - C_{j-2}} \leq 1$$

$$C_{j-1} - C_{j-2} \leq C_{j-\frac{1}{2}} - C_{j-2} \leq C_j - C_{j-2}$$

The right-hand inequality in above equation is insured

$$C_{j-\frac{1}{2}} \leq C_j \qquad \text{constraint (1)}$$

The left-hand inequality in above equation is insured

$$C_{j-\frac{1}{2}} \geq C_{j-1} \qquad \text{constraint (2)}$$

Also, Explicit finite difference solution at note j-1 is

$$C_{j-1}^{n+1} = C_{j-1}^n - Cr\,(C_{j-\frac{1}{2}}^n - C_{j-1-\frac{1}{2}}^n)$$

Is transformed in terms of normalized variables,

$$\tilde{C}_{j-1}^{n+1} = \tilde{C}_{j-1}^n - Cr\,(\tilde{C}_{j-\frac{1}{2}}^n - \tilde{C}_{j-1-\frac{1}{2}}^n)$$

Since

$$\tilde{C}_{j-\frac{1}{2}}^n \geq \tilde{C}_{j-1-\frac{1}{2}}^n \quad \text{due to monotonic}$$

$$0 \leq \tilde{C}_{j-1}^{n+1} \leq \tilde{C}_{j-1}^n \leq 1$$

Left-hand inequality implies

$$0 \leq \tilde{C}_{j-1}^{n+1}$$

$$0 \leq \tilde{C}_{j-1}^n - C_r\,(\tilde{C}_{j-\frac{1}{2}}^n - \tilde{C}_{j-1-\frac{1}{2}}^n)$$

$$\tilde{C}_{j-\frac{1}{2}}^n \leq \tilde{C}_{j-1-\frac{1}{2}}^n + \tilde{C}_{j-1}^n / C_r$$

The worst –case estimate for $\tilde{C}_{j-1-\frac{1}{2}}^n = 0$ results in additional constraints on $\tilde{C}_{j-\frac{1}{2}}^n$:

$$\tilde{C}_{j-\frac{1}{2}}^n \leq \tilde{C}_{j-1}^n / C_r \qquad\qquad \textit{constratint (3)}$$

If $\tilde{C}_{j-\frac{1}{2}}^n$ does not lie with above boundary,

$$\tilde{C}_{j-\frac{1}{2}}^n = \tilde{C}_{j-1}^n$$

Therefore

$$C_{j-\frac{1}{2}}^n = C_{j-1}^n$$

References

Abarca, E., and T. P. Clement (2009), A novel approach for characterizing the mixing zone of a saltwater wedge, *Geophysical Research Letters*, *36*(6).

Abarca, E., J. Carrera, X. Sánchez-Vila, and C. I. Voss (2007a), Quasi-horizontal circulation cells in 3D seawater intrusion, *Journal of Hydrology*, *339*(3-4), 118-129.

Abarca, E., J. Carrera, X. Sánchez-Vila, and M. Dentz (2007b), Anisotropic dispersive Henry problem, *Advances in Water Resources*, *30*(4), 913-926.

Anderson, J., K. Milliken, D. Wallace, A. Rodriguez, and A. Simms (2010), Coastal Impact Underestimated From Rapid Sea Level Rise, *Eos Trans. AGU, 91*(23), 205-206, doi: 10.1029/2010EO230001

Barlow, P. M., and E. G. Reichard (2010), Saltwater intrusion in coastal regions of North America, *Hydrogeology Journal*, *18*(1), 247-260.

Bear, J., and A. H. D. Cheng (2010), *Modeling groundwater flow and contaminant transport*, 1st edition ed., Springer.

Blanchon, P., A. Eisenhauer, J. Fietzke, and V. Liebetrau (2009), Rapid sea-level rise and reef back-stepping at the close of the last interglacial highstand, *Nature*, *458*(7240), 881-884.

Boufadel, M. C. (2000), A mechanistic study of nonlinear solute transport in a groundwater-surface water system under steady state and transient hydraulic conditions, *Water Resour. Res.*, *36*(9), 2549-2565.

Chang, S. W., and T. P. Clement (2012a), Laboratory and numerical investigation of transport processes occurring beneath a saltwater wedge *Journal of Contaminant Hydrology*, *sumbitted*.

Chang, S. W., and T. P. Clement (2012b), Experimental and numerical investigation of saltwater intrusion dynamics in flux controlled groundwater systems, *Water Resources Research*, *doi:10.1029/2012WR012134*, In press.

Chang, S. W., T. P. Clement, M. J. Simpson, and K.-K. Lee (2011), Does sea-level rise have an impact on saltwater intrusion?, *Advances in Water Resources*, *34*(10), 1283-1291.

Cheng, A. H. D., D. Halhal, A. Naji, and D. Ouazar (2000), Pumping optimization in saltwater-intruded coastal aquifers, *Water Resources Research*, *36*(8), 2155-2165.

Clement, T. P., Y. Sun, B. S. Hooker, and J. N. Petersen (1998), Modeling Multispecies Reactive Transport in Ground Water, *Ground Water Monitoring & Remediation*, *18*(2), 79-92.

Croucher, A. E., and M. J. O'Sullivan (1995), The Henry Problem for Saltwater Intrusion, *Water Resour. Res.*, *31*(7), 1809-1814.

Custodio, E., and G. A. Bruggeman (1987), Groundwater problems in coastal areas. Studies and reports in hydrology 45, edited, UNESCO, Paris.

Dausman, A., and C. Langevin (2005), Movement of the saltwater interface in the Surficial Aquifer System in response to hydrologic stresses and water-management practices, Broward County, Florida: USGS Scientific Investigations Report : SIR 2004-5256*Rep.*

Destouni, G., and C. Prieto (2003), On the possibility for generic modeling of submarine groundwater discharge, *Biogeochemistry*, *66*(1), 171-186.

Diersch, H. J. G. (2002), FEFLOW finite element subsurface flow and transport simulation system -user's manual/reference manual/whilte papers. Release 5.0*Rep.*, Berlin.

Elder, J. W. (1967), Steady free convection in a porous medium heated from below, *Journal of Fluid Mechanics*, *27*(01), 29-48.

Feseker, T. (2007), Numerical studies on saltwater intrusion in a coastal aquifer in northwestern Germany, *Hydrogeology Journal*, *15*(2), 267-279.

Fetter, C. W. (2001), *Applied Hydrogeology*, Prentice Hall, N.J.

Frind, E. O. (1982), Simulation of long-term transient density-dependent transport in groundwater, *Advances in Water Resources*, *5*(2), 73-88.

Giambastiani, B. M. S., M. Antonellini, G. H. P. Oude Essink, and R. J. Stuurman (2007), Saltwater intrusion in the unconfined coastal aquifer of Ravenna (Italy): A numerical model, *Journal of Hydrology*, *340*(1-2), 91-104.

Goswami, R. R., and T. P. Clement (2007), Laboratory-scale investigation of saltwater intrusion dynamics, *Water Resources Research, 43*(4), doi: 10.1029/2006WR005151.

Goswami, R. R., B. Ambale, and T. P. Clement (2009), Estimating errors in concentration measurements obtained from image analysis, *Vadose Zone Journal*, *8*(1), 108-118.

Goswami, R. R., T. P. Clement, and J. H. Hayworth (2012), Comparison of Numerical Techniques Used for Simulating Variable-Density Flow and Transport Experiments, *Journal of Hydrologic Engineering*, *17*(2), 272-282.

Green, T. R., M. Taniguchi, H. Kooi, J. J. Gurdak, D. M. Allen, K. M. Hiscock, H. Treidel, and A. Aureli (2011), Beneath the surface of global change: Impacts of climate change on groundwater, *Journal of Hydrology*, *405*(3-4), 532-560.

Guo, W., and C. D. Langevin (2002), *User's Guide to SEWAT: A Computer Program for Simulation of Three-Dimensional Variable-Density Ground-Water Flow*, United States Geological Survey.

Henry, H. R. (1964), Effects of dispersion on salt encroachment in coastal aquifers, *U.S. Geological Survey Water-Supply Paper Rep. 1613-C*, C71-C84. pp.

Huyakorn, P. S., P. F. Andersen, J. W. Mercer, and H. O. White, Jr. (1987), Saltwater intrusion in aquifers: Development and testing of a three-dimensional finite element model, *Water Resour. Res.*, *23*(2), 293-312.

Illangasekare, T., et al. (2006), Impacts of the 2004 tsunami on groundwater resources in Sri Lanka, *Water Resour. Res.*, *42*(5), W05201.

IPCC (2007), Climate change 2007: Impacts, adaptation and vulnerability, *Contribution of Working Group II to the Fourth Assessment Report of the Intergovernmental Panel on Climate Change*, edited by M. L. Parry, O. F. Canziani, J. P. Palutikof, P. J. van der Linden and C. E. Hanson, Cambridge University Press Cambridge.

Johannes, R. E. (1980), The ecological significance of the submarine discharge of groundwater, *Marine Ecology Progress Series 3*, 365–-373.

Kanel, S. R., R. R. Goswami, T. P. Clement, M. O. Barnett, and D. Zhao (2008), Two dimensional transport characteristics of surface stabilized zero-valent iron nanoparticles in porous media, *Environ Sci Technol*, *42*(3), 896-900.

Karasaki, K., K. Ito, and K. Maekawa (2006), Simulation of salt water intruison, paper presented at TOUGH Symposium, Lawrence Berkeley National Laboratory, Berkely, California.

Kohout, F. A. (1960), Cyclic Flow of Salt Water in the Biscayne Aquifer of Southeastern Florida, *J. Geophys. Res.*, *65*(7), 2133-2141.

Kuan, W. K., G. Jin, P. Xin, C. Robinson, B. Gibbes, and L. Li (2012), Tidal influence on seawater intrusion in unconfined coastal aquifers, *Water Resour. Res.*, *48*(2), W02502.

Kundzewicz, Z. W., and P. Dölle (2009), Will groundwater ease freshwater stress under climate change?, *Hydrological Sciences Journal*, *54*(4), 665-675.

Lacombe, P. J., and G. B. Carleton (1992), Saltwater intrusion into fresh ground-water supplies, southern Cape May County, New Jersey, 1890-1991.

Langevin C, Shoemaker WB, and G. W (2003), Modflow-2000, The USGS Geological Survey modular ground-water model – documentation of the Seawat-2000 version with the variable density flow process (VDF) and the integrated MT3DMS transport process (IMT)*Rep.*, US Geological Survey.

Leatherman, S. P. (1984), Coastal geomorphic response to sea level rise : Galveston Bay, Texas, in Barth M.C., Titus J.G. (eds) Greenhouse effect and sea level rise : a challenge for this generation.*Rep.*, 151-178 pp, Reinhold, New York.

Lee, C. H., and R. T. S. Cheng (1974), On seawater encroachment in coastal aquifers, *Water Resources Research*, *10*, 1039-1043.

Li, H., and J. J. Jiao (2003a), Influence of the tide on the mean watertable in an unconfined, anisotropic, inhomogeneous coastal aquifer, *Advances in Water Resources*, *26*(1), 9-16.

Li, H., and J. J. Jiao (2003b), Tide-induced seawater-groundwater circulation in a multi-layered coastal leaky aquifer system, *Journal of Hydrology*, *274*(1-4), 211-224.

Li, H., M. C. Boufadel, and J. W. Weaver (2008), Tide-induced seawater-groundwater circulation in shallow beach aquifers, *Journal of Hydrology*, *352*(1-2), 211-224.

Li, L., D. A. Barry, F. Stagnitti, and J. Y. Parlange (1999), Submarine groundwater discharge and associated chemical input to a coastal sea, *Water Resour. Res.*, *35*(11), 3253-3259.

Loáiciga, H. A., T. J. Pingel, and E. S. Garcia (2011), Sea Water Intrusion by Sea-Level Rise: Scenarios for the 21st Century, *Ground Water*, no-no.

Mantoglou, A. (2003), Pumping management of coastal aquifers using analytical models of saltwater intrusion, *Water Resources Research*, *39*(12), 1335.

Masterson, J. P., and S. P. Garabedian (2007), Effects of Sea-Level Rise on Ground Water Flow in a Coastal Aquifer System, *Ground Water*, *45*(2), 209-217.

McCarthy, J. J. (2009), Reflections On: Our Planet and Its Life, Origins, and Futures, *Science, 326*(5960), 1646, doi: 10.1126/science.1184937.

Meisler, H., Leahy PP and Knobel LL. (1985), The effect of eustatic sea-level changes on saltwaterfreshwater relations in the northern Atlantic Coastal Plain: U.S. Geological Survey Water-Supply Paper 2255, 28 p.*Rep.*

Melloul, A., and M. Collin (2006), Hydrogeological changes in coastal aquifers due to sea level rise, *Ocean & Coastal Management*, *49*(5-6), 281-297.

Michael, H. A., A. E. Mulligan, and C. F. Harvey (2005), Seasonal oscillations in water exchange between aquifers and the coastal ocean, *Nature*, *436*(7054), 1145-1148.

Moore, W. S. (1996), Large groundwater inputs to coastal waters revealed by 226Ra enrichments, *Nature*, *380*(6575), 612-614.

Moore, W. S., and T. M. Church (1996), Submarine Groundwater Discharge, reply to Younger., *Nature*, *382*, 122.

Navoy, A. S. (1991), Aquifer-estuary interaction and vulnerability of groundwater supplies to sea level rise-driven saltwater intrusion, Pennsylvania State University, USA.

Oostrom, M., J. S. Hayworth, J. H. Dane, and O. Güen (1992), Behavior of dense aqueous phase leachate plumes in homogeneous porous media, *Water Resour. Res.*, *28*(8), 2123-2134.

Oude Essink, G. H. P. (2001), Salt Water Intrusion in a Three-dimensional Groundwater System in The Netherlands: A Numerical Study, *Transport in Porous Media*, *43*(1), 137-158.

Oude Essink, G. H. P., E. S. van Baaren, and P. G. B. de Louw (2010), Effects of climate change on coastal groundwater systems: A modeling study in the Netherlands, *Water Resour. Res.*, *46*, W00F04.

Pinder, G. F., and H. H. Cooper, Jr. (1970), A Numerical Technique for Calculating the Transient Position of the Saltwater Front, *Water Resour. Res.*, *6*(3), 875-882.

Ranjan, P., S. Kazama, and M. Sawamoto (2006), Effects of climate change on coastal fresh groundwater resources, *Global Environmental Change*, *16*(4), 388-399.

Robinson, C., L. Li, and H. Prommer (2007), Tide-induced recirculation across the aquifer-ocean interface, *Water Resour. Res.*, *43*(7), W07428.

Rozell, D. J., and T.-F. Wong (2010), Effects of climate change on groundwater resources at Shelter Island, New York State, USA, *Hydrogeology Journal*, *18*, 1657-1665.

Schincariol, R. A., and F. W. Schwartz (1990), An experimental investigation of variable density flow and mixing in homogeneous and heterogeneous media, *Water Resour. Res.*, *26*(10), 2317-2329.

Segol, G. (1994), *Classic Groundwater Simulations Proving and Improving Numerical Models*, Old Tappan, N. J.

Segol, G., G. F. Pinder, and W. G. Gray (1975), A Galerkin-finite element technique for calculating the transient position of the saltwater front, *Water Resour. Res.*, *11*(2), 343-347.

Simmons, G. M. (1992), Importance of submarine groundwater discharge (Sgwd) and seawater cycling to material flux across sediment water interfaces in marine environments., *Marine Ecology Progress Series 84*, 173-184.

Simpson, M. J., and T. P. Clement (2003), Theoretical analysis of the worthiness of Henry and Elder problems as benchmarks of density-dependent groundwater flow models, *Advances in Water Resources*, *26*(1), 17-31.

Simpson, M. J., and T. P. Clement (2004), Improving the worthiness of the Henry problem as a benchmark for density-dependent groundwater flow models, *Water Resour. Res.*, *40*(1), W01504.

Simpson, M. J., T. P. Clement, and T. A. Gallop (2003), Laboratory and Numerical Investigation of Flow and Transport Near a Seepage-Face Boundary, *Ground Water*, *41*(5), 690-700.

Smith, A. J. (2004), Mixed convection and density-dependent seawater circulation in coastal aquifers, *Water Resour. Res.*, *40*(8), W08309.

Strack, O. D. L. (1976), A single-potential solution for regional interface problems in coastal aquifers, *Water Resources Research*, *12*(6), 1165-1174.

Sun, Y., and T. P. Clement (1999), A Decomposition Method for Solving Coupled Multi-Species Reactive Transport Problems, *Transport in Porous Media*, *37*, 327-346.

USGS (2000), Ground-Water Resources for the Future - Atlantic Coastal Zone*Rep.*

Vermeer, M., and S. Rahmstorf (2009), Global sea level linked to global temperature, *Proc. Natl. Acad. Sci., 106*(51), 21527-21532, doi: 10.1073/pnas.0907765106

Volker, R. E., Q. Zhang, and D. A. Lockington (2002), Numerical modelling of contaminant transport in coastal aquifers, *Mathematics and Computers in Simulation*, *59*(1??), 35-44.

Voss, C. I., and W. R. Souza (1987), Variable density flow and solute transport simulation of regional aquifers containing a narrow freshwater-saltwater transition zone, *Water Resour. Res.*, *23*(10), 1851-1866.

Voss, C. I., and A. M. Provost (2002), A model for saturated-unsaturated, variable-density ground-water flow with solute or energy transport*Rep.*, U.S. Geol. Surv., Reston, Va.

Watson, T. A., A. D. Werner, and C. T. Simmons (2010), Transience of seawater intrusion in response to sea level rise, *Water Resour. Res.*, *46*(12), W12533.

Webb, M. D., and K. W. F. Howard (2010), Modeling the Transient Response of Saline Intrusion to Rising Sea-Levels, *Ground Water*.

Werner, A. D., and C. T. Simmons (2009), Impact of Sea-Level Rise on Sea Water Intrusion in Coastal Aquifers, *Ground Water, 47*(2), 197-204, doi: 10.1111/j.1745-6584.2008.00535.x.

Werner, A. D., J. D. Ward, L. K. Morgan, C. T. Simmons, N. I. Robinson, and M. D. Teubner (2011), Vulnerability Indicators of Sea Water Intrusion, *Ground Water*, no-no.

Westbrook, S. J., J. L. Rayner, G. B. Davis, T. P. Clement, P. L. Bjerg, and S. J. Fisher (2005), Interaction between shallow groundwater, saline surface water and contaminant discharge at a seasonally and tidally forced estuarine boundary, *Journal of Hydrology*, *302*, 255-269.

White, I., and T. Falkland (2009), Management of freshwater lenses on small Pacific islands, *Hydrogeology Journal*, *18*(1), 227-246.

WWD (1998), Groundwater: the Invisible Resource.

Yu, W., C. Voss, H. Michael, K. M. Ahmed, L. Feinson, M. R. Khan, and A. Tuinhof (2010), Implications of climate change for fresh groundwater resources in coastal aquifers in Bangladesh*Rep.*, The world bank
US Geological Survey.

Zhang, Q., R. E. Volker, and D. A. Lockington (2002), Experimental investigation of contaminant transport in coastal groundwater, *Advances in Environmental Research*, *6*(3), 229-237.